The Potential of Energetic Condensation Techniques for SRF Applications

—

The First Extensive SRF Performance Study on Nb/Cu by ECR Deposition

DISSERTATION
zur Erlangung des Grades eines Doktors
der Naturwissenschaften (Dr. rer. nat.)

vorgelegt von
Dipl.-Phys. Sarah Katharina Aull

eingereicht bei der Naturwissenschaftlich-Technischen Fakultät
der Universität Siegen
Siegen 2023

Angefertigt am Europäischen Kernforschungszentrum CERN, Schweiz

Erster Gutachter:	Univ.-Prof. Dr. Jens Knobloch (Univerisität Siegen)
Zweiter Gutachter:	Univ.-Prof. Dr. Florian Hug (JGU Mainz)
Tag der mündlichen Prüfung:	31. März 2023

Abstract

Particle accelerators operating in continuous wave (cw) mode or at high duty cycles usually use superconducting radio-frequency (SRF) cavities for particle acceleration due to the lower power consumption compared to normal conducting accelerating structures.

The niobium thin film technology, where a copper structure is coated with a some μm thick niobium film, offers numerous advantages over structures made from niobium sheet in terms of thermal and mechanical stability, raw material costs, and complexity of cryomodules. However, the strong increase of surface resistance with RF magnetic field, the so-called Q-slope, currently limits the application of niobium thin films to low accelerating gradients. The established DC magnetron sputtering technology is now challenged by energetic condensation techniques which promise to improve the microstructure of a coating and subsequently improve the RF performance. Electron cyclotron resonance (ECR) deposition is the most advanced representative of the class of energetic condensation techniques.

This thesis presents the first SRF results of an ECR niobium-on-copper coating at operation-typical frequencies. The film was studied using the Quadrupole Resonator (QPR) which is the ideal tool for comprehensive investigations of the superconducting surface resistance at different temperatures, RF fields, at cavity typical frequencies and with different ambient conditions. For the latter, the QPR has been extended with a solenoid for controlling the ambient magnetic field. SEM, EBSD, FIB and EDS analyses provided further insight regarding the film microstructure and enabled linking the film properties to the RF performance. The coating exhibits bulk-like material properties and a strongly mitigated Q-slope confirming the potential of the ECR technique in particular and of energetic condensation techniques in general. The surface resistance increase with field is however still stronger than in bulk niobium of comparable material quality. The results suggest that the grain boundaries, their density and degree of oxidation, as well as the heat transfer through the niobium-copper interface are the key aspects for the RF performance rather than the mean free path alone. Furthermore, the roles of ambient magnetic field and cooling conditions were extensively studied: It was found that despite the bulk-like properties and just like previous Nb/Cu coatings, also the studied ECR coating exhibits very low surface resistance sensitivity to ambient magnetic field. In contrast, the cooling dynamics have been identified as impacting the surface resistance severely. Finally, a discussion of the trapped flux sensitivity comes to the conclusion that the low sensitivity in Nb/Cu is not only due to a beneficial combination of short mean free path and low frequency, but is dominated by stronger pinning compared to bulk Nb.

Looking beyond niobium, this thesis additionally presents secondary electron yield (SEY) data of various SRF material candidates. The SEY is the key material parameter for determining the multipacting risk. Although multipacting is not a limitation in elliptical cavities anymore, it is certainly still a limitation in non-elliptical cavities, including the Quadrupole Resonator. The results suggest that Niobium compounds are not critical. MgB_2 however holds a strong risk of electron activity due to the formation of MgO when exposed to air.

Zusammenfassung

Teilchenbeschleuniger für Dauerstrichbetrieb oder hohen Tastgrad nutzen häufig supraleitende Hohlraumresonatoren zur Teilchenbeschleunigung, da ihr Stromverbrauch im Vergleich zu normalleitenden Beschleunigunsstrukturen geringer ist.

Die Niobfilmtechnologie bietet gegenüber Niobblech viele Vorteile hinsichtlich thermischer und mechanischer Stabilität, Kosten für Rohmaterial und der Komplexität eines Kryomoduls. Dennoch begrenzt die Zunahme des Oberflächenwiderstand mit der Feldstärke der Hochfrequenz, die Anwendbarkeit von dünnen Niobfilmen auf kleine Beschleunigungsgradienten. Die etablierte Technik des Gleichstrom-Magnetronsputterns (DCMS) wird nun von energetischen Abscheidungsverfahren herausgefordert, die eine verbesserte Mikrostruktur der Beschichtung und daraus resultierendes verbessertes Hochfrequenzverhalten versprechen. Elektronen-Zyklotronresonanz (ECR) Beschichtung ist eine Vertreterin der Klasse der energetischen Abscheidungsverfahren und ist zur Zeit am weitesten entwickelt.

Diese Dissertation präsentiert die ersten Hochfrequenzergebnisse einer ECR-Niobbeschichtung. Der Film wurde mit dem Quadrupol Resonator (QPR) charakterisiert, der das ideale Instrument für umfassende Studien des Oberflächenwiderstands bei unterschiedlichen Temperaturen, Hochfrequenzfeldern, kavitätentypischen Frequenzen und mit verschiedenen äußeren Bedingungen ist. Für letztere wurde der QPR um einen Solenoiden erweitert um äußere statische Magnetfelder zu erzeugen und ihren Einfluss auf den Oberflächenwiderstand zu untersuchen. Rasterelektronenmikroskopie (SEM), Elektronenrückstreubeugung (EBSD), Ionenfeinstrahlmikroskopie (FIB) und Energiedispersive Röntgenspektroskopie (EDS) ermöglichten zusätzliche Einblicke in die Filmmikrostruktur und erlauben die Filmeigenschaften mit dem Hochfrequenzverhalten zu verbinden. Die Beschichtung zeigte Eigenschaften vergleichbar mit massivem Niob und einen stark abgeschwächten Oberflächenwiderstandsanstieg. Dies bestätigt das Potential des ECR Verfahrens im Speziellen aber auch das Potential der energetischen Beschichtungsverfahren im Allgemeinen. Der Oberflächenwiderstandsanstieg ist allerdings immer noch stärker als bei gleichwertigem Niobblech. Die Ergebnisse legen nahe, dass sowohl Korngrenzen, deren Kompaktheit und Oxidationszustand, als auch der Wärmeübertrag durch die Niob-Kupfer-Grenzfläche die Hauptrollen für das Hochfrequenzverhalten spielen. Darüber hinaus wurde die Unempfindlichkeit gegenüber externen Magnetfelder bewahrt aber eine starke Abhängigkeit des Oberflächenwiderstands gegenüber der Abkühlbedingungen festgestellt.

Auf der Suche nach neuen Materialen für supraleitende Kavitäten wurde die Sekundärelektronenausbeute (SEY) der vielversprechensten Kandidaten untersucht und das Risiko von Elektronenaktivität als wiederkehrende Feldlimitierung evaluiert. Die Messungen zeigen ähnliches Verhalten für Nb_3Sn, Nb(Ti)N und Niob; daher besteht kein zusätzliches Risiko eines elektronenverursachten Spannungseinbruchs. Bei MgB_2 besteht ein hohes Risiko Elektronenaktivität zu erzeuen, da es an Luft MgO bildet und MgO eine der höchsten SEY-Werte hat.

Acknowledgements

The completion of this thesis represents a significant personal milestone, and it would not have been possible without the support and guidance of many individuals.

I would like to express my sincere gratitude to my University supervisor, Prof. Jens Knobloch, for opening many doors within the SRF community, for always challenging the work in a constructive manner, and for supporting the completion of my thesis – especially this long after the research work was finished.

This work has been sponsored by the Wolfgang Gentner Programme of the German Federal Ministry of Education and Research (grant no. 13E18CHA). As such, I am thankful for the financial support during the three years as a doctoral student at CERN.

I am indebted to Tobias Junginger, who generously took charge of supervising me on a day-to-day basis. His expertise, training and support enabled me to drive my research project forward.

I owe gratitude to Anne-Marie Valente-Feliciano (Jefferson Lab) who provided the sample upon which this thesis is based, and with whom I engaged in many fruitful discussions. Thank you for being a stellar collaborator and role-model.

I would like to thank Reza Valizadeh (STFC), Ana Teresa Perez Fontenla (formerly CERN), Sam Posen (formerly Cornell), Xiaoxing Xi (Temple University), Marco Bonura (University of Geneva), Jérémie Teyssier (LTA Geneva) and Mounir Driss Mensi (formerly CERN) for supporting my research with additional samples and/or material analysis.

Thank you to the members of the technical teams supporting the SRF activities at CERN, in particularly Gaby Pechaud (clean room), Serge Forel (chemistry) and Sebastien Prunet (cryogenics) who always made an effort to accommodate my requests. Additionally, thank you to Torsten Köttig for his cryogenic expertise.

On a more personal note, I enjoyed working with Alick Macpherson, Nikolai Schwerg and Tobias Junginger. Lunch was never boring with these three.

Finally, I would like to close with a general thank you to friends, family and colleagues around the world who supported me in my academic, professional or personal development throughout my PhD endeavor.

Contents

1. Introduction

More and more superconducting radio-frequency (RF) cavities are being installed in particle accelerators around the world. This is due to the fact that the dissipated power in the cavity walls is 5 to 6 orders of magnitude lower than for normal conducting structures and that nowadays considerable high gradients can be achieved on an industrial production scale. Todays superconducting cavities are made from niobium which is the element with the highest transition temperature of 9.2 K. These cavities are cooled by liquid helium and operate at temperatures between 1.8 K and 2.1 K or at 4.5 K. It is clear that for operation at cryogenic temperatures, the required refrigeration power has to be taken into account when estimating cost efficiency. Still, superconducting cavities are often more cost effective than normal conducting structures, especially for operation in cw mode or at high duty cycles. However, cavities reaching field levels close to the theoretical limit are rare and cannot yet be produced on an industrial production scale. Improving existing preparation procedures and developing new ones focusses on obtaining reliably high accelerating gradients which requires understanding the underlying loss mechanisms at medium and high fields as well as understanding the physics of the various cavity treatments. Nevertheless, for (quasi-)cw machines low losses, i.e. high quality factors Q, are more important than high accelerating gradient as becomes clear when calculating the cryogenic consumption both in terms of static and dynamic losses.

The dissipated power into the helium has to be scaled with the carnot efficiency $\eta_{\text{carnot}}$and the technical efficiency of the cryogenic plant which is estimated with $\eta_{\text{tech}} = 20\,\%$ for 2 K operation and $\eta_{\text{tech}} = 30\,\%$ for 4.5 K operation [1]. The static losses per unit length p' are typically in the range of a few W/m. The length of the cold section(s) is given by the length of the cavity l_{cavity} and the number of cavities n_{cavity} which depends on the total RF voltage V_{RF} required and the accelerating gradient:

$$P_{\text{static}} = \frac{p' \cdot n_{\text{cavity}} \cdot l_{\text{cavity}}}{\eta_{\text{carnot}}\eta_{\text{tech}}}. \tag{1.1}$$

The dynamic losses scale with V_{RF}^2 and depend additionally on the surface resistance of the material R_{S} and on the geometry of the cavity cell. The cell geometry in turn has an influence on the R/Q which describes how efficiently a particle can be accelerated for a given stored energy, and on the geometry factor G which describes the magnetic fiel distribution in the cell volume and on the cell wall:

$$P_{\text{dynamic}} = \frac{n_{\text{cell}}\,(E_{\text{acc}} \cdot l_{\text{cell}})^2}{R/Q \cdot \eta_{\text{carnot}}\eta_{\text{tech}}} \frac{R_{\text{S}}}{G} \tag{1.2}$$

Figure 1.1a displays exemplarily the static, dynamic and total cryogenic losses as function of accelerating gradient for a fixed total voltage. With increasing accelerating gradient, the machine becomes shorter and the static losses decrease. In contrast, the dynamic losses increase linearly with accelerating gradient E_{acc} as the number of cells n_{cell} in Equation 1.2 decreases with $1/E_{\text{acc}}$ for a given total RF

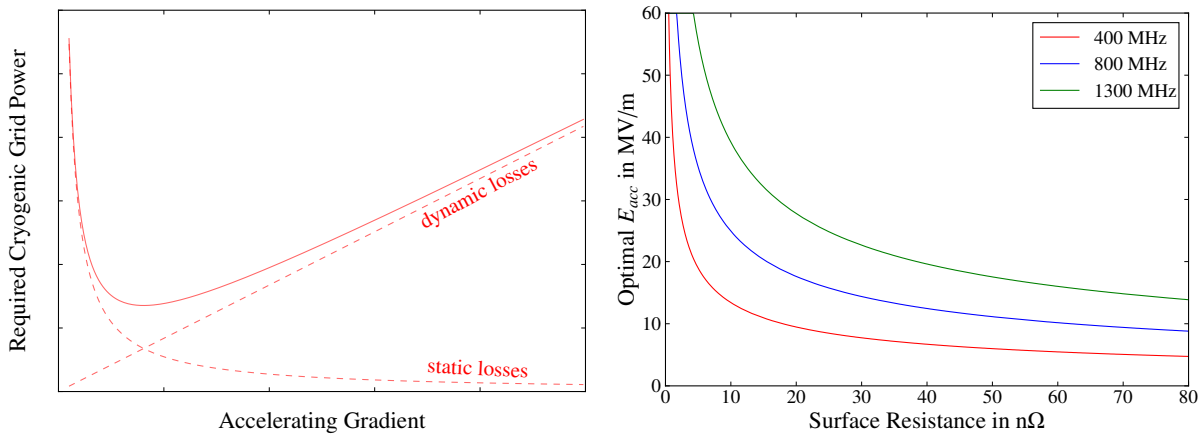

(a) (b)

Figure 1.1.: (a) Generic cryogenic losses as function of accelerating gradient and (b) the optimal gradient for minimal cryogenic losses as function of surface resistance.

voltage. Consequently, the total cryogenic consumption has an optimum accelerating gradient where the total cryogenic losses are minimal. This optimal accelerating gradient depends only on the surface resistance for a given RF frequency, the static losses per unit length and the number of cells per cavity. Exemplarily, the optimal gradient as function of surface resistance is calculated for single cell cavities at 400 MHz, 800 MHz and 1.3 GHz with static losses of 8 W/m which is the static heat load from the LEP machine and considered very conservative [2] and the resulting curves are displayed in Figure 1.1b.

Considering 10 nΩ as a realistic lower limit for any cavity geometry in high volume production, it can be concluded from Figure 1.1b that accelerating gradients up to 40 MV/m at 1.3 GHz and only 14 MV/m at 400 MHz or 25 MV/m at 800 MHz are optimal for cw machines. For lower static losses per unit length and multi-cell cavities, the optimal gradient is even lower. The need of higher gradients is limited to accelerators with strong restrictions on the length of the RF system and machines where installation cost are comparable to the life time operation cost, in particular linear accelerators.

Therefore a lot of effort is put into maximising Q at moderate accelerating gradients. Treatments that shorten the electron mean free path in sheet (*bulk*) niobium lower the contribution from thermally activated quasi-particles, i.e. the temperature dependent part of the surface resistance. This contribution can be derived from the Bardeen, Cooper, Schriefer (BCS) theory and is typically referred to as the BCS resistance. Moreover, dissolved gases, foreign materials and ambient magnetic fields might contribute to the residual resistance which is the dominant contribution for operating temperature between 1.8 K and 2 K. Alternatively, niobium-on-copper coatings can be tuned to minimise the BCS resistance and have been shown to achieve residual resistance values as low as for bulk niobium. These coatings have the advantage of very good thermal stability due to the copper substrate and are significantly less sensitive to ambient magnetic fields, but they suffer more severely from field dependent losses. The thermal stability in combination with the low BCS resistance (at low frequency) allow for operation at 4.5 K and make Nb films especially interesting for machines facing high heat loads from higher order modes and for accelerators of non-relativistic particles which typically favour low frequency. The later usually have non-elliptical geometries which might impede cooling and/or are often bulky objects.

CERN has a long history in the application of niobium coated copper cavities. With the upgrade of LEP, niobium coated cavities were installed and operated in a particle accelerator not only for the first time, but also as the largest SRF system ever built. Also for the LHC and the High Intensity and Energy upgrade of the ISOLDE accelerator for radioactive ions, HIE-Isolde, niobium coated cavities were chosen. Parallel to the design of the LHC, a vigorous R&D programme for niobium coatings on 1.5 GHz cavities was pursued resulting in excellent low field behaviour outperforming bulk Nb at that time. The program was discontinued early in the new millennium though. The niobium coating activities were re-launched for the HIE-Isolde project and the R&D re-started focussing on new coating technologies for elliptical cavities. Due to the strong decline of the quality factor with RF field, the application of Nb coated cavities is still limited to accelerating gradient below 10 MV/m.

The quest for accelerating gradients and quality factors beyond the theoretical limits steers R&D activities also into the direction of materials beyond bulk niobium. On the one hand, this lead to a revival of the niobium coating efforts and on the other hand it pushed exploring alternative superconductors such as Nb_3Sn, NbTiN and MgB_2.

The Quadrupole Resonator is an ideal tool for studying the SRF surface resistance. It is a sample test cavity that allows the RF characterization of superconducting samples as function of temperature, RF field and for three typical cavity frequencies. CERNs Quadrupole Resonator operates at 400 MHz, 800 MHz and 1200 MHz. Due to a recent upgrade also trapped flux studies are possible. Moreover, the calorimetric measurement principle assures high resolution measurements. Therefore, the Quadrupole Resonator allows the investigation of loss mechanisms usually attributed to the residual resistance. In addition to the wide parameter range of the Quadrupole Resonator measurements, the fact that the samples are flat and compared to cavity surfaces small makes the Quadrupole Resonator also an ideal set-up for studying new coating techniques and alternative materials before it is possible to coat an entire cavity surface with all geometry related issues.

1.1. Outline of this Thesis

The objective of this thesis is to discuss the potential of the niobium film technology and other materials beyond bulk niobium. Chapter 2 starts with introducing the reader to the current limitations of state of the art bulk niobium technology. In the following, the potential advantages and current limitations of the niobium film technology and alternative materials are presented. In the context of coatings, the most important deposition techniques for SRF applications are summarised. Chapter 3 gives an overview over the main limitations of SRF materials: the minimal heat load given by the surface resistance, the maximum accelerating gradient given by the maximum magnetic surface field up to which superconductivity can persist and the secondary electron yield which might cause electron avalanches and limit the operation of an SRF cavity to very low fields. The Quadrupole Resonator as the main measurement tool is introduced in Chapter 4. The design and measurement principle are described along with the hardware upgrades done within this work. Moreover, a simulation of thermal effects is discussed and the preparation of the samples is outlined. The results presented in Chapter 5 and Chapter 6. Chapter 5 is dedicated to the different SRF performance of a niobium coating compared to bulk niobium. After discussing similarities and differences of the two samples in terms of material parameters and low field

RF behaviour, the effect of medium RF fields, the influence of the cooling conditions and the effect of ambient magnetic fields are discussed giving insight regarding the loss mechanisms in niobium coatings. Chapter 6 presents secondary electron yield data of the most interesting alternative materials for SRF application. This thesis closes with summarizing the findings and drawing general conclusions in Chapter 7 and gives an outlook to future investigations in Chapter 8.

2. Overcoming the Limits of the Bulk Niobium Technology

Ultimate performance for bulk niobium can be understood as maximum quality factor (Q) at maximum accelerating gradients (E_{acc}). SRF cavities with high Q performance are crucial for cw and high duty cycle applications such as (circular) particle colliders for high energy physics, light sources or accelerator driven systems and spallations sources. Several accelerator projects with one of these perspectives are under design or construction with their cryogenic load being the cost driver. For low duty cycle applications, the installation costs, i.e. the footprint of the machine, dominate costs. Hence, for low duty cycle machines the focus is on high accelerating gradient E_{acc}.

As it is difficult to achieve both high Q and high gradient at the same time, current research activities focus either on maximum Q at medium accelerating fields or maximum E_{acc} with moderate Q depending on the accelerator project under consideration. In the medium-term, bulk niobium performance is expected to reach the fundamental limitations given by the material so that the development of alternative materials which have the potential to outperform niobium will be necessary in the long term.

This chapter gives the reader an overview over the limits of the well established bulk niobium technology with regards to quality factor and accelerating gradients, followed by a presentation of the alternative material options that are currently under investigation. With a focus on Nb/Cu coatings, a brief introduction to film growth is given and the coating techniques which are pursuit for Nb coatings are presented including their status of development.

2.1. Limits of Bulk Niobium Technology

To date, most accelerators using superconducting cavities rely on bulk niobium technology. Niobium has been the material of choice due to its comparatively high critical temperature of 9.2 K and its good mechanical properties. In terms of accelerating fields, the cavity performance is limited by the magnetic field above which the material becomes normal conducting. This intrinsic property of the superconductor represents the ultimate limit for magnetic surface fields B_{peak} inside the cavity. In terms of power dissipated in the cavity walls, i.e. cryogenic losses, the surface resistance defines the ultimate limitation. Here, the critical temperature, the operational temperature and the purity of the material are the dominant contributors.

2.1.1. Reaching Maximum Accelerating Gradients

The achievable accelerating gradients increased with the development of surface preparation procedures and, as shown in Figure 2.1, by optimizing the cavity geometry. As the surface magnetic field in the

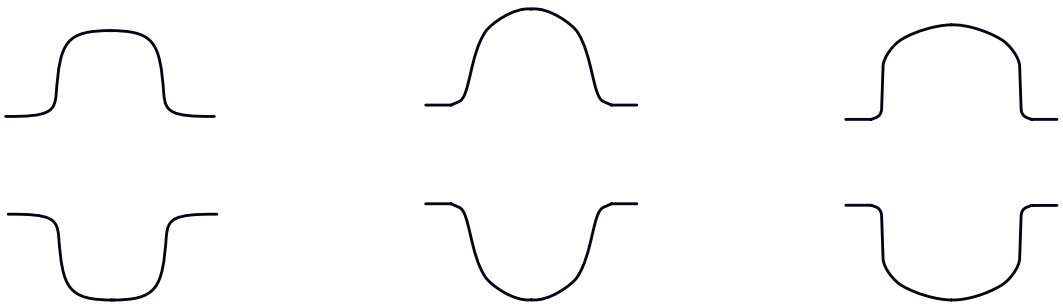

Figure 2.1.: Evolution of cavity geometries: (a) 1st generation with multipacting as main limitation, (b) TESLA avoiding multipacting and (c) the low loss/re-entrant shape reducing the peak magnetic field for a given accelerating gradient.

cavity is the fundamental limitation, the cavity geometry can be optimized by minimizing the ratio of $B_{\text{peak}}/E_{\text{acc}}$ in order to reach highest accelerating gradients.

Figure 2.2 shows the evolution of accelerating gradients with time. The first generation of cavities (see Figure 2.1a) was limited by multipacting. The almost parallel walls of the cell favoured the resonant effect of local electron avalanches. These electrons absorb the RF power and lead to local heating and eventually thermal breakdown of the cavity. Spherical/elliptical shapes, for example the TESLA shape (Figure 2.1b), suppressed hard low field multipacting barriers, so that todays performance limit is field emission or quench due to defects. With improvements of the surface preparation, clean handling and avoiding or repairing features, the gradient has been pushed higher in recent years. As all preparation steps become more challenging for mutli-cell cavities, their evolution of E_{acc} lags behind the single cell results.

The most recent milestone (for single-cell cavities) was achieved by the development of the *low loss* and the *re-entrant* cavity shapes as sketched in Figure 2.1c. Both shapes reduce the ratio $B_{\text{peak}}/E_{\text{acc}}$ so that the magnetic surface field for a given accelerating field is lower than for the standard TESLA design. Depending on the design improvement is of the order of 9 % to 15 % for the fields ratio, but comes with 15 % to 21 % higher $E_{\text{peak}}/E_{\text{acc}}$ [3]. The higher $E_{\text{peak}}/E_{\text{acc}}$ ratio leads to an increased risk of field emission with respect to the TESLA shape, and so requires even better cleaning and handling.

To date, a re-entrant shaped single-cell cavity holds the world record for accelerating gradient of 59 MV/m corresponding to a surface magnetic (peak) field of 206 mT [4]. Several TESLA cavities have reached this range of surface magnetic fields (with lower E_{acc}), but all of these cavities where single cells, and the low loss cavity underwent several iterations of surface preparation until the maximum field was reached. The production of a 3 and a 9-cell re-entrant cavity was attempted by CORNELL but neither of the cavities exceeded standard TESLA performance [5, 6].

The preparation of SRF cavities with maximum gradients on a mass-production scale is however still challenging. For the installation of very high gradient cavities, the processes need to be optimized and industrialized so that the required performance can be reliably reached with a reasonable number of preparation steps. Avoiding (and curing) features that could serve as field emission sites or quench locations is a major challenge.

For bare cavity validation Figure 2.3 shows a typical production flow of a bulk niobium cavity: After

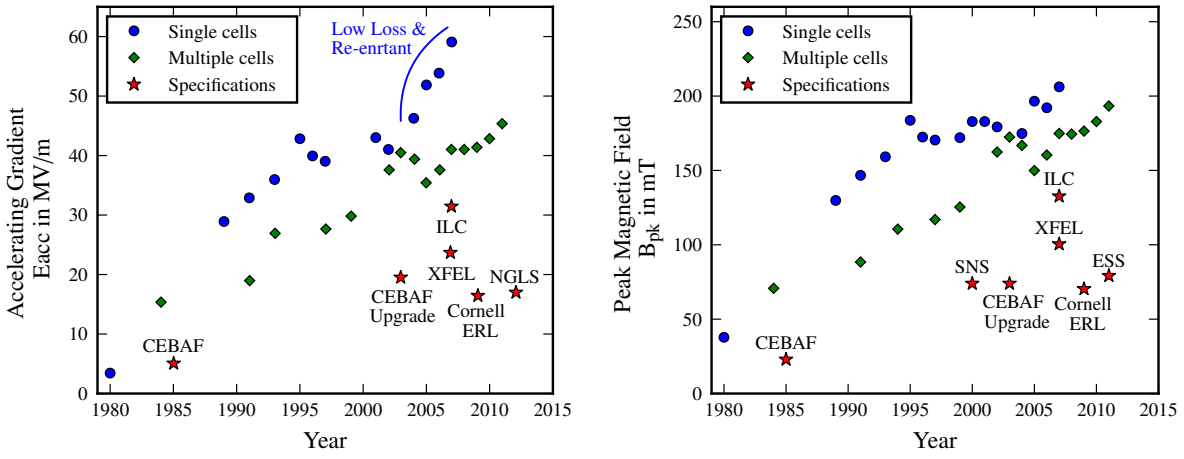

(a) (b)

Figure 2.2.: Evolution of the (a) accelerating gradients and (b) surface magnetic fields for single cell and multi-cell cavities. Reproduced from Reference [7].

fabrication of the half-cells, a bulk chemical treatment is done to remove a damage layer from production of about 150 µm, before half-cells are electron beam welded (EBW), and then undergo an additional light chemical treatment (including a ultrasonic bath) to remove contaminants from the EBW. Alternatively, the half-cells are welded first and the bulk chemical treatment is done on the full cavity. This depends on the chemical treatment facilities and the size and complexity of the cavity. Depending on the application the cavity is afterwards baked at high temperature (typically at 800 °C) to purify and recrystallise the material, followed by a light chemical treatment to remove contaminants. Finally the cavity is rinsed with ultra-pure water at high (typically 100 bar) pressure to remove dust particles from the surface. The high pressure rinsing (HPR) is often followed by an in-situ bake at low temperature (120 °C) in order to tune the mean free path in the surface layer and/or facilitate drying.

After assembly in a ISO 4 to ISO 5 clean room, the cavity can finally be installed in the cryostat, cooled down and tested. If specifications are not reached, the cavity is typically retreated, which usually means an additional HPR in case of field emission or heat and/or chemical treatment if the cavity prematurely quenched or the quality factor is strongly degraded.

As for chemical treatments of the RF surface buffered chemical polishing (BCP) and electro-polishing (EP) are the standard processes. EP is known to produce a smoother surface than BCP, but the result depends strongly on the initial state of the surface [8]. In order to create a smooth cavity surface, repair defects and/or remove field emitters cavities can be prepared with centrifugal barrel polishing (CBP) [9]. For CBP the cavity is partially filled with liquid loaded with abrasive media of different material, size and shape [10], and then rotated. This mechanical polishing results in a mirror-like finish surface with a roughness one order of magnitude better than optimum EP [11], but the process holds the risk of embedding media into the surface as well as loading the material with hydrogen. As the crystal lattice at the surface is damaged during tumbling, a light EP of about 20 µm to 30 µm has to be done and a heat treatment might also be necessary. CBP can also be applied instead of the initial bulk chemical treatment done to remove the damaged surface layer from the production of the sheet and forming the (half-) cells.

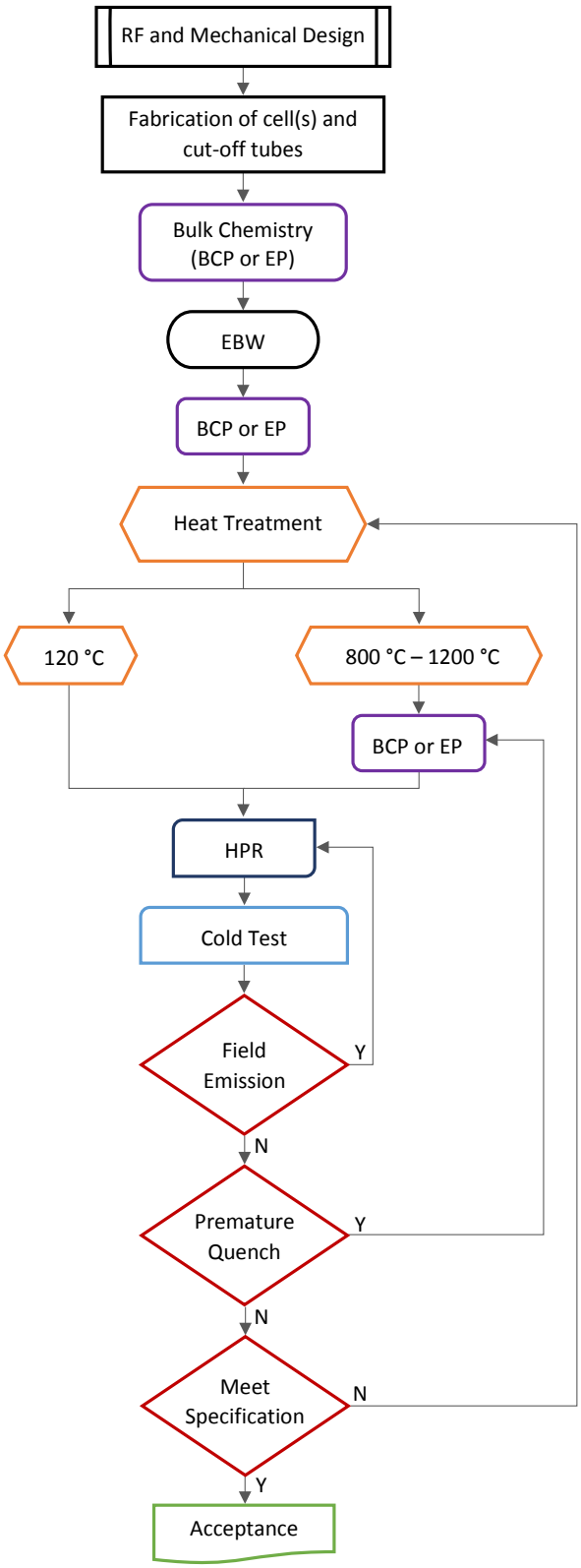

Figure 2.3.: Typical production flow chart of a bulk niobium cavity.

Effort is being invested in chemistry-free CBP in order to avoid chemical treatments completely [12]. As EP and BCP are both using hydrofluoric acid (HF), they require special facilities for handling and disposal in addition to specific training and safety regulations. Eliminating HF from the cavity preparation process would therefore have strong benefits for safety and cost.

Independent of the specific surface preparation procedures, the cryostating of cavities and their installation in an accelerator requires that the resulting spread in cavity performance be small, and achievable within a reasonable number of processing and reprocessing steps. In order to achieve this, the target accelerating gradients for the current accelerator projects are typically set at maximum half of the theoretical possible, often in the range of 20 MV/m (at 1.3 GHz; 31.5 MV/m for ILC).

2.1.2. Reaching Highest Quality Factors

The quality factor Q of a cavity is given by its geometry represented by the geometry factor G and the surface resistance R_S,

$$Q = \frac{G}{R_S}, \tag{2.1}$$

and can be maximised by optimising the cavity geometry for a given R_S. For elliptical cavities, the geometry factor typically varies between 270 Ω (TESLA [6]) and 295 Ω (1.5 GHz Nb/Cu programme at CERN [13]).

As will be subject to Section 3, the surface resistance consists of two contributions: the BCS resistance and the residual resistance which both depend on the RF field strength. The BCS resistance for bulk niobium at typical cavity frequencies (400 MHz to 1.3 GHz) ranges from 60 nΩ to 1 μΩ at 4.5 K and between 0.2 nΩ and 6 nΩ at 1.8 K. The residual resistance is usually comparable or higher than the BCS resistance at low temperature, so that minimising both contributions is desirable for 2 K operation.

For a given operating temperature (and material), the BCS resistance can only be changed by acting on the electron mean free path. Over the years many recipes have been developed to improve the quality factor for a certain accelerating gradient range: The *mild baking*, typically at 120 °C for 48 h, promotes oxygen diffusion towards the surface which transforms the niobium oxide states of the surface layer [14] and suppresses the formation of nano-hydrides [15]. This heat treatment shortens the mean free path and therefore reduces the BCS contribution [14]. However, it comes with an increase in residual resistance and tends to only be beneficial for sufficiently high frequencies unless it is applied to cure the so-called *high field Q-drop*, a strong degradation of Q above 100 mT peak magnetic field.

Heat treatments at higher temperatures (between 600 °C and 1400 °C) dissolve gases from the bulk, reduce the number of dislocations and recrystallise the material, which leads to an increase of mean free path in the bulk. The high temperature bakings strongly pollute the top surface layer which makes it necessary to remove several microns after baking.

The most recent discovery is the so called anti-Q-slope, i.e. an increase of Q with accelerating field [16]. This *nitrogen doping* is achieved by diffusing nitrogen into the crystal lattice and followed by a light electro-polishing to remove all weak or non superconducting niobium nitrides. The remaining surface is characterised by interstitial nitrogen in the double-digit ppm range [17]. The mechanism behind the decreased surface resistance for nitrogen doped cavities, along with the significantly reduced

quench field is yet not well understood. Suppressing the formation of nanohydrides was recently found not to be an accurate explanation of the phenomenon [18].

The residual resistance accounts for all additional surface resistance contributions due to external sources which might be reduced independently of the material parameters. One of the major contributors is trapped magnetic flux which will be discussed in detail in Section 3.2.2. Recent studies have shown that the amount of trapped field depends on the cavity material and treatment [19] and on the cooling dynamics [19, 20, 21, 22]. The latter acts in two different ways: Depending on the cooling speed and the temperature gradient across the cavities at the moment of the superconducting transition the ambient field can be more or less efficiently expelled [21]. Additionally, a temperature gradient across the cavity can induce a thermo-electric current that may create an additional magnetic field which can in turn be trapped [23]. For this to happen, there needs to be a closed loop over the cavity, that is closed through the support structure or the helium tank.

Without the closed loop a voltage drop will be thermally induced but no current can flow. Although a thermo-current can exist in a single material, bi-metal contacts might emphasise this effect if the difference in Seebeck coefficients of the two materials is significant, i.e. the induced voltage per kelvin, is big enough. This is of particular importance when considering the cavity-helium tank system [24].

Finally, the surface roughness is known to have an influence on the residual resistance [25] and the formation of oxides and hydrides need to be considered.

2.1.3. Optimising Cavity Production

Availability of High Purity Niobium

Large scale accelerator projects increase the demand for high purity niobium and require manufacturing processes that are fast, reliable and cost effective. The U.S. Geological Society, *USGS*, reports the world production of niobium ore from mining of roughly 50 000 t in the last years [26].

Almost 90 % of the world production is used for ferro-niobium in steel. Of the remaining 10 %, about a quarter is used for the production of niobium alloys, which are highly important for superconducting magnets, and 1 % for high purity Nb [27]. Overall, annual niobium material in the order of 500 t is available for SRF applications.

The huge bulk niobium projects, such as ILC with 16 000 9-cell TESLA cavities, X-FEL with about 800 9-cell TESLA cavities, in addition to other accelerators like the Cornell ERL with 400 7-cell 1.3 GHz cavities, the European Spallation Source, *ESS*, with 36 6-cell and 84 5-cell cavities both operating at 704 MHz (plus 28 spoke cavities) and the New Light Source, *NLS*, 144 9-cell TESLA cavities will already constitute several years worth of high grade niobium annual world production. The availability of high purity niobium for yet another superconducting large scale machine might therefore be questionable or may lead to a strong increase in cost. Hence, the use of thin film technology offers big potential for keeping material costs at a reasonable level.

Manufacturing Processes

In addition to the optimisation of the cavity design and surface preparation, optimisation of the manufacturing process additionally provides the opportunity to lower production costs and produce cavities

more accurately and more reliably.

The standard technique to form SRF cavities is deep drawing where spring back the metal sheet is drawn into a forming die; the cavity parts are then joined by electron beam welding (EBW). Elliptical cavities are also fabricated by spinning. In this process a metal sheet or tube is rotated at high speed and deformed by a mandrel.

Both fabrication methods result in a reduced and non uniform wall thickness and suffer from spring back. Spring back is characterised by partial relapse of the cavity shape after releasing the load of forming, due to elastic deformation of the part and plastic deformation of the punch. The geometry of cavities formed by deep drawing is known to be rather sensitive to spring back. A analysis on 17 1.5 GHz cavities showed deviations of the resonance frequency on average of 2.8 MHz with a maximum of 4.2 MHz from the target and field flatness deviations in the order of 20 % with a maximum of 51 % [28]. Besides reliably producing cavities meeting the mechanical requirements and tolerances, the electron beam weld is often associated with performance limitations. Typical limitations include quenching in the heat affected zone close to the weld, weld features, and contamination originating in the welding process [11, 29, 30, 31].

For niobium film cavities, it is desired to coat seamless substrate cavities to avoid adhesion issues and to avoid altered film growth on the recrystalised zone. Moreover, EBW is a cost driver of the cavity fabrication. For these reasons, the fabrication of seamless niobium and copper cavities is considered worthwhile.

In order to overcome the limitations and drawbacks of the standard fabrication methods, so called high strain-rate forming processes are under investigation. Within a collaboration between CERN and Bmax, electro-hydraulic forming is being pursued, which is based on a high power arc discharge in water [32]. The resulting shock wave plastically deforms the metal sheet against the forming die at high impact speed in the order of 50 m/s to 200 m/s. Repeated shocks allow for the seamless forming of the cavity geometry.. This process also allows the fabrication of structures with fine details and sharp edges, might supersedes heat treatments and has a low overall energy consumption.

An alternative to forming a structure from metal sheet is additive manufacturing. For metal objects, the metal powder is melted layer-wise by a high power laser or an electron beam according to a CAD model. This process allows a maximum freedom for design with a minimum of required material and is especially interesting for higher order mode and fundamental power couplers as well as exotic cavity geometries like crab cavities. This process is still in its infancy, and key issues for high performing SRF structures are the density of the object and the quality of the powder. A first attempt of manufacturing two 3.8 GHz cavities from niobium powder yielded 170 nΩ resp. 2.5 μΩ residual resistance and quench fields of 3 MV/m resp. 2 MV/m [33], which are well below state-of-the-art performance of bulk Nb.

2.2. Beyond Bulk Niobium

In order to overcome the technological limits of bulk niobium cavity production, alternative manufacturing processes and materials are currently under survey. The potential benefits are extensive: Both in terms of material and fabrication cost savings, but also as accelerator operations costs may be significantly reduced. Alternative materials with higher critical temperature have lower BCS resistance

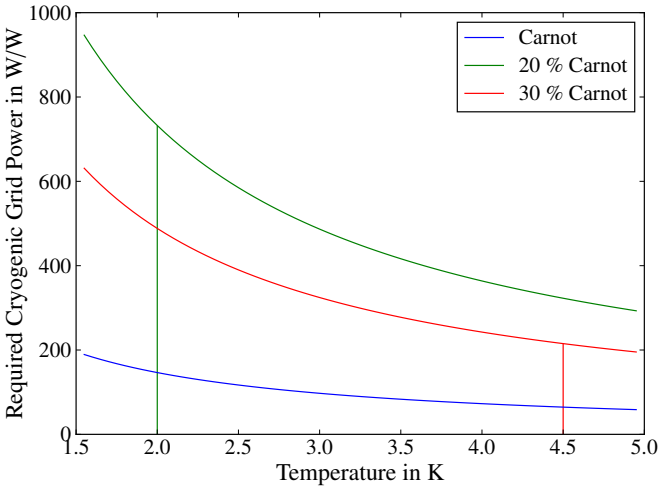

Figure 2.4.: Required cryogenic grid power per dissipated W as function of operating temperature.

compared to bulk niobium at the same frequency and temperature. A significantly lower BCS resistance would reduce dissipative losses in the cavity, and so favour operating at 4.5 K instead of 2 K. This would lower the refrigeration costs and simplify the layout of the entire cryogenic plant and hence reduce the installation costs of the refrigeration system.

The minimal cryogenic power consumption is defined by the carnot efficiency and depends on the ambient temperature T_{ambient} and the operation temperature T_0:

$$\eta_{\text{carnot}} = \frac{T_0}{T_{\text{ambient}} - T_0} \tag{2.2}$$

Figure 2.4 shows the required grid power for a cryogenic installation per 1 W dissipated power assuming an ambient temperature of 20 °C. The most efficient refrigeration systems to date however have a technical efficiency of 20 % at 2 K and 30 % at 4.5 K as indicated by the green and red line in the plot. With these efficiencies the required cryogenic power at 2 K is a factor of 3.4 higher than the required power at 4.5 K for the same heat load.

From the cryogenic operations and efficiency point of view, an operational temperature of 4.5 K is favourable over 1.8 K to 2 K. However, it must be kept in mind that liquid helium changes its properties drastically when becoming superfluid below the lambda point $T_\lambda = 2.17\,\text{K}$. Below T_λ the thermal conductivity of liquid helium increases by more than six orders of magnitude [34]. For operation at temperatures above T_λ, very good thermal stability has to be ensured by the cavity material.

In additional to the thermal and superconducting properties also normal electrical properties as well as mechanical properties have to be considered when assessing a new material for superconducting RF applications. In this context, bulk materials need to satisfy all thermal, mechanical and SRF requirements while the concept of a micrometer thin superconducting coating decouples the requirements of the bulk substrate from the requirements for the RF surface. The coating parameters may allow tayloring the superconducting properties of the layer for optimal SRF performance, while the thermal stability is provided by the substrate which will not be exposed to the RF if the superconducting coating is sufficiently thick. It goes without saying that the mechanical integrity has to be sustained for substrate as

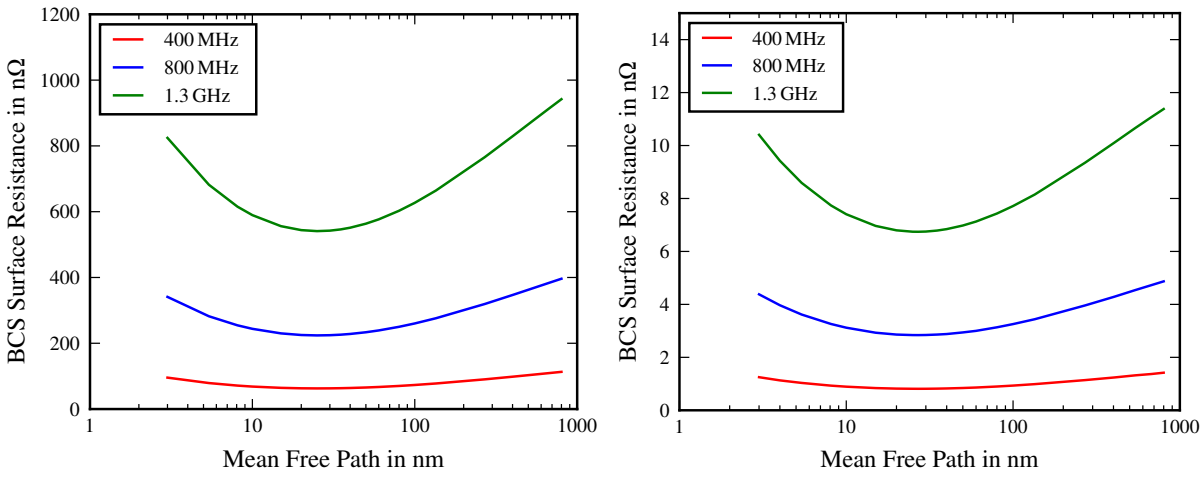

Figure 2.5.: Calculated BCS surface resistance for standard niobium at (a) 4.5 K and (b) 2 K.

well as the thin film.

2.2.1. Niobium Films

In terms of material properties, the BCS resistance does not only depend on the critical temperature of a material but also on the mean free path, as will be discussed in detail in Section 3.1. The surface resistance of a niobium cavity can be optimized by tuning the mean free path. For very long and very short mean free paths, the BCS resistance increases, while having a minimum at around 20 nm to 40 nm which corresponds roughly to a residual resistance ratio RRR of 10 to 30. Figure 2.5 shows the BCS resistance at 2 K and 4.5 K as a function of mean free path for 400 MHz, 800 MHz and 1.3 GHz assuming a London penetration depth of 32 nm and a coherence length of 39 nm as literature values for Nb [35]. The BCS resistance was calculated using WinSuperfit [36] which is based the FORTRAN code by Halbritter [37], and handles the full BCS theory. The BCS resistance increases strongly for higher frequencies when moving away from the minimum due to its quadratic dependence. Especially for higher frequencies and higher temperature the optimization of mean free path holds huge potential gain for a reduction of the BCS resistance. At 2 K the difference on R_{BCS} is significantly lower; but since the overall surface resistance is in the order of several nΩ, a mean free path optimisation still has a non-negligible effect for frequencies above 1GHz.

A low (bulk) mean free path, however, comes with a low thermal conductivity since both quantities are proportional to each other. For that reason, bulk niobium cavities made from medium quality material (residual resistance ratio RRR ≈ 50), as was common in the 1970s and 1980s, quenched due to thermal breakdown at rather low fields [35]. Instead of moving to high RRR material by purifying the bulk material, and paying the price of higher BCS resistance (and higher production cost) as a result, CERN proposed to coat a few µm thick niobium layer onto a copper cavity [38]. Due to the short penetration depth of niobium, the RF field will not penetrate the copper, and so the losses of the cavity will be given by the surface resistance of the superconducting material while high quality copper ensures thermal stability even at 4.5 K. Moreover, the coating process allows tuning the mean free path towards the BCS

Table 2.1.: Operating accelerating gradient and Q_0 for the four accelerators using niobium coated cavities. All machines run/ran at 4.5 K.

	Installation/Operation	Frequency	E_{acc} in MV/m	Q_0 at operating field	Ref.
LEP	1989[1] - 2000	352 MHz	6	$3.2 \cdot 10^9$	[2]
ALPI	1995[2] - present	160 MHz	4.6	$2 \cdot 10^8$	[39]
LHC	2009 - present	400 MHz	5	$2 \cdot 10^9$	[40]
HIE-Isolde	2015	101 MHz	6	$5 \cdot 10^8$	[41, 42]

minimum through the specific coating parameters.

Besides cryogenic loss considerations, there are applications that may favour Nb/Cu over bulk Nb for other reasons: Particle colliders that suffer from high losses due to higher order modes require low frequency cavities such as 352 MHz (LEP) or 400 MHz (LHC and the FCC study) and favour large beam tube apertures. Building such large objects from bulk niobium would require a huge amount of raw material which might be cost prohibitive or unavailable (see Section 2.1.3). Moreover, the heat load in the higher order mode couplers might favour operation at 4.5 K where high thermal stability of the material is crucial. What is more, the high thermal conductivity of copper allows to increase the cavity wall thickness in order to mitigate microphonics. Lastly, Nb/Cu cavities simplify the cryostat design: Niobium films are known to have a very low sensitivity to trapped magnetic flux so that magnetic shielding of a cavity can be discarded without increasing the residual resistance.

Despite all these advantages, niobium coated cavities have found application only in few accelerators: LEP and LHC as high energy particle colliders and ALPI and HIE-Isolde as heavy ion accelerators; Table 2.1 summarizes the operation parameters of these four Nb/Cu accelerators.

The reason for this is the strong increase of surface resistance with increasing accelerating field, referred to as *Q-Slope*. The increase is often exponential in field and limits the application to accelerating gradients below 10 MV/m across the whole (SRF typical) frequency range.

Figure 2.6 shows a typical production flow chart for a niobium coated copper cavity. In the context of cavity fabrication, the complexity of production and preparation of the copper substrate cavity is comparable to the production and preparation of a bulk niobium cavity. Bulk niobium cavity half cells are conventionally deep drawn and electron beam welded together. The production of seamless bulk niobium cavities is today subject to research and development activities since electron beam welding is expensive, requires a high level of expertise and is error-prone. In addition to the disadvantages of EBW, it is preferred to produce copper cavities from spinning in order to avoid coating on the electron beam welding seam. After fabrication a copper cavity is exposed to (electro-)chemical (EP or SUBU) and heat treatments in order to remove the damage layer from fabrication and to remove contamination and dissolved gases from the bulk material. Due to the fact that typical films are less than 10 µm thick, it is evident that the repair of defects has to be done already on the copper cavity. Any fault in or under the micrometer thick coating requires stripping the film off the substrate, repair and then re-coating the copper cavity. Prior to coating, the cavity has to be high pressure rinsed with ultra-pure water in order to remove any dust particles and other contamination that would affect the niobium film quality and/or adhesion. The coating process involves a bake-out up to 600 °C, for elliptical cavities typically

[1] The majority of Nb coated cavities was installed in 1992 [43]
[2] First installation of Nb coated cavities [44]

about 150 °C as a degassing step. Elliptical copper substrates serve here as the main part of the vacuum chamber while other geometries need to be mounted in a separate vacuum chamber. After coating, the cavity is again high pressure water rinsed and can then be cold tested in the same way as any bulk niobium cavity. If specifications are not met, the cavity can be rinsed again if the limitation was field emission. If the cavity performance is limited by the film itself, for example by peel-off or high residual resistance, the film has to be removed and the substrate can be coated again.

2.2.2. Alternative Materials

In the quest for alternative materials for SRF applications, several material properties need to be considered. The BCS surface resistance, R_{BCS}, decreases exponentially with T/T_{c}, but also increases with (at least) the third power of the penetration depth ($\sim \lambda^3$). The residual resistance, R_{res} was empirically found to be proportional to (at least) the square root of the normal state resistivity. The ideal candidate would therefore be a material with low resistivity, small penetration depth and high T_{c}. Also it should be noted that a very short coherence length which describes the interaction length scale of the cooper pairs will lead to a higher sensitivity towards surface defects the smaller the coherence length is.

Moreover, a higher critical field would allow reaching higher accelerating gradients. However, it is not the upper critical field that is of interest but the superheating field. As will be discussed in Section 3.3, the superheating field is related to the thermodynamic critical field which is inversely proportional to the product of penetration depth λ and coherence length ξ: $H_{\mathrm{c}} \sim 1/\lambda\xi$. Depending on the Ginsburg-Landau parameter ($\kappa = \lambda/\xi$), the superheating field of a type II superconductor will be as high as $0.85\,\mathrm{H_c}$ to $1.2\,\mathrm{H_c}$.

Besides the superconducting properties, mechanical, thermal and chemical properties need to also be considered. An ideal SRF material would therefore be ductile, have a good thermal conductivity and be chemically stable in both air and water and from room temperature down to cryogenic temperatures. In the context of coating techniques, materials of two or three components are favourable as the process becomes excessively complex with increasing number of deposition constituents. In addition, the phase diagram of the material system of interest should allow a certain range of right stoichiometry before the superconducting properties are lost. Finally, each constituent component should be easily available and at moderate cost.

From the large number of superconducting materials, only few are therefore potential candidates for SRF applications. High critical temperature superconductors (HTS) like YBCO or BSCCO have high critical temperatures but very large and anisotropic penetration depths (up to 1 µm) and a very short coherence length typically of order of 1 nm. Moreover, they have a complex crystal lattice with at least four components. These materials are also ceramics, so the thermal conductivity is very low, and the material is brittle. For these reasons, high temperature superconductors are not considered for SRF cavities.

In contrast to HTS, low temperature superconductors offers several potential candidates, which all belong to the A15 or B1 compounds. A15 materials are compounds with three atoms of a transition metal and one atom of any element. Of special interest for SRF applications are Nb_3Sn, Nb_3Al, Nb_3Ge and V_3Si which have all critical temperatures between 15 K and 20 K. Unfortunately A15 alloys are characteristically very brittle, which prohibits mechanical forming after the film was deposited. It is also not

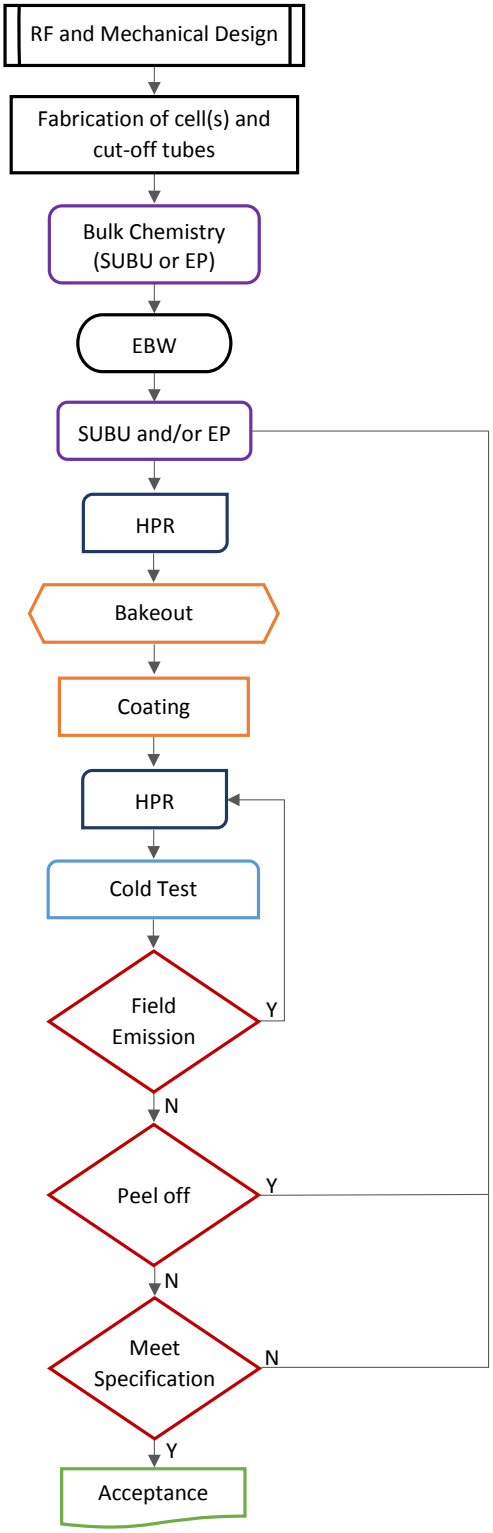

Figure 2.6.: Typical production flow chart of a niobium-on-copper cavity.

clear yet if mechanical tuning of a cavity will affect the film. B1 compounds consist of one metallic and one non-metallic element which form a face centred cubic (fcc) lattice in which the non-metallic atoms sit on interstitial sites forming octahedrons. Potential candidates due to higher T_c are NbC and NbN. Further, adding titanium to the NbN lattice was found to improve the thermal conductivity and lower the normal state resistivity without suppressing the superconducting properties. Therefore, also NbTiN is a promising SRF material. Similarly, Magnesium-Diboride, MgB_2 has recently been considered for SRF application due to it remarkably high critical temperature of 39 K. The high T_c might allow for using cryocoolers instead of bath cryostats. However, MgB_2 exhibits anisotropy of the superconducting energy gap and it is not clear if this will be an issue. Moreover, it is known to degrade under humidity [45].

As can be seen, what all materials have in common is that the relevant properties are only vaguely know and might depend on the deposition technique. With the exception of Nb_3Sn, there are only few SRF measurements due to the fact that the potential materials cannot be deposited onto a complex geometry like a cavity yet.

Nb_3Sn

Niobium-tin combines high critical temperature (18.1 K) with a low normal resistivity and is therefore a promising candidate as an SRF material. Due to its brittleness the cavity geometry has to be formed first and then the Nb_3Sn layer has to be deposited onto the final shape. As the thermal conductivity of Nb_3Sn is low the deposited layer must be thin and thermally well connected to the substrate.

The first attempt to apply Nb_3Sn to an SRF cavity was made in the 1980s in a collaboration between Siemens Research Laboratories Erlangen and the Universität Wuppertal in Germany. Since then, accelerating gradients of about 10 MV/m with a Q about 1×10^9 at 4.2 K have been achieved repeatedly using a vapour diffusion technique [46, 47]. The *Wuppertal recipe* served as a basis for the recent Nb_3Sn programme at the Cornell University where improvements in the coating process yielded Q values of 1×10^{10} at 12 MV/m and 4.2 K on a 1.3 GHz elliptical cavity. Quenching due to a defect limited cavity performance to a surface magnetic (peak) field of 55 mT [48].

NbN & NbTiN

The B1 compound Niobium nitride, NbN, is one of the binary compounds with the highest critical temperature (17.3 K) and has been studied for SRF applications by numerous labs. The critical temperature of NbN depends strongly on the stoichiometry, and the superconducting phase is only metastable at room temperature [49]. For the fcc lattice, where the nitrogen atoms sit on interstitial sites, vacancies are typical which results in a relatively high normal resistivity compared to other SRF candidates [50].

Mixing NbN and TiN creates the ternary compound NbTiN which is also superconducting. The Ti atmos serve as a nitrogen getter which reduces the number of vacancies and therefore improves the metallic behaviour [49]. Additionally, the TiN phase is stable at room temperature, which contributes to stabilising the whole compound. The critical temperature is however as sensitive to the N stoichiometry as NbN. To date, the best SRF performance of NbTiN has been achieved on a 120 mm diameter copper disc, characterised in a TE011 cavity at 4 GHz [51]. The NbTiN film showed a decent residual resistance

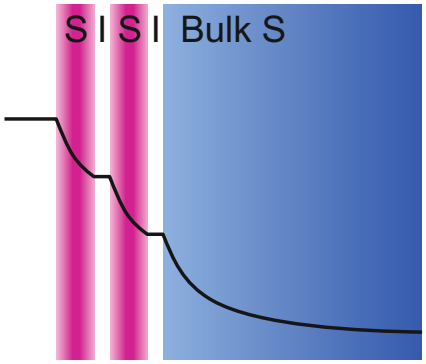

Figure 2.7.: Concept on how S-I-S multilayer shield the RF field from the bulk Nb cavity to reach higher accelerating gradients.

at low field but suffered from a strong increase of surface resistance with field: the surface resistance at 1.6 K increased from 40 nΩ to 500 nΩ at 34 mT and was limited by quenching [52].

MgB_2

High quality magnesium diboride (MgB_2) coatings were successfully produced by reactive evaporation [53] at Superconductor Technology Inc. (STI), and by hybrid physical–chemical vapour deposition [54] at Temple University on various substrates.

While direct current (DC) measurements like T_c, vortex penetration measurements [55] and DC resistance measurements [53] have been performed there are very few RF measurements available. The reason for that the MgB_2 sample size is limited to a few centimetres. Still, one set of RF surface resistance measurements is available for each supplier: STI samples with a 5 cm diameter and on different substrates where characterised in a strip-line resonator at 2 GHz or in a dielectric resonator at 10.7 GHz[56]. Quadratically scaled down to 1.5 GHz, the surface resistance obtained is in the order of 1 μΩ at 5 K [57]. Additionally, the surface resistance appeared to be weakly dependent on the RF magnetic field up to 30 mT, which would correspond to 7 MV/m for a standard TESLA shape cavity.

A 5 cm MgB_2 single crystal on sapphire sample produced at the Temple University was characterized in Jefferson Labs surface impedance characterization (SIC) system [58] at 7.5 GHz, and a surface resistance of (9 ± 2) μΩ at 2.2 K is reported [59].

SIS Multilayer

In order to reach higher accelerating gradients, A. Gurevich proposed in 2006 to coat bulk niobium cavities with multilayers, alternating superconducting (S) and insulating (I) layers [60]. By choosing a material with higher critical temperature and higher thermodynamical critical field than bulk niobium for the superconducting layers and a thicknesses less than the penetration depth of niobium the superconducting layers can remain in the Meissner state at magnetic fields higher than their bulk lower critical field value. The thin layer increases the threshold for first vortex penetration of parallel fields while the underlying bulk niobium shields from perpendicular vortex penetration. The insulation layers act as Josephson junctions and decouple the superconducting layers from each other. Since vortices cannot exist in the insulating layer, the layer shields the bulk superconductor from severe vortex dissipation

losses.

The magnetic field decays exponentially in the superconducting layers as sketched in Figure 2.7 and the layer thicknesses are chosen so that the bulk niobium substrate remains in the Meissner state [60]. A single layer of Nb_3Sn of optimal thickness could increase the accelerating gradient in a typical elliptical cavity by more than a factor of 2, but also NbN [61], NbTiN [62] and MgB_2 [63] are pursued for multilayer structures. Even a thin dirty niobium coating could increase the quench field by 20 % [64].

First experimental results are available for a sample of 25 nm NbN on 14 nm MgO on 250 nm niobium, all dc magnetron sputtered. The sample was characterised by dc magnetisation measurements (SQUID) and showed an enhancement of first flux penetration by a factor of 5 compared to a 250 nm thick niobium film sample as reference [61].

2.3. Thin Film Growth

Deposition techniques for Nb/Cu as well as for alternative materials are subject to several research activities around the world. For good superconducting properties contamination with foreign materials and gases has to be kept at very low level, often in the ppm range. Therefore, industrial coating techniques such as electroplating are not suitable for SRF films. Only physical vapour deposition (PVD) and chemical vapour deposition (CVD) techniques, and their hybrids, are considered clean enough and are currently under investigation.

Niobium deposition via CVD is usually based on the reduction of niobium halides like $NbCl_5$, NbI_5 or $NbBr_5$ to form a niobium coating. Although attempts have been reported for coating of an SRF cavity from CVD [65, 66, 67], there is no RF data available yet. Atomic layer deposition (ALD) as a subclass of CVD has recently gained attention for SRF thin films [68]. Due to the intrinsically very slow process with typical deposition rates of order 100 nm/h, ALD is of highest interest for very thin films such as the insulating layers of the S-I-S structures. This implies that the attention will be on PVD techniques, but before discussing the most advanced (PVD) techniques for SRF cavities, basic aspects of thin film growth are presented, all be it with a focus on the deposition of niobium on copper.

2.3.1. Film Growth

In physical vapour deposition of metals, ions, molecules or atoms are created by evaporation or sputtering, and the film grows from the gas phase. While atoms travel ballistically, ions and molecules can be guided by electric and/or magnetic fields towards the substrate where they condense, diffuse on the surface or into the bulk, bond to a surface atom or are re-emitted to the vacuum. Nucleation on the substrate is triggered by low energy sites such as defects or foreign particles.

Species mobility on the surface is given by the substrate temperature, the energy of the arriving species and the deposition rate, i.e. the number of arriving species per second.

Depending on process parameters, the properties of the substrate and the deposited material, the film can grow in different modes: In the island growth mode, the particles interact strongly with each other. The arriving species build up islands which grow laterally and normal to the surface and merge to a continuous film. As with most metals, niobium grows in the island mode.

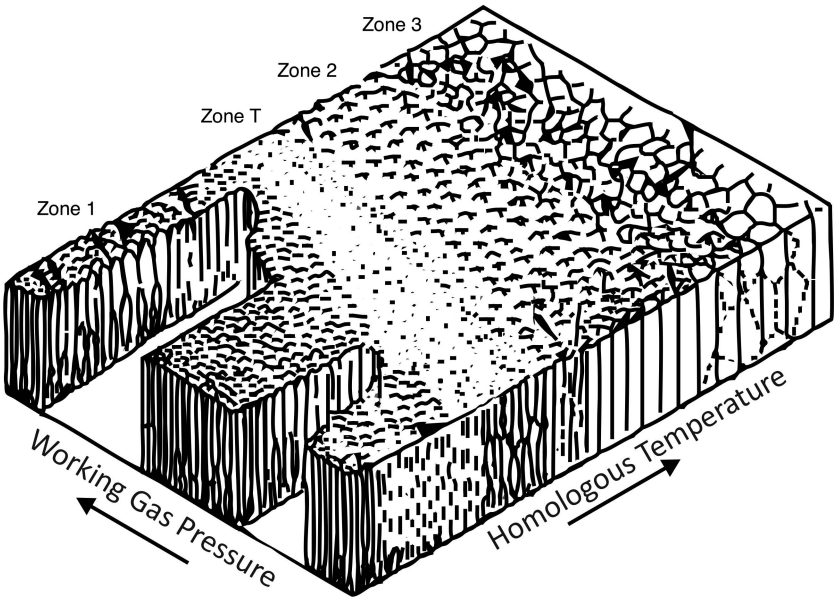

Figure 2.8.: Structure zone diagramme after Thornton [69].

In the layer-by-layer mode, the condensed atoms interact strongly with the substrate, forming a two dimensional layer first, then growing normal to the surface. If the difference in bonding energies between adatoms and substrate atoms is not too big, the film might grow in the mixed mode: starting in the layer-by-layer mode followed by the island growth mode as soon as the substrate is covered by a few monolayers such that the interaction between adatoms and substrate is negligible.

The microstructure of the film is a result of different potentially competing processes and interactions between deposition material and substrate as well as the general coating conditions. Four main coating parameters dominate the morphology of a film:

- the homologous temperature, i.e. the ratio of substrate temperature and melting temperature of the deposited material.
- the partial pressures of the base vacuum[3].
- the deposition rate of the arriving species.
- the energy of the arriving species.

Based on these parameters the different resulting microstructures can be qualitatively described in a structure zone diagram with the Thornton diagram being the most prominent one [69]. As shown in Figure 2.8, it illustrates the film growth in magnetron sputter deposition with the homologous temperature and the working gas pressure as the main process parameters.

Alike to precedent publications and diagrams four structural zones are identified: Porous and/or amorphous films with a high density of dislocations grow for low homologous temperatures and low particle energy (high pressure) as the adsorbed particles have low surface mobility (Zone 1). If the particle mobility is increased, e.g. by decreasing the working gas pressure (Zone T) or by a higher

[3]Vacuum level before the coating process is launched; in particular before adding a working gas

substrate temperature (Zone 2), columnar grains with denser grain boundaries but still high dislocation density are created. In zone 2, the dislocations are mainly located at grain boundaries. The transition zone (Zone T) is moreover characterized by V shaped grains due to significant surface diffusion but still limited grain boundary diffusion which leads to competing grain growth. Increasing mobility further will promote bulk diffusion (Zone 3). It is characterised by a recrystallised grain structure with dense grain boundaries and a low dislocation density.

2.3.2. The Role of the Substrate

The morphology of a film depends also on the condition of the substrate. If the substrate is amorphous, the film is likely to grow as fibres or columnar while the film grows epitaxially on a crystalline substrate. In case of a single crystal substrate, a single crystal film can be expected while a polycrystalline substrate will result in a polycrystalline film. Moreover, lattice mismatch, thermal expansion coefficients, miscibility and surface roughness influence the film growth. A high lattice mismatch or big difference in thermal expansion will result in a high level of stress within the film. If two materials have a high diffusivity and are miscible, they will form an alloy rather than two distinct layers. A diffusion barrier might be necessary to inhibit mixing. The film surface roughness is driven by the process parameters but cannot be less than the roughness of the substrate surface.

In the context of coating SRF cavities, the standard scenario is depositing 1 µm to 2 µm niobium onto a copper cavity which corresponds to 10 to 20 superconducting penetration depth lengths. Since typically the surface area is in the order of 1 m^2, the coating will always be on polycrystalline copper. Niobium and copper are not miscible and therefore do not require a diffusion barrier. However, Niobium may be deposited on the native amorphous copper oxide which acts as a diffusion barrier or on oxide free crystalline copper which can be created by dissolving the oxide via baking or sputtering, i.e. high energy ion bombardment. Due to their immiscibility in combination with a lattice mismatch of about 10 %, achieving good adhesion is delicate. However, if a strong interface is achieved, adhesion is excellent and Nb/Cu films withstand repeated high pressure rinsing and thermal cycles between room and cryogenic temperatures without any signs of deterioration.

As the SRF films are in the order of 1 to 2 µm, any surface feature or defect will be copied to the film. Hence, a well defined substrate preparation prior to coating is crucial. Especially indentations hold the risk of shadowing areas which then will not be coated or result in abnormal film growth. Mechanical polishing followed by an electro-polishing are therefore considered state-of-the-art preparation. Moreover, any residue from the chemical preparation and contamination from lab air has to be thoroughly removed as it will be incorporated by the film, diffuse into the film or even suppress adhesion between film and substrate. Rinsing with ultra pure water prior to coating is therefore mandatory often following a cleaning with detergents to remove chemistry residues.

2.4. Deposition Techniques

In sputter deposition, neutral atoms condense on the substrate after they have been ejected from the cathode by energetic ions in the plasma. Typical particle energies are in the range of a few eV and the surface mobility is dominated by the substrate temperature. As the standard substrate for SRF cavities is

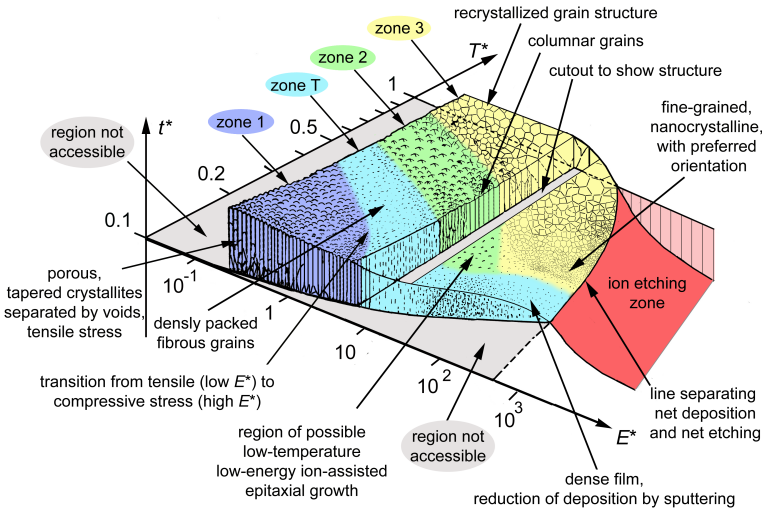

Figure 2.9.: Structure zone diagram for energetic condensation developed by A. Anders [72].

copper due to its high thermal conductivity and its good mechanical properties, coating temperatures are limited to about 400 °C for a cavity with a wall thickness 2 to 3 mm due to the low melting temperature of copper. In order to promote high quality film growth additional energy has to be supplied to the deposition material. Energetic condensation techniques create ionised species at high and low energies. Higher particle energies are expected to lead to improved microstructure and denser films. Moreover, ions can be accelerated (or decelerated) to a certain energy and can be guided by electrical bias an/or magnetic fields. The latter might improve coatings on low beta elliptical cavities [70] or even enable coating more complex geometries like crab cavities [71].

Based on the Thornton structure zone diagram, A. Anders proposed a modified structure zone diagram for energetic condensation which is displayed in Figure 2.9 [72]. The homologous temperature is replaced by a generalized temperature T^*. In addition to the homologous temperature it accounts for an additional temperature shift due to the potential energy of the arriving particles. This potential energy represents the cohesive energy of any condensed particle and the ionisation energy less the work function for arriving ions. It therefore describes also energy deposited in the film by particles that are instantly re-emitted to the vacuum.

The pressure axis in the Thornton diagram describes the effect of the kinetic energy of the arriving atoms and takes the number of collisions with the working gas into account. In energetic condensation processes the kinetic energy comprises of an initial energy from the plasma and the energy gain of ions between plasma and substrate. Therefore the pressure axis is replaced by a generalised energy axis E^*. The third axis was free in Thorntons version and represents now the net film thickness t^*. It illustrates the evolving microstructure with thickness and even includes ion etching, i.e. a negative thickness.

2.4.1. DC Magnetron Sputtering

Direct current magnetron sputtering (DCMS) is the standard deposition technique for SRF cavities and is sketched in Figure 2.10. The copper substrate serves as the anode while the niobium target serves as cathode. Both are placed in ultra high vacuum. A high (DC) voltage applied on the cathode in

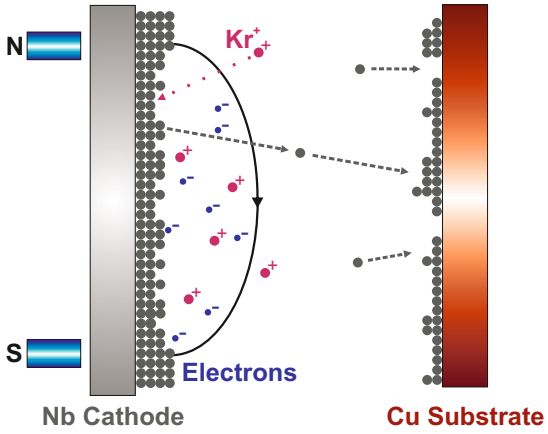

Figure 2.10.: Principle of the DC magnetron sputtering: Energetic ions from the working gas bombard the cathode's surface. Emitted cathode atoms are deposited in line of sight on the substrate. A magnetic field is used to concentrate the plasma around the cathode and therefore increase the plasma density resp. deposition rate. For high power impulse magnetron sputtering (HIPIMS) the continuous moderate DC power is replaced by a high power pulse in order to ionise the cathode material.

combination with the introduction of a working gas ignites a plasma. The resulting sputter gas ions, a noble gas unless a chemical reaction is desired, bombard the surface of the cathode and emit neutral niobium atoms. Permanent magnets on the back side of the cathode concentrate the plasma electrons close to the target and enhance the density of the plasma which in turn increases the energy density on the cathode's surface. As a result the deposition rate is increased which reduces the risk of incorporating sputter gas and residual gases from the vacuum into the film.

In the late 1990's CERN launched an exhaustive study on elliptical 1.5 GHz cavities involving dozens of cavity coatings. The study focussed on the influence of coating parameters such as type and mixtures of the working gas(es) and the surface preparation on the BCS and residual surface resistance and the Q-Slope [13]. Although argon is the standard sputter gas, krypton was found to be the best choice for the deposition of niobium on copper due to a better atomic mass ratio[4] with respect to the niobium atoms. The cavity coating exhibit fibrous growth on oxidised copper and epitaxial films on crystalline copper. Although the microstructure of unoxidised copper is of higher quality, the coatings on oxidised copper gave better RF results . Diffusion of residual gases from the copper into the thin niobium layer would be a possible explanation as the copper oxide layer might serve as a diffusion barrier. On oxidised copper residual resistances of a few nΩ were repeatedly achieved but the exponential increase of surface resistance with RF field could not be mitigated.

2.4.2. High Power Impulse Magnetron Sputtering

HIPIMS is the energetic condensation variant of the regular sputter deposition. The components and their arrangement are as in the DC magnetron sputtering, except for the supplied power. Instead of having a constant voltage on the cathode in the order of hundreds of volts, HIPIMS applies high power (im)pulses in the order of 1 kV over a pulse length of a few hundred µs. As a result the power densities

[4]The atomic mass ratio of argon to niobium is 0.43 compared to the atomic mass ratio of krypton to niobium is 0.90

on the target increases from a few W/cm^2 to a few kW/cm^2 and a highly dense plasma with neutrals and mainly singly and doubly charged ions with a ionization degree between 30 and 100 % is created [73, 74]. The duty cycle is adjusted to maintain the average power of the magnetron sputtering to avoid overheating the (copper) substrate. Although HIPIMS processes without a working gas are in principle possible, the sputtering yield of niobium appears to be too low so that for the deposition of niobium the process keeps on relying on a working gas with the risk of incorporation into the film [74]. This is of special importance as the main disadvantage of HIPIMS is the low deposition rate. Early HIPIMS coatings without any substrate bias of 1.3 GHz cavities reached the performance of the typical magnetron sputtered niobium films and the development is ongoing for further improvements and at different laboratories with CERN, JLab and LBNL being the biggest ones. Cross section SEM images show that unbiased HIPIMS coated samples are not different than standard DCMS coatings: Crystals grow in fibres at the incident angle of the arriving particles. Samples coated with biased HIPIMS however show crystal growth normal to the surface, also when coated at a 45° angle [75]. This is of high importance for low-β elliptical cavities which have particularly steep cell slopes. Yet, crystals still grow as tens of nm fibres.

2.4.3. Electron Cyclotron Resonance

The ECR is commonly used as a plasma generator and ion source not only for scientific purposes but also for a variety of medical and industrial applications. The principle is based on superposing a microwave field with a static and uniform magnetic field perpendicular to the RF oscillating plane. Free electrons will be accelerated by the electric field component of the RF field while the static magnetic field will bend the electrons onto a circular path. As a result, any electron will follow a helicoidal trajectory with increasing radius. In the absence of an electric field the circular motion of the electron is described by the Lamor radius and the associated (angular) frequency is

$$\omega_{\text{Lamor}} = \frac{eB}{m_{\text{e}}} \tag{2.3}$$

where m_{e} and e are the electron's mass and elementary charge and B describes the static magnetic field. If the microwave frequency matches the Lamor frequency, then the resonance condition is fulfilled: If the energy loss due to collisions is negligible, the electrons are continuously accelerated by the microwave field until their energy is sufficiently high to ionize surrounding atoms or molecules. The created discharges ignite a plasma which can be stabilized with enough microwave power.

As an industrial standard the typical frequency for an ECR system is 2.45 GHz which results in a required static magnetic field of 87.5 mT.

For ECR thin film deposition, the ECR ignites a plasma from the vapour of the deposition material inside a UHV chamber in which the substrate is placed. The created ions can be extracted from the plasma in order to condense them on the substrate by biasing it.

ECR deposition of niobium films has several big advantages over standard magnetron sputtering: The ECR creates mainly singly charged niobium ions. If the substrate is placed out off line of sight and the ions are extracted from the plasma by biasing, the film is built up only from niobium ions. Moreover, the energy of the ions can be varied in order to optimise the film's microstructure. In addition, no working gas is required and therefore only background gases can be incorporated into the film. This is

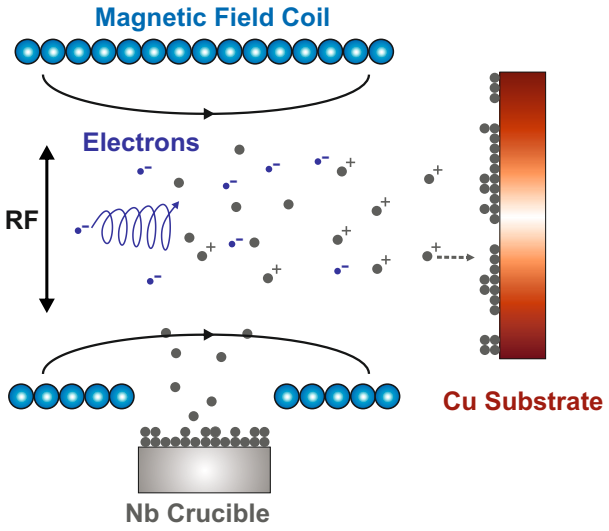

Figure 2.11.: Principle of the ECR plasma deposition: A static magnetic field is superimposed with an RF field. If the resonance condition is met, free electrons are accelerated beyond the ionization threshold and a localised niobium plasma is created. Niobium ions are extracted towards the substrate by biasing the latter.

however marginal if the base pressure in the coating chamber is sufficiently low. The disadvantage is the complexity of the coating system, in particular with regard to extracting and guiding the niobium ions into a cavity.

ECR Deposition of Niobium at Jefferson Lab

The ECR is used at JLab for the deposition of high quality niobium films on flat samples [49]. The system works at the typical ECR frequency of 2.45 GHz with a maximum RF power of 1.5 kW. The RF power is coupled into a cylindrical vacuum chamber through a ceramic window. The ECR chamber is surrounded by two neighbouring coils which provide the static magnetic field. Various metallic and insulating substrates of different sizes may be coated. The samples are placed at the end of the ECR chamber on a sample holder that can be independently biased and heated up to 700°. The static plasma potential is 64 eV. Neutral niobium vapour is produced by evaporating material from a high quality niobium crucible with an electron gun and flows into the ECR chamber. As indicated in Figure 2.11 all components are arranged in a way that the ECR condition is met in the region of the niobium vapour and only niobium ions reach the substrate.

The influence of various quantities on the niobium film quality has been studied vigorously covering pre-deposition bake-out temperature, coating temperature and ion energy as well as the influence of different substrates [49]. A variety of cryogenic methods (critical temperature, RRR, superconducting energy gap) and surface characterisations in order to investigate the microstructure of the film and the interface, crystallinity and chemical composition has been employed.

It was found that niobium grows epitaxial on crystalline substrates with a preferred crystal orientation depending on the orientation of the substrate [76]. Moreover, the niobium film reproduces the grain structure of the underlying substrate. On amorphous substrates, niobium exhibits fibre growth normal to the surface with fibre diameters in the nanometre range.

The RRR can be tuned by tuning coating temperature and ion energy, i.e. bias voltage [77]. RRR values up to 640 on single crystal Al_2O_3 have been obtained. On polycrystalline copper typical RRR values range between 50 and 300.

Secondary ion mass spectrometry (SIMS) depth profiles gave insights about the impurity content in the film. The studied films showed less nitrogen, more carbon and comparable oxygen levels compared to large grain bulk niobium [49]. Hydrogen is of special interest for the SRF performance as it leads to the formation of niobium hydrides which are associated with RF losses. The measured hydrogen content in the niobium films varied by two orders of magnitudes depending on RRR with higher H content for lower RRR. However, the higher level was still four orders of magnitude lower than for bulk niobium which agrees well with measurements on niobium films by cathodic arc deposition (CAD) [78].

The superconducting energy gap can be measured by point contact tunneling spectroscopy [79]. In this technique the conductance curve (dI/dV) ist measured as function of voltage V across an area of about 10 µm. Since this is a local measurement, several points across a sample are probed with a distribution of gap values as a result.

Niobium films deposited on large grain copper showed gap values comparable to bulk niobium while fibre grown films (on oxidised copper) showed a reduced gap [80, 49]. A film grown in two steps, i.e. at higher energy for the nucleation phase and at lower energy for the subsequent growth, showed a distribution around two superconducting gap values. As cross section transmission electron microscopy (TEM) could not reveal any change in microstructure through the two films it is argued that the two gaps might be due to different levels of oxygen or hydrogen across the depth of the film.

Surface resistance measurements were done on samples with 5 cm diameter in JLab's Surface Impedance Cavity (SIC) working at 7.5 GHz [81]. Measurements of the surface resistance as function of temperature at fixed field are compared for different coating schemes. A clear trend was found between the (low field) residual resistance and the ion energy, leading to lower resistance as the energy increases [80]. Moreover it was found that two staged coating, i.e. high energy during the early growth stages of the film followed by a lower energy subsequent growth, leads to lower resistance than growing the film entirely at high ion energy [49]. This is attributed to a lower defect density during the lower energy deposition after a film template has been formed by the higher energetic ions. Also no significant difference between a large grain film and a single crystal film was found. Nevertheless, significant losses are expected if grains are not well connected.

2.4.4. Cathodic Arc Deposition

The deposition of niobium on copper using a cathodic arc discharge is currently pursued by Alameda Applied Science Corporation (AASC) [82] and is sketched in Figure 2.12. A high current arc is ignited in a spot of the niobium cathode evaporating material which is emitted to the vacuum. The arc creates neutrals, ions of mainly triple charge, clusters and macro particles which might be deposited on the substrate. Adding coils for the creation of a static magnetic field allows separating ions from neutrals and macro particles. The power density is very high leading to a high ionisation degree between 30 and 100 %. Due to the fact that cathodic arc deposition does not require any working gas and due to the high deposition rate, the deposited films have been demonstrated to have low incorporated hydrogen content; almost four order of magnitude less than bulk niobium. However, macro particles in the µm range

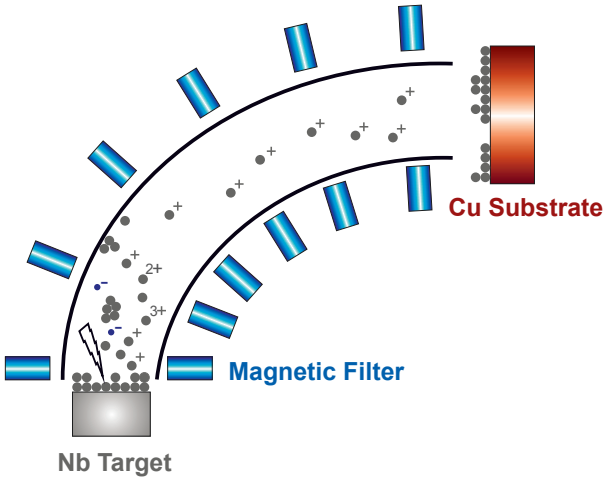

Figure 2.12.: Principle of the cathodic arc deposition: A high current arc vaporises cathode material in UHV. Static magnetic fields and substrate biasing is used to filter macro particles and to extract ions towards the substrate.

deteriorate the film quality as they do not have any surface mobility or even bulk diffusion. Moreover, the promote shadowing. Filtering macro particles is possible but reduces the deposition rate significantly.

Niobium films deposited on sapphire and MgO yield repeatedly very high RRR values up to 680, but the films suffer still from localized bad adhesion which inhibits an accurate evaluation of the RF performance [82, 83].

3. Theoretical Limitations

The quality factor Q of a cavity is given by the geometry and the reciprocal of the surface resistance R_S:

$$Q = \frac{G}{R_\mathrm{S}}, \tag{3.1}$$

where the geometry factor G only depends on the RF field distribution in the cavity and hence only on the geometry of the structure. The surface resistance depends on temperature, frequency, RF field, material parameters and ambient conditions and defines the SRF performance of a cavity. Some of these dependencies are well described by theory; the frequency and temperature dependence at low RF field are described by the BCS surface resistance while other contributions are described empirically.

A typical performance curve of a bulk niobium cavity is shown in Figure 3.1, with three regimes defined: The first is the low field Q-increase, the second the medium field Q-slope and the third the high field Q-drop. All three are still not fully understood and subject to ongoing research.

The black line in Figure 3.1 represents the ideal Q curve within the Mattis-Bardeen theory which describes the BCS losses in the zero field approximation. An RF field dependence is here only given by the magnetic field dependence of the superconducting energy gap Δ_0 [84]:

$$\Delta_0 (B) = \Delta_0 (0) \sqrt{1 - \left(\frac{B}{B_\mathrm{c}}\right)^2} \tag{3.2}$$

This ideal Q curve was recently questioned by measurements on nitrogen doped bulk niobium cavities which show an extended Q increase with fields up to high fields in the order 100 mT [16].

The difference between the predictions and the measurements is described by the residual surface resistance so that the overall surface resistance is described as the sum of two contributions: the temperature (T) dependent (low RF field) BCS resistance R_{BCS} which will be subject to the next section, and the temperature independent residual resistance, R_{res}, which will be addressed in Section 3.2. It summarizes all non-BCS losses and therefore might depend on RF field, B_{RF}, and frequency f_0:

$$R_\mathrm{S} = R_\mathrm{BCS} (T, f_0) + R_\mathrm{res} (B_\mathrm{RF}, f_0) \tag{3.3}$$

The maximum accelerating gradient (for a given geometry factor) is given by the field where the Meissner state of the superconductor breaks down and the cavity becomes either highly dissipative due to flux penetration, or quenches. The so-called superheating field is subject to Section 3.3.

Finally, the material aspects of multipacting are introduced in the final section of this chapter. Although multipacting is well understood and considered mastered for niobium, the secondary electron yield as a material property must be addressed when considering new materials for SRF application.

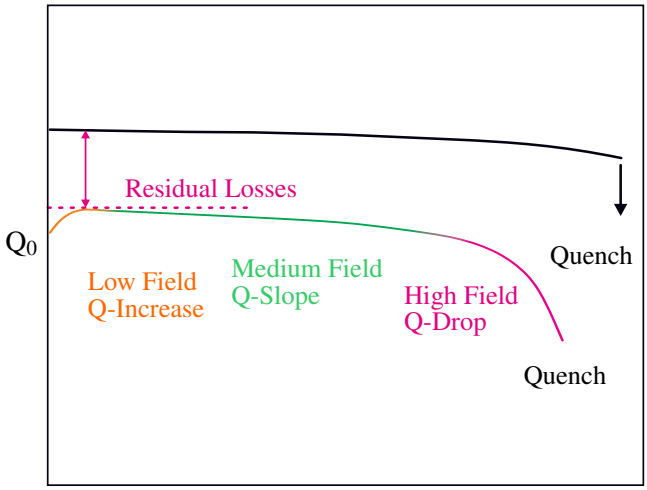

Figure 3.1.: Typical performance curve for bulk niobium.

3.1. BCS Resistance

Based on the BCS theory Mattis and Bardeen [85, 86] as well as Abrikosov, Gork'lov and Khalatnikov [87] developed a theoretical description of the surface impedance of normal and superconductors in the low field approximation. The Mattis-Bardeen theory describes the surface impedance for superconductors as a function of temperature and material parameters such as penetration depth, coherence length, mean free path and superconducting energy gap but is limited to frequencies well below 100 GHz and small magnetic fields ($B \ll B_{c1}$) [86]. Below $T_c/2$, the BCS surface resistance can be approximated by:

$$R_{\mathrm{BCS}} = \frac{A_{\mathrm{BCS}}}{T} e^{-\Delta/k_B T} \tag{3.4}$$

The factor A_{BCS} depends on frequency ($\omega = 2\pi f_0$), the normal conductivity $\sigma = \sigma_0 \cdot RRR$, with the electrical conductivity at room temperature σ_0 and the residual resistance ratio RRR, and the penetration depth λ_{eff}:

$$A_{\mathrm{BCS}} \sim \mu_0^2 \omega^2 \sigma_0 RRR \cdot \lambda_{\mathrm{eff}}^n \tag{3.5}$$

Depending on if the superconductor is in the clean or dirty limit, n is 4 or 3 so that A_{BCS} scales with:

$$A_{\mathrm{BCS}} \sim \lambda_{\mathrm{eff}}^4 \text{ in the clean limit, i.e. where } \ell \gg \xi_0 \tag{3.6}$$

$$A_{\mathrm{BCS}} \sim \lambda_{\mathrm{eff}}^3 \text{ in the dirty limit, i.e. where } \ell \ll \xi_0. \tag{3.7}$$

A. Gurevich recently proposed to calculate the surface resistance as function of a strong RF field within the non-equilibrium BCS theory [88]. The calculations are restricted to dirty type II superconductors ($\lambda_{\mathrm{eff}} \gg \xi_{\mathrm{eff}}$) at low temperature. For frequencies far away from the pair breaking limit the RF field oscillates slowly across the coherence length ξ_{eff} so that the screening current has to be treated locally and the density of electron states becomes time dependent. If the RF period is shorter than the recombination time of Cooper pairs and shorter than the scattering time for electrons off phonons, the normal electrons absorb RF power but cannot transfer energy to the lattice. In this case the normal elec-

trons become overheated with respect to the lattice. As a result, the surface resistance decreases with RF field strength. Comparison with measurements on titanium doped niobium cavities at 1.5 GHz and 2 K yields good agreement and a one parameter fit yields an electron overheating of about 170 mK [88].

3.2. Residual Resistance

As introduced in Section 3.1 the residual resistance is a collection of all effects which are not described by the BCS theory. It is assumed to be independent of temperature but might depend on RF field, frequency and other quantities. Two effects are of particular interest of this thesis: RF field dependent losses in niobium films as they are the dominant limitation of the technology and losses due trapped magnetic flux which is a main limitation for bulk niobium, yet negligible for Nb/Cu films. In addition, niobium hydrides which in their severest form cause the so-called Q-disease in bulk niobium are briefly introduced. Niobium hydrides along with niobium oxides are often discussed as a root cause for unexplained losses.

3.2.1. RF Field Dependence for Niobium Films

While bulk niobium cavities typically show surface resistance curves that increase linearly or quadratically with RF field, the surface resistance increase of niobium film cavities is much stronger and often exponential in nature. Different loss mechanisms have been proposed as potential explanation describing frequency and the RF field dependencies. Most models have in common that they attribute the losses to the smaller grain size in niobium films. Typical grain sizes of sputtered Nb/Cu films are in the order of 100 nm compared to 50 µm for bulk niobium sheet.

Intergrain Losses

Based on calculations of the surface impedance of high T_c superconductors by T. Hylton *et al.* [89] B. Bonin and H. Safa proposed that grain boundaries may be treated as Josephson junctions and present weak superconducting links in the niobium [90]. Calculations predict a quadratic dependence on frequency for low RF fields which agrees well with experiments in bulk niobium [91] as well as Nb/Cu films [92]. However, predictions of these models for the field dependence of the surface impedance does not match the experimental data.

J. Halbritter focussed on the role of oxidation of grain boundaries, the external surface and the Nb-Cu interface [93]: Oxidised grain boundaries act as weak or strong links between grains, and are again treated as Josephson junctions. Additional losses may then arise from leakage current through the lossy grain boundary (*weak link model*) or inelastic scattering on localized states in the niobium oxides at the oxide-metal interfaces. Like Hylton and Bonin/Safa, this model predicts a f_0^2 dependence. Moreover, weak links allow early flux penetration which causes hysteresis losses scaling linearly in frequency. The weak link model as well as hysteresis losses predict a dependence on the RF field of $\sim B^2$. For all models the grain size and the thickness of the grain boundaries are crucial as they influence the compression of grain boundaries and their extend of oxidation. Bigger grains result in a lower grain boundary density with less compressed boundaries which leads to a thicker inter-grain oxide layer and therefore a thicker tunneling barrier. As a result, the grain boundary resistance of big grain is larger

than for small grains. Nevertheless, considering the whole cavity surface, the larger grain boundary resistance will be compensated with the lower total number of grain boundaries.

For strongly oxidised surfaces and crack corrosion, J. Halbritter introduces the interface tunnel exchange (ITE) model which describes dielectric losses due to tunneling of electrons between insulating (Nb_2O_5) and superconducting (Nb) areas [94]. These dielectric losses are characterized by an onset field, followed by a concave increase of surface resistance and scale linearly in frequency. Experimental evidence was found in strongly oxidized Nb/Cu films [95, 96].

Thermal Boundary Resistance Model

The most recent model discussing the Q-Slope in niobium films is offered by V. Palmieri and R. Vaglio [97]: The authors argue that the decline in Q is a result of local poor adhesion between the niobium film and the copper substrate resulting in a high thermal contact resistance.

Considering a perfectly connected Nb-Cu system the thermal contact resistance $R_{Nb/Cu}$ between the two metals is negligible compared to the Kapitza resistance at the copper-helium interface R_K: The first is estimated to be $0.3\,\mathrm{cm^2K/W}$ while the latter typically is the same order as the Kapitza resistance of the (bulk) niobium-helium interface – several $\mathrm{cm^2}$ K/W.

For a given RF field B_RF the dissipated power P_{diss} on any cavity surface is

$$P_\mathrm{diss} = \frac{1}{2\mu_0^2} R_\mathrm{S}(T)\, B_\mathrm{RF}^2 \tag{3.8}$$

with R_S being the total surface resistance and μ_0 the vacuum permeability. The corresponding temperature difference between the RF surface and the heat sink, i.e. the helium bath, depends on the thermal boundary resistance $R_B = R_\mathrm{Nb/Cu} + R_\mathrm{K}$ and is $\Delta T = P_\mathrm{diss} \cdot R_\mathrm{B}$.

If the niobium film is locally detached the cooling power is diminished, a microscopic hot spot with a high R_B is created. The surface resistance then increases exponentially due to the temperature dependence of the BCS resistance and can lead to a local thermal run away and drive the detached spot into the normal conducting state with a constant (normal) surface resistance. Below $T_\mathrm{c}/2$ the increase of surface resistance is described as

$$R_\mathrm{S} = \frac{A_\mathrm{BCS}}{T_0 + \Delta T} \exp\left[-\frac{\Delta_0}{k_\mathrm{B}(T_0 + \Delta T)}\right] + R_\mathrm{res} \tag{3.9}$$

where T_0 is the helium bath temperature, k_B the Boltzmann constant and all other parameters as defined previously.

The local temperature increase ΔT is then

$$\Delta T = \frac{1}{2\mu_0^2} R_\mathrm{B} R_\mathrm{S}(T)\, B_\mathrm{RF}^2. \tag{3.10}$$

Based on the assumption that the thermal boundary resistance between niobium and copper, $R_\mathrm{Nb/Cu}$, is not constant over the whole RF surface, Palmieri and Vaglio introduce a statistical distribution function $f(R_\mathrm{Nb/Cu})$ that represents the probability of finding a given $R_\mathrm{Nb/Cu}$ value on the RF surface. This distribution function must comply with the following two conditions:

$$\int_0^\infty f\left(R_{\mathrm{Nb/Cu}}\right) \mathrm{d}R_{\mathrm{Nb/Cu}} = 1 \tag{3.11}$$

$$\int_0^\infty R_{\mathrm{Nb/Cu}} f\left(R_{\mathrm{Nb/Cu}}\right) \mathrm{d}R_{\mathrm{Nb/Cu}} = \overline{R_{\mathrm{Nb/Cu}}} \tag{3.12}$$

where $\overline{R_{\mathrm{Nb/Cu}}}$ is the average thermal boundary resistance.

The average surface resistance which is accessible through measurement is accordingly

$$\overline{R_{\mathrm{S}}\left(T_0, B_{\mathrm{RF}}\right)} = \int_0^\infty R_{\mathrm{S}}\left(T_0, B_{\mathrm{RF}}, R_{\mathrm{B}}\right) \cdot f\left(R_{\mathrm{Nb/Cu}}\right) \mathrm{d}R_{\mathrm{Nb/Cu}}. \tag{3.13}$$

From measuring $\overline{R_{\mathrm{S}}\left(T_0, B_{\mathrm{RF}}\right)}$ the distribution function $f\left(R_{\mathrm{Nb/Cu}}\right)$ can be derived in an iterative way: The Equation 3.13 is approximated with

$$\overline{R_{\mathrm{S}}\left(B_{\mathrm{RF}}\right)} = \sum_{i=1}^{n} R_{\mathrm{S}}\left(B_{\mathrm{i}}, R_{\mathrm{B,i}}\right) f\left(R_{\mathrm{B,i}}\right) \Delta R_{\mathrm{B,i}} = \sum_{i=1}^{n} R_{\mathrm{S}}\left(B_{\mathrm{i}}, R_{\mathrm{B,i}}\right) \cdot P_{\mathrm{i}} \tag{3.14}$$

for $i = 1...n$ data points and with the weights $P_{\mathrm{i}} = f\left(R_{\mathrm{B,i}}\right) \Delta R_{\mathrm{B,i}}$ and $\Delta R_{\mathrm{B,i+1}} = R_{\mathrm{B,i+1}} - R_{\mathrm{B,i}}$.

In practice, two sets of measurement are usually performed: $R_{\mathrm{S}}(T)$ at a fixed, typically low, RF field and $R_{\mathrm{S}}\left(B_{\mathrm{RF}}\right)$ at a fixed temperature(s). The $R_{\mathrm{S}}(T)$ data is fitted and the resulting fit function is introduced into Equation 3.10. The local temperature increase and the resulting surface resistance (Equation 3.9) are then calculated for different R_{B} values. For each R_{B} value a quench field is obtained that leads to a thermal runaway, i.e. temperature increase above 9.3 K. These (R_{B}, B_{quench}) value pairs are fitted as $R_{\mathrm{B}} \sim B_{\mathrm{quench}}^{-2}$. Now a corresponding R_{B} value is calculated for each data point of the $R_{\mathrm{S}}\left(B_{\mathrm{RF}}\right)$ measurement, which means that $B_{\mathrm{i}} \coloneqq B_{\mathrm{quench}}$ in Equation 3.14.

Solving Equation 3.14 for all P_{i} yields

$$P_{\mathrm{i}} = \frac{R_{\mathrm{S}}\left(B_{\mathrm{i+1}}\right) - R_{\mathrm{S}}\left(B_{\mathrm{i}}\right)}{R_{\mathrm{N}}} \qquad \text{for} \qquad 1 \leq i \leq n-1 \tag{3.15}$$

with the normal conducting electrical resistance R_{N}, and

$$P_{\mathrm{n}} = 1 - \sum_{i=1}^{n-1} P_{\mathrm{i}}. \tag{3.16}$$

Finally, the distribution function can be calculated via $f\left(R_{\mathrm{B,i}}\right) = P_{\mathrm{i}}/\Delta R_{\mathrm{B,i}}$. In addition, integrating (resp. summing) over all the distribution function values allows estimating the fraction of surface that is not well attached to the substrate. Typical values for sputtered films range between 0.03 % to 0.5 % of the surface area [97].

There are two main weakness of this model: First, it allows heat flow only normal to the surface and not lateral. It remains unclear if this is a reasonable assumption, considering that the thermal conductivity of copper is much higher than the thermal conductivity of low RRR niobium. Secondly, the derivation of a distribution function is not a fit and a solution can be obtained for any data set independently of a physical meaning.

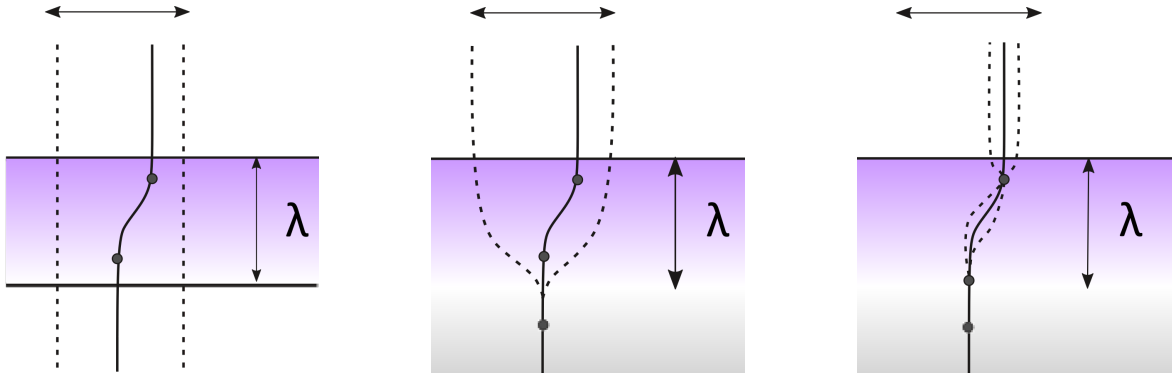

(a) (b) (c)

Figure 3.2.: Flux line motion under the influence of an RF field. The solid line represents a single flux line trapped by two pinning centres. The dashed lines indicate the range of motion for the flux line assuming (a) a film thinner than the penetration depth and with $f_0/f_p \gg 1$, (b) a thick superconductor with $f_0/f_p \gg 1$, (c) a thick superconductor with $f_0/f_p \ll 1$.

3.2.2. Trapped Magnetic Flux

Trapped magnetic flux is known to be a significant contribution to the residual resistance in bulk niobium. When the material becomes superconducting, any ambient magnetic field should be expelled from the the bulk according to the Meissner effect. Imperfections such as grain boundaries and lattice defects, impurities and oxides and hydrides have a pinning potential and inhibit the expulsion of the magnetic field. Each magnetic flux line has an associated flux vortex with a normal conducting core with the coherence length as the radius. Under the influence of RF, the vortices might oscillate causing dissipation.

If flux lines are depinned from their pinning centre, they will be coherently dragged through the material following the driving force. The frequency at which 50 % of the pinned vortices are depinned, is defined as the depinning frequency f_p.

To study pinning effects samples thinner than the penetration depth λ_{eff} are used so that the sample is fully penetrated by the RF field and there are no field free regions. In this case the depinning frequency can be derived from power dissipation when vortices are moved freely through the material which is depicted in Figure 3.2a. This case would even allow to eliminate entirely trapped flux from the sample due to the fact that all pinning centers are exposed to the RF field.

For superconducting cavities the RF does not fully penetrate the superconducting material, yet, the whole superconducting layer has to be considered: Figure 3.2b depicts the situation of trapped flux exposed to an RF field well above the depinning frequency. The vortices are depinned from their pinning centres in the surface layer which is penetrated by the RF field. However, if the vortices are pinned deep in the field free bulk, they cannot be driven out of the superconductor entirely. The loose end within the penetration depth will now oscillate under the RF and dissipate.

If the RF frequency is well below the depinning frequency, the vortex remains pinned in the RF layer and can only move in-between pinning centres as indicated in Figure 3.2c. This is expected to lead to only small dissipation.

For a qualitatively better understanding of the depinning frequency and the associated losses, the

theoretical work of Gittleman and Rosenblum and other authors is summarized in the following: In an ideal superconductor, i.e. a superconductor without pinning, only the Lorentz force and the frictional force have to be considered for describing the motion of a flux line

$$\frac{j_\mathrm{T}\Phi_0}{c} = \eta\dot{x} \tag{3.17}$$

where the transport current j_T, the magnetic flux quantum Φ_0 and the speed of light c describe the Lorentz force and the flux flow viscosity η and the speed of a flux line $\dot{x}$ describe the frictional force.

Using Ohm's law, $j = E/\rho$, with the electrical resistivity ρ and the electric field due to the moving vortices, $E = B \cdot \dot{x}/c$, the formula can be further developed: ρ is identified as a flux flow resistivity

$$\rho_\mathrm{f} = \rho_\mathrm{n} \cdot \frac{B}{B_\mathrm{c2}} \tag{3.18}$$

with the electrical resistivity of the normal conductor at low temperature ρ_n and the fraction of normal conducting material given by B/B_{c2} where B_{c2} is the upper critical field in a type II superconductor [98].

The flux flow viscosity is accordingly:

$$\eta = \frac{\Phi_0 B_\mathrm{c2}}{c^2\rho_\mathrm{n}}. \tag{3.19}$$

If pinning occurs, the motion of a flux line can be treated as a driven oscillator, accounting for the Lorentz force, the frictional force and the pinning force [99, 100, 101]:

$$m\ddot{x} + \eta\dot{x} + kx = \frac{j_\mathrm{T}\Phi_0}{c} \tag{3.20}$$

Here m is the effective mass of the vortex per unit length. The RF period ($> 10^{-8}$ s) is much larger than the relaxation time of a vortex $\tau \sim m$ which was estimated by H. Suhl to be in the order of 10^{-12} s [100, 102] so that this contribution can be neglected and Equation 3.20 reduces to a linear differential equation of first order:

$$\eta\dot{x} + kx = \frac{j_\mathrm{T}\Phi_0}{c}. \tag{3.21}$$

k accounts for the pinning force and depends on the size, geometry and type of the pinning centre. It also describes if the pinning centre is interacting with a single flux line or the whole flux line lattice.

The depinning frequency f_p is a solution to the differential equation 3.21 and given by the ratio of pinning constant and flux flow viscosity [103]:

$$f_\mathrm{p} = \frac{1}{2\pi}\frac{k}{\eta}. \tag{3.22}$$

If the surface currents induced by the RF are significantly smaller than the depairing current[1] and if the thickness of the sample is less than the penetration depth, the impedance Z (in the mixed state) as function of frequency f_0 can be calculated and can be used to experimentally derive the depinning frequency f_p [99]:

[1] current where superconductivity breaks down.

$$Z = \frac{R_\mathrm{n} H}{H_\mathrm{c2}} \frac{f_0}{f_0^2 + f_\mathrm{p}^2} \left(f_0 + i f_\mathrm{p} \right) \tag{3.23}$$

In general, the (surface) impedance Z_S is described as

$$Z_\mathrm{S} = R_\mathrm{S} + i X_\mathrm{s} \tag{3.24}$$

with the surface resistance R_S and the surface reactance Xs. The real part of Equation 3.23 can then be identified with the additional surface resistance due to depinned trapped flux.

Furthermore, Larkin and Ovchinnikov [104] estimate the pinning force F_p of a grain boundary acting on a single flux line parallel to the grain boundary to

$$F_\mathrm{p} = \mathcal{N} g_1 \Delta^2 \xi p \tag{3.25}$$

with the density of electron states $\mathcal{N}$, the electron-phonon interaction g_1 and the thickness of the grain boundary p. It is assumed that $k \sim F_\mathrm{p}$ and that the normal electrical resistivity is inversely proportional to the purity of the material, i.e. $\rho_\mathrm{n} \sim 1/RRR$. It follows that the depinning frequency f_p increases with the size of the pinning centre p and with decreasing purity, following

$$f_\mathrm{p} \sim \frac{p}{RRR} \tag{3.26}$$

if all other parameters stay fixed.

Based on Equation 3.23 the depinning efficiency ε_pin can be defined, following the same dependence on frequency and depinning frequency and ranging from 0 % for complete pinning and 100 % for complete depinning:

$$\varepsilon_\mathrm{pin} = \frac{f_0^2}{f_0^2 + f_\mathrm{p}^2} = \frac{\left(f_0 / f_\mathrm{p} \right)^2}{\left(f_0 / f_\mathrm{p} \right)^2 + 1} \tag{3.27}$$

As long as the depinning frequency is unknown, only qualitative statements can be made for the sensitivity of niobium cavities to trapped flux.

Figure 3.3 shows the depinning efficiency as a function of the ratio between operating frequency f_0 and depinning frequency f_p.

Two regimes can be identified: Bulk niobium cavities have a high RRR yielding a low depinning frequency but are operated at rather high frequencies. Therefore it is suggested that $f_0/f_\mathrm{p} \gg 1$ and all trapped vortices are depinned. In contrast, niobium films have comparatively low RRR , i.e. high f_p, but are operated at low frequencies. The trapped vortices may stay pinned and contribute only slightly to the dissipation. Hence their performance is on the opposite side of the slope which agrees with the experimental experience that niobium films are significantly less sensitive to trapped flux as bulk niobium. High RRR films at high frequency or bulk niobium with reduced RRR at low frequency might move towards the transition from one regime to the other.

From bulk Nb cavity measurements, an empirical formula was derived to estimate the additional residual resistance R_TF due to trapped magnetic field B_TF with a frequency scaling according to the

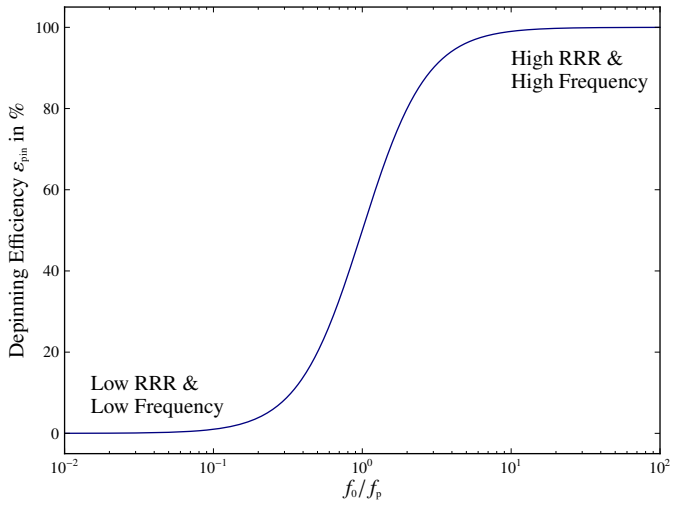

Figure 3.3.: Depinning efficiency as function of operating frequency/depinning frequency, f_0/f_p.

normal skin effect:

$$R_{\mathrm{TF}} = S_{\mathrm{TF}} \cdot B_{\mathrm{TF}} \sqrt{\frac{f_0/1.5\,\mathrm{GHz}}{RRR/300}} \tag{3.28}$$

The trapped flux sensitivity S_{TF} describes how much additional surface resistance must be expected per trapped magnetic field unit. It is derived experimentally to be 3.6 nΩ/μT for RRR 300 bulk niobium at 1.5 GHz [105], but the amount of trapped field depends also on the treatment history of the material. Moreover, the ratio between trapped magnetic field B_{TF} and external field B_{ext}, i.e. the trapping efficiency ε_{TF}, was found to not depend on the ambient field strength [19].

Trapping efficiencies between 40 % to 100 % were found and $B_{\mathrm{TF}} = \varepsilon_{\mathrm{TF}} B_{\mathrm{ext}}$ is valid for external fields up to 300 μT. For fine grain bulk niobium after 800° baking and light BCP which is the TESLA standard material, a flux trapping efficiency of about 80 % was found. Correspondingly, a surface resistance increase of more than 140 nΩ have to be expected for a TESLA cavity if the earth magnetic field[2] was not shielded. As a consequence, magnetic shielding as low as 0.5 μT is common for today's bulk niobium cavities.

Only few data sets are available on flux trapping in niobium coatings. A study on 1.5 GHz cavities shows a flux trapping efficiency close to 100 %, yet additional surface resistances due to trapped flux well below 0.1 nΩ/μT [13]. Measurements on other niobium-on-copper coated SRF cavities, i.e. other geometries and/or frequencies (down to 100 MHz), show similar trapped flux losses and suggest that Equation 3.28 does not apply to Nb/Cu films.

Due to the fact that the measured values for trapped flux losses across the frequency range of 100 MHz to 1.5 GHz are all of the same order of magnitude and very small, no magnetic shielding is used for in the cryomodules of the respective accelerators.

[2] Based on an earth magnetic field of 49 μT in Meyrin, Switzerland [106]

3.2.3. Niobium Hydrides

Hydrogen chemically bonds to niobium and forms niobium hydrides during cool down, in particular in the temperature range between 60 K to 150 K [35]. In this temperature range interstitial hydrogen can still move through the lattice but with decreasing speed as the temperature drops. The hydrogen eventually segregates at low energy sites and forms niobium hydrides as the temperature further decreases and the mobility of the hydrogen atoms ceases. For higher (> 150 K) or lower (< 60 K) temperatures, the required H mobility is too high resp. too low to form hydrides.

A high hydrogen concentration in the niobium can result in the so-called *Q disease*, a very strong drop in Q starting at low RF fields due to significant niobium hydride formation in the RF surface due to a too slow cool down. The Q disease is usually reversible and can often be cured by warming up to room temperature and cooling down below 60 K quickly again. It is also common practice to park a cavity (after the cold testing) at 100 K for several hours in order to determine if the cavity is susceptible for Q disease.

Any chemical treatment risks loading the material with hydrogen as the oxide layer which serves as a diffusion barrier is dissolved. Although H is very mobile in Nb, it accumulates very close to the surface. This might be due to the fact that lattice features attract hydrogen, and the surface can be considered a major *feature* [107]. But even in a Q disease free cavity, Nb hydrides are expected to contribute to the residual resistance as they are only weakly superconducting. It has been shown that mild baking suppresses the formation of Nb hydrides [108].

3.3. Superheating Field

The accelerating gradient of a cavity is proportional to the surface magnetic field, so that the maximum gradient is given by the maximum sustainable RF magnetic field without loss of superconductivity. As previously discussed in Section 2.1.1, the ratio between accelerating gradient and peak magnetic field is given by the geometry of the cavity. Since the surface magnetic field is the fundamental variable for superconductivity, the cavity geometry will not be under discussion until an estimate for the maximum field can be made and translated into an accelerating gradient for different $E_{\mathrm{acc}}/H_{\mathrm{peak}}$ ratios.

The Meissner state is limited by the critical field (for type I superconductors) respectively by the lower critical field (for type II superconductors). Without any perturbation, the Meissner state can persist in a metastable state up to higher fields. This state is referred to as the superheated state with a *superheating field* as ultimate limit for the Meissner state. The following section gives a brief overview over the underlying theory before calculations of the superheating field can be presented. A fully derivation of the superconducting theories can be found in Reference [109] and are also summarized in Reference [92] .

3.3.1. Ginsburg-Landau Theory

To understand the superheating field a description of superconductivity in terms of Ginsburg-Landau theory is required. The Ginsburg-Landau theory is a macroscopic phenomenological theory which successfully describes situations where spatial inhomogeneity has to be taken into account. Ginsburg and Landau introduced a pseudo-wave-function ψ as a complex order parameter which is small and varies

slowly in space. Its squared norm $|\psi|^2$ represents the local density of superconducting charge carriers and Gibbs free energy density g can be expanded in a series of even powers of $|\psi|$. For temperatures close to the critical temperature and for slow varying vector potential $\mathbf{A}$, the free energy density reads

$$g = g_{\mathrm{n0}} + \alpha |\psi|^2 + \frac{\beta}{2} |\psi|^4 + \frac{1}{2m^*} \left| \left(\frac{\hbar}{i} \nabla - e^* \mathbf{A} \right) \psi \right|^2 + \frac{\mu_0 H^2}{2} \tag{3.29}$$

where $g_{\mathrm{n0}} + \mu_0 H^2/2$ equals the free energy in the normal state. m^* and e^* represent the mass and the charge of the superconducting charge carriers and $\hbar$ is Plancks constant divided by 2π. Within the BCS theory, these superconducting charge carriers will be identified by Cooper pairs [110], with twice the electron mass and twice the electron charge so that $m^* = 2m_{\mathrm{e}}$ and $e^* = 2e$.

Considering the fourth contribution in Equation 3.29 to be zero, i.e. if no magnetic fields and no gradients are present, it can be found that

$$|\psi|^2 = |\psi_\infty|^2 \equiv -\frac{\alpha}{\beta} \tag{3.30}$$

which yields the definition of the (theromdynamic) critical field H_{c}:

$$g_{\mathrm{s}} - g_{\mathrm{n}} = -\frac{\alpha^2}{2\beta} = -\frac{\mu_0 H_{\mathrm{c}}^2}{2}. \tag{3.31}$$

$|\psi_\infty|^2$, $\alpha(T)$ and $\beta(T)$ only depend on the charge carrier mass and charge. The thermodynamic critical field it linked to a characteristic length λ which can be identified with Londons penetration depth for an ideal superconductor. It represents the length scale on which the ambient magnetic field penetrates the surface of the superconductor. Minimization of the free energy of a system leads to a set of differential equations which allow the description of the superconducting state. Solving the equations for zero magnetic field, a second characteristic length, the coherence length ξ, can be deduced. It describes the interaction distance between two electrons in a Cooper pair bound state. Furthermore, the Ginsburg-Landau parameter is defined as

$$\kappa = \lambda / \xi$$

which separates two classes of superconductors: Type I for $\kappa \leq 1/\sqrt{2}$ and type II where $\kappa \geq 1/\sqrt{2}$. For type II superconductors it will be energetically favourable to change into a mixed state above a lower critical field H_{c1} where the ambient magnetic field penetrates the material in distinct flux lines. Superconductivity eventually breaks down at an upper critical field H_{c2}.

As will be seen in the following section, the superheating field usually depends on the Ginsburg-Landau parameter which in turn is a function of temperature and mean free path. From the Ginsburg-Landau differential equations follows the temperature dependence of the coherence length and the penetration depth:

$$\xi(T) = \frac{\Phi_0}{2\sqrt{2}\pi H_{\mathrm{c}}(T)\, \lambda_{\mathrm{eff}}(T)} \tag{3.32}$$

Here, Φ_0 is the flux quantum, defined by the BCS theory as:

$$\Phi_0 = \sqrt{\frac{2}{3}} \pi^2 \xi_0 \lambda_{\mathrm{L}} H_{\mathrm{c}}(0) \tag{3.33}$$

ξ_0 and λ_L are material parameters, i.e. the coherence length and the penetration depth at 0 K and for infinite mean free path ℓ. Substituting Φ_0 in Equation 3.32 yields

$$\xi(T) = \frac{\pi\xi_0}{2\sqrt{3}} \frac{H_c(0)}{H_c(T)} \frac{\lambda_L}{\lambda_{eff}(T)}, \tag{3.34}$$

and taking into account the temperature dependence of the critical field $\sim \left(1 - (T/T_c)^2\right)$, the Ginsburg-Landau parameter can be expressed as a function of temperature and effective penetration depth λ_{eff}, which includes already the effect of a finite mean free path:

$$\kappa(T) = \frac{\lambda_{eff}(T)}{\xi(T)} = \frac{2\sqrt{3}}{\pi} \frac{\lambda_{eff}(T)^2}{\xi_0 \lambda_L} \left(1 - \left(\frac{T}{T_c}\right)^2\right) \tag{3.35}$$

The effective penetration depth can be replaced with the Gorter-Casimir relation:

$$\lambda_{eff}(T, \ell) = \frac{\lambda(0, \ell)}{\sqrt{1 - \left(\frac{T}{T_c}\right)^4}} \tag{3.36}$$

This relation is an empirical expression and is known to fit very well experimental data. The penetration depth at 0 K but for finite mean free path ℓ is given by Pippard [111]

$$\lambda(0, \ell) = \lambda_L \sqrt{1 + \frac{\pi\xi_0}{2\ell}} \tag{3.37}$$

and describes less effective shielding for finite (short) mean free path.

Finally, an expression for the Ginsburg-Landau parameter as function of the fundamental parameters ξ_0 and λ_L, mean free path and temperature is found:

$$\kappa(T, \ell) = \frac{2\sqrt{3}}{\pi} \frac{\lambda_L \left(1 + \frac{\pi\xi_0}{2\ell}\right)}{\xi_0 \left(1 + \left(\frac{T}{T_c}\right)^2\right)} \tag{3.38}$$

The literature values for niobium are

$$\lambda_L = 32\,\text{nm} \tag{3.39}$$

$$\xi_0 = 39\,\text{nm}. \tag{3.40}$$

Further if the empirical relation for the mean free path [112]

$$\ell = 2.7 \cdot RRR \tag{3.41}$$

is taken into account, the resulting Ginsburg-Landau parameter is

$$\kappa \approx 1 \qquad \text{for typical bulk niobium with RRR 300 and} \tag{3.42}$$

$$2 \leq \kappa \leq 3 \qquad \text{for niobium films with RRR 5 to 20.} \tag{3.43}$$

Therefore, the commonly used approximations for superconductors, i.e. $\kappa >> 1$ and $\kappa << 1$ do not

apply for niobium.

3.3.2. The Critical Fields

The most fundamental (critical) field in superconductivity is defined as the magnetic field strength at which the energy needed to expel the magnetic field from the bulk of the superconductor compensates the energy gain due to electrons condensing into Cooper pairs. It is therefore referred to as the *thermodynamic* critical field H_c [113]:

$$\mu_0 H_c = \frac{\Phi_0}{2\sqrt{2}\pi\lambda\xi} \tag{3.44}$$

For a type I superconductor H_c separates (thermodynamically) the Meissner state from the normal conducting state. For type II superconductors, it has only a virtual meaning, as the transition from Meissner to mixed state and from mixed state to normal conducting state are described by the *lower* critical field H_{c1} and the *upper* critical field H_{c2}. They are usually defined in the high κ approximation [113, 114]:

$$\mu_0 H_{c1} = \frac{\Phi_0 \ln\kappa}{4\pi\lambda^2} \tag{3.45}$$

$$\mu_0 H_{c2} = \frac{\Phi_0}{2\pi\xi^2}. \tag{3.46}$$

While H_{c2} also holds for small κ, H_{c1} becomes zero (for $\kappa = 1$) or negative (for $\kappa < 1$). Abrikosov formulates the lower critical field for $\kappa \gg 1$ as [115]

$$H_{c1,\,\kappa\gg 1} = \frac{1}{2\kappa}\cdot(\ln\kappa + 0.081)\,. \tag{3.47}$$

The additional constant of 0.08 is negligible for sufficiently high values of κ and is therefore often dropped in text books. Later numerical calculations done by Hu correct the constant to 0.497 [116] but keep the restrictions to high values of κ. Harden and Arp [117] calculated H_{c1} by solving numerically Abrikosovs formulation of the Ginsburg-Landau equations for eight κ values ranging from 0.3 to 50. Their results are plotted in Figure 3.4 and fitted for the values up to $\kappa = 20$ with the following function

$$H_{c1,\kappa\leq 20} = 0.817\cdot\kappa^{-0.615} H_c \tag{3.48}$$

Figure 3.4 compares also Harden and Arps calculations with the previously mentioned high κ approximations. As can be seen, for high values of κ all curves converge but only Harden and Arps calculations approach H_c at the transition from type II to type I superconductors where $\kappa = 1/\sqrt{2}$.

For this reason, the other models are discarded and all calculations of H_{c1} for small κ type II superconductors will be based on the Harden and Arp calculations respectively Equation 3.48

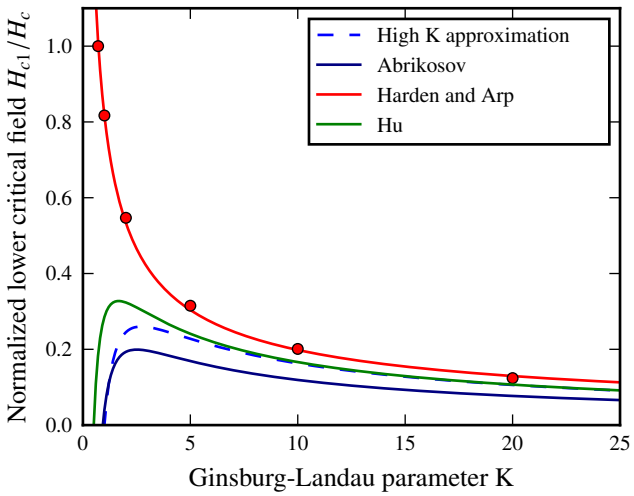

Figure 3.4.: Lower critical field according to different models as function of κ. Only the approximation given by Harden and Arp [117] approaches H_c at the transition to type I superconductors.

3.3.3. The Superheating Field within the Ginsburg-Landau Theory

For high values of the Ginsburg-Landau parameter κ the superheating field was calculated based on the Ginsburg-Landau theory by Galaiko [118]. He finds

$$H_{\mathrm{sh,GL}} = 0.75 H_\mathrm{c} \tag{3.49}$$

for temperatures close to T_c and

$$H_{\mathrm{sh}} = 0.84 H_\mathrm{c} \tag{3.50}$$

for temperatures well below T_c. The latter was supported by recent numerical solutions of the Eilenberger equations [119].

The first calculation of the superheating field for intermediate values of κ was done in 1967 by J. Matrcion and D. Saint-James [120]. The authors solved numerically the one dimensional Ginsburg-Landau equations for a semi-infinite superconductor in the presence of a magnetic field, parallel to the surface. For κ values $\leq 1/\sqrt{2}$ their solution is in good agreement with the approximation derived in Orsay [121] for type I superconductors. From Figure 1 in Reference [120], the superheating field for $\kappa \approx 1$, i.e. high quality bulk Nb, can be read:

$$H_{\mathrm{sh},\kappa\approx 1} = 1.29 \cdot H_\mathrm{c} \tag{3.51}$$

As the superheating field depends on the Ginsburg-Landau parameter, Equation 3.51 can not be used for calculations of the superheating field of niobium with significantly shorter mean free path and corresponding κ values > 1, i.e. Nb films, dirty or doped bulk Nb.

Alternatively, K. Saito found an analytical expression for the superheating field for κ values between $2^{-1/2}$ and 2.5 by fitting the Matricon and Saint-James curve [122]:

$$H_{\mathrm{sh,MSJ}} = 1.291 \kappa^{-0.16008} \cdot H_\mathrm{c} \tag{3.52}$$

It was not until 2011, that Transtrum et al. calculated the superheating field for a large range of κ again by solving the Ginsburg-Landau equations [123]. Like the previous studies, the authors assume a semi-infinite superconductor with an magnetic field parallel to the surface. In contrast to the previous study, they performed a stability study to identify perturbations that lead to the break down of the Meissner state. The superheating field was then defined as the maximum magnetic field for which the second variation of the free energy is positive definite. For the numerical result, analytical approximations were found which describe well the superheating field for κ larger and smaller than a critical value κ_c. This critical value also separates two regimes for the instability and is derived to be

$$\kappa_c = 1.1495. \tag{3.53}$$

For $\kappa < \kappa_c$, instability is caused by one dimensional perturbations which are identified by uniform flux penetration. In this regime, the superheating field is

$$H_{sh,\kappa<\kappa_c} = \sqrt[4]{2}\frac{H_c}{\sqrt{\kappa}}\frac{1 + 4.6825120\kappa + 3.3478315\kappa^2}{1 + 4.0195994\kappa + 1.0005715\kappa^2} \tag{3.54}$$

For $\kappa > \kappa_c$, a two dimensional perturbation causes instability and the superheating field is:

$$H_{sh,\kappa>\kappa_c} = H_c\left(\frac{\sqrt{20}}{6} + 0.3852\sqrt{\frac{2}{\kappa}}\right) \tag{3.55}$$

Unfortunately, neither the corresponding physical mechanism nor the dynamics of vortex penetration are proposed or speculated [124]. Close to κ_c, both approximations deviate, and the numerical solution, which is in agreement with the solution found by Matricon and Saint-James, has to be used.

As introduced in the beginning, the Ginsburg-Landau theory and therefore the calculations of the superheating field is only valid close to the critical temperature. For the behaviour at low temperatures the Eilenberger equations have to be solved. For high κ superconductors this was done by Catelani and Sethna [119] finding an 11 % increase of the superheating field at $0.2T_c$ compared to the Ginsburg-Landau solution. Attempts to calculate the superheating field for small κ type II superconductors at low temperatures indicate that H_{sh} is expected to also increase in the order of 10 % [124].

Putting together the so far presented models for the critical and superheating fields, the phase diagram for the different superconducting states as function of Ginsburg-Landau parameter on the basis of Reference [125] is reproduced in Figure 3.5. In contrast to Yogi et al, the focus is set on the low type II regime. Also, not the numerical solutions for the superheating field but the analytical approximations are used. The dashed line indicates the fit done by K. Saito to describe the superheating field close to $\kappa = 1$ as the analytical approximations of Transtrum et al. are not valid in this range.

From this plot, the main difference between bulk Nb and Nb films become clear: The shorter mean free path, i.e. higher κ of the films results in a suppression of the lower critical field and an increase of the upper critical field. The superheating field decreases only slightly. For clean bulk Nb the mixed state, i.e. field range between superheating field and upper critical field, is comparatively narrow. It can be expected that bulk niobium will almost directly become normal conducting when entering the mixed state due to strong dissipation and thermal break down. The range for the mixed state for a typical Nb film is significantly wider and it remains to be shown if the high thermal conductivity of the

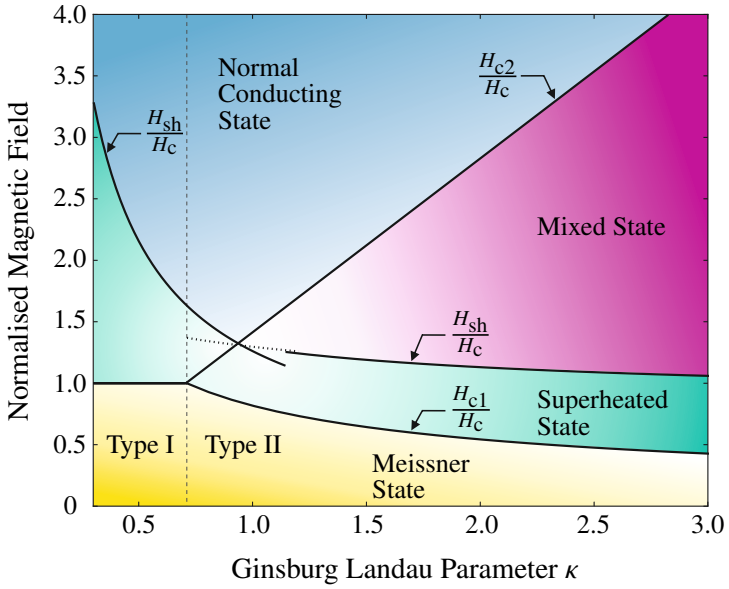

Figure 3.5.: Critical and superheating fields as function of the Ginsburg Landau parameter.

copper substrate is able to sufficiently stablilise a niobium film is the mixed state. Either way, losses are expected to be excessive.

3.3.4. Vortex Line Nucleation

The vortex line nucleation model describes early flux penetration into the superconductor before the superheating field is reached. It considers the surface energy of the superconductor and calculates the energy difference between the condensation energy and the magnetic energy of the vortex [122]. From the Ginsburg-Landau theory, the condensation energy per unit volume is

$$g_{\text{core}} = \pi\xi^2 \frac{H_c^2}{8\pi} \tag{3.56}$$

while the energy provided by the magnetic field is

$$g_{\text{mag}} = \pi\lambda^2 \frac{H^2}{8\pi}. \tag{3.57}$$

The vortices will penetrate the material when the condensation energy cancels the magnetic energy, i.e. $g_{\text{core}} = g_{\text{mag}}$. The vortex line nucleation field is accordingly defined as:

$$H_{\text{vlnm}} = \frac{H_c}{\kappa} \tag{3.58}$$

and can limit the maximum achievable magnetic field, as $H_{\text{vlnm}} < H_{\text{sh}}$.

3.3.5. Predictions for Niobium

Based on the preceding sections, predictions for the lower critical field, the superheating field as well as the vortex line nucleation field shall be made for bulk niobium and niobium films. The Ginsburg-Landau

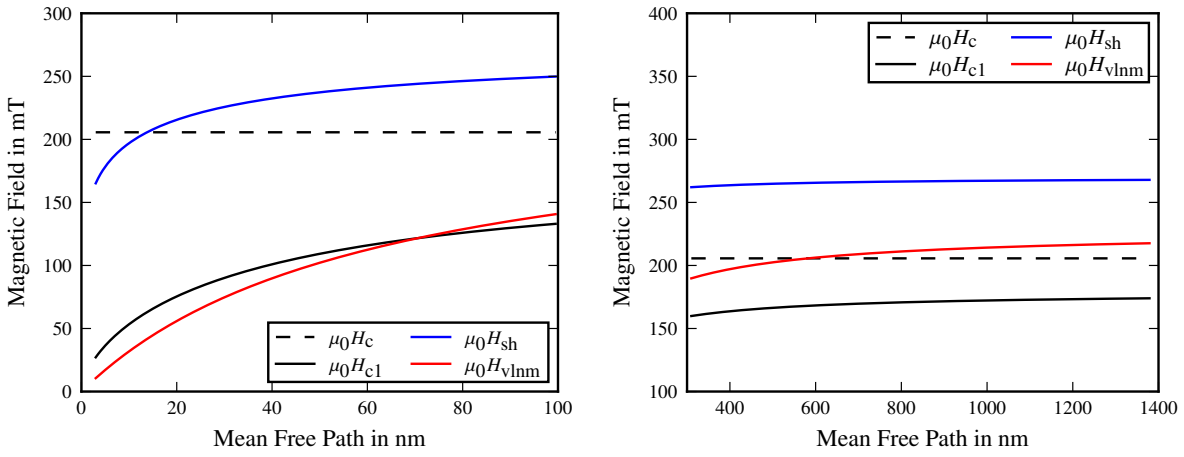

Figure 3.6.: Superheating field at 0 K for (a) niobium films with RRR 2 to 40 and (b) bulk Nb with RRR 200 to 500. See Equation 3.41 for the relation between mean free path and RRR.

parameter will be expressed as function of mean free path using Equation 3.38, while the London penetration depth and the coherence length are taken from literature.

Figure 3.6 shows the predictions for the different magnetic fields as function of mean free path. It can be seen that the superheating field H_{sh} and H_{c1} is approximately constant over the typical bulk niobium range while the vortex line nucleation field starts to decrease below a mean free path of about 500 nm. For the niobium films, all fields decrease significantly for very short mean free path corresponding to RRR values below 7 and hence considered a low quality film as also the BCS resistance is in the dirty limit. A comparison between good quality films (mean free path > 60 nm resp. RRR > 22) and bulk niobium shows that the superheating field of the film is slightly suppressed by about 8 %. This suppression therefore will only limit the application range of niobium films when gradients close to the theoretical limit can be achieved.

3.4. Multipacting

In the late 1970's, multipacting was the main limitation for SRF cavities in terms of accelerating gradient [126, 35]. Multipacting generates electron avalanches and occurs when free electrons from the vacuum or released from the surface are accelerated by the RF field, the emission and the arrival point meet certain symmetry criteria (depending on the order of the multipacting) and the SEY is greater than one [126]. The effect of multipacting is suppressed as soon as one of the criteria is not fulfilled. For SRF cavities, this has been achieved by optimizing the cavity geometry towards spherical and elliptical shapes for which all criteria for multipacting are only fulfilled for high accelerating gradients. However, multipacting is still an issue for non-elliptical cavities, couplers and waveguides as well as for the Quadrupole Resonator(s) due to their geometry [127, 128]. Moreover, it is also an issue for RF windows due to high SEY materials and in SRF electron sources (*SRF guns*) [129].

Above all, the development of materials beyond niobium require the evaluation of the SEY as a material parameter in order to avoid the return of multipacting as a performance limitation for elliptical

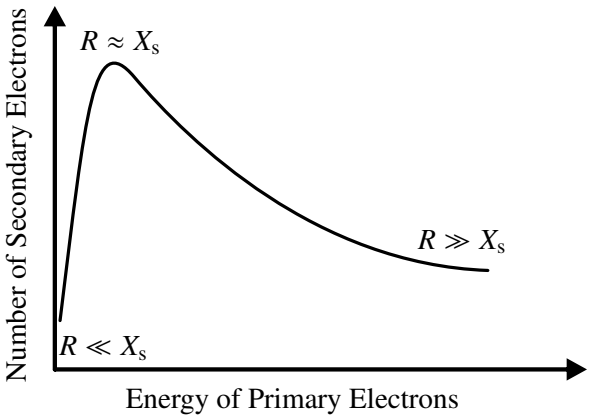

Figure 3.7.: Typical spectrum of the SEY.

cavities.

3.4.1. The Process of Secondary Electron Emission

The SEY represents the average number of secondarily emitted electrons per primary electron impacting the surface. The process is fully described in [130] and briefly summarized in the following: After impact, a primary electron travels through the material, loses energy due to scattering and produces secondary electrons while slowing down. With increasing incident energy the maximum penetration depth R of the primary increases. Although secondary electrons are generated along the whole path, the majority of secondaries is created at the end of the primaries path and the total number of secondary electrons increases with the energy of the primary electron. The secondaries diffuse through the material and are emitted if they reach the surface with a remaining energy high enough to overcome the surface-vacuum barrier. Their probability to escape decreases exponentially on a characteristic escape length X_s. The superposition of these two mechanisms yield the typical curved shape of the SEY curve as shown in Figure 3.7: For low incident energies the generated secondaries are likely to escape since $R \ll X_s$ but only a small number is generated. For high energies, many secondary electrons are generated deep in the material ($R \gg X_s$) so that a big fraction is absorbed and not emitted. For energies where the primaries' penetration depth is similar to the escape length, the SEY curve has its maximum, which is often referred to as *the* SEY value of a certain material or sample.

However, the maximum SEY of a material does not only depend on the energy of the primary electron, but also on the incident angle θ. If the primary electron trajectory is not perpendicular to the surface, the penetration depth is scaled by $\cos\theta$. As a result more secondaries are generated close to the surface and are more likely to be emitted into the vacuum. Thus, the peak in the SEY curve shifts up and the maximum is shifted to higher primary energies.

3.4.2. The Influence of the Surface on the Secondary Electron Yield

The SEY can be influenced by the condition of the surface in two ways: Surface roughness and cleanliness [131]. After the secondary electrons are diffused to the surface, they have to be energetic enough

to overcome the surface-vacuum barrier. However, if a secondary electron is emitted from the material it can still be reabsorbed due to surface roughness [130]. The rougher the surface, the less electrons are released into the vacuum, leading to a decrease in the SEY. However, superconducting RF applications require a smooth surface for good performance.

As secondary electron emission is a surface effect, also contaminants and native oxides on the surface have to be taken into account. As primary electrons tend to interact in particular with hydrocarbons and water, the measured SEY of an air-exposed surface is in fact a superposition of the SEY of the adsorbates and the top surface layer of the sample. Altough hydrocarbons and water cannot be avoided since they originate from exposure to air, long hydrocarbon chains can be split into shorter chains or amorphous carbon with hydrogen may be released to the vacuum by electron bombardment [132] or baking [133]. These processes are usually referred to as *conditioning*. Recently, amorphous carbon coatings have been used to reduce the SEY, as they have low SEY (≈ 1) [134] and therefore mitigate electron cloud effects in high energy particle accelerators [135].

3.4.3. Secondary Electron Yield for Conductors and Insulators

Although it is not possible to predict the SEY of a certain material, the SEY range can be estimated based on the electrical transport properties: Metals are known to have low SEY values, ranging from 0.5 for lithium to 1.8 for platinum [134]. In contrast, insulators have often (but not always) SEY values beyond 4 [134], while alloys range between 1.5 and 3 [136]. Insulators with an especially high SEY find application as coating material for dynodes in photomultipliers, for example MgO (SEY up to 15 [35]) .

The number of emitted electrons is given by the minimum energy necessary to overcome the surface-vacuum barrier (*minimum escape energy*) and the interaction of the internal secondaries with the material, i.e. how much energy they lose on their way to the surface. Independent of the material, internal secondaries lose their energy by scattering with phonons and defects. In the case of secondaries travelling through an insulator with energy less than the band gap, this scattering dominating. If their energy is higher than the band gap, they can also excite valence electrons into the conduction band, which is an additional loss contribution. However, typically all three contributions are small, so that the kinetic energy of many secondaries exceeds the minimum escape energy which is usually as low as 1 eV. As a consequence, many generated secondaries are emitted to the vacuum. In contrast to insulators, the energy loss of internal secondaries passing through a metal is dominated by scattering off electrons in the conduction band which results in a high energy loss. Moreover, the minimum escape energy in a metal is the sum of the work function and the Fermi level and is in the range of 10 eV.

Taking into account that electron scattering leads to much more energy loss than scattering with phonons and defects and that the minimum escape energy in metals is an order of magnitude higher compared to insulating materials, the significant difference in SEY values can be explained.

4. Instrumentation

Regular SRF cavity cold tests are a fast way to quantify the performance of an SRF cavity. Results usually comprise the surface resistance as function of RF field and temperature. Tests of bare cavities are usually performed in bath cryostats which typically cover a temperature range between 1.6 and 4.2 K. Some cryogenic systems deliver however only superfluid helium ($T \leq 2.1$ K). This makes the analysis of the BCS contribution difficult as the BCS resistance is comparatively small for the common frequencies. If a BCS fit is justified and the shift of the resonance frequency during warm up can be measured, material parameters like the penetration depth, electron mean free path, Ginsburg-Landau parameter and RRR can be derived [137].

While the dissipated power in regular cavities can be measured directly via the decay time of the electro-magnetic energy in the cavity and the law of energy conservation, the dissipated power in a flat sample independent of its host structure needs to derived differently, i.e. through a calorimetric method. Moreover, sample test cavities are designed for systematic studies of the surface resistance and aim therefore for high resolution measurements. Compared to cavity surfaces in the order of 1 m^2, the sample surface area is typically in the range of tens of cm^2. This makes it especially interesting for the development of new materials and coatings. To date there are numerous sample test cavities with calorimetric systems:

- JLab developed a sapphire loaded sample test cavity operating at 7.5 GHz characterizing samples with a diameter of 5 cm [81].
- CEA Saclay and IPN Orsay developed a sample test cavity operating at 4 and 5.6 GHz characterizing samples with a diameter of 12.6 cm [138, 139].
- SLAC commissioned two hemispherical cavities, one in copper and one in niobium, hosting samples of 5 cm diameter for surface resistance and quench studies at 11.4 GHz and down to 4 K [140].
- STFC is currently commissioning a three-choked cavity at 7.8 GHz for testing samples of 10 cm diameter [141, 142]
- CERN designed and operates a Quadrupole Resonator which allows testing samples of 7.5 cm diameter at 400 MHz, 800 MHz and 1200 MHz [143, 144]. HZB adapted and optimised the design for operation at 433 MHz, 866 MHz and 1300 MHz [145, 146].

Additionally, the Cornell University runs a non-calorimetric sample test cavity in the third generation which allows testing 12.7 cm large samples at 3.96 GHz [147]. A detailed review of the different systems can be found elsewhere [148].

The main disadvantage of most systems is the high frequency which is a consequence of the requirement of a small sample size. If one just considers the end plate of a pill box cavity as the sample, the sample diameter would be about 30 cm at 1.3 GHz and about 1.1 m for 400 MHz. If samples should be tested in this frequency range, a different approach needs to be found which was the starting point for the development of the Quadrupole Resonator.

4.1. The Quadrupole Resonator

CERN's Quadrupole Resonator was designed for characterizing niobium coatings at the LHC frequency of 400 MHz. A 3D model from the CST simulation is displayed in Figure 4.1 with the whole object in Figure 4.1a and detailed views in Figures 4.1b - 4.1d.

The Quadrupole Resonator is designed as a four wire transmission line made from two pairs of two superconducting rods each which are connected with an arc shaped piece. The two arc pieces face each other to form a loop parallel to the sample surface. The length of the rods corresponds to half of the wavelength of the fundamental quadrupole mode of 400 MHz. The sample size does not scale with frequency and just needs to be sufficiently large to cover the *illumination* area of the split loop. In this case the sample diameter was chosen to be 75 mm. The rods are placed in a host cavity for shielding, and a tubular port on the bottom side allows for sample mounting. The host cavity is connected to a turbo molecular pump with a dry membrane pump for oil free ultra high vacuum. The sample port has a 2 mm wider diameter than the sample so that a coaxial structure is created to ensure that the RF fields decay exponentially in the cut-off gap so that losses at the sample flange can be neglected and only losses on the sample surface contribute to the surface resistance measurement. The support tube has a length of about 11 cm to ensure a sufficient long cut-off gap.

Figure 4.2 shows the magnetic and electric field distribution on the sample surface. The Quadrupole Resonator can also be excited in harmonics of the fundamental quadrupole mode. Since 2012, RF equipment for not only 400 MHz, but also 800 MHz and 1.2 GHz is available [144]. The field distribution on the sample surface remains almost the same which allows conclusions to be drawn about the frequency dependence of the surface resistance.

The measurement of the surface resistance relies on a DC-RF compensation method which will be addressed in Section 4.1.1. This calorimetric method requires excellent electrical and thermal contact between the sample disk and the support structure which is guaranteed by electron beam welding of the two. The DC (heating) power is provided by a heater which is mounted on the bottom side of the sample along with four temperature sensors, as shown in Figure 4.3. This thermometry chamber is connected to a turbo molecular pump for pumping isolation vacuum. The heater is rated with 1/8 W at room temperature and is operated up to 1 W at cryogenic temperatures. The maximum achievable sample temperature is given by the maximum heater power and about 15 K for 1 W. A temperature controller from Lake Shore Cryogenic, Inc. reads all temperature diodes and controls the heater power through an proportional–integral–derivative (PID) algorithm.

The RF field reach for measurements is limited by the quench field of the Quadrupole Resonator. The maximum magnetic field of the whole assembly is on the rods and the corresponding field on the sample surface is about 18 % lower. The Quadrupole Resonator quenches when the magnetic field on

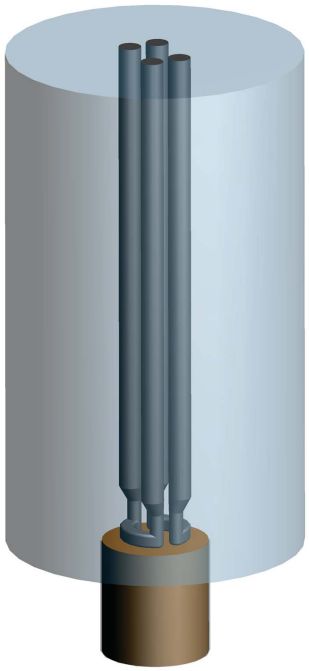

(a) CST model of the Quadrupole Resonator with host cavity (blue), superconducting rods (grey) and sample under test (orange).

(b) Detailed view: lower part of the superconducting rods with the pole shoes (grey) with the sample (orange) underneath.

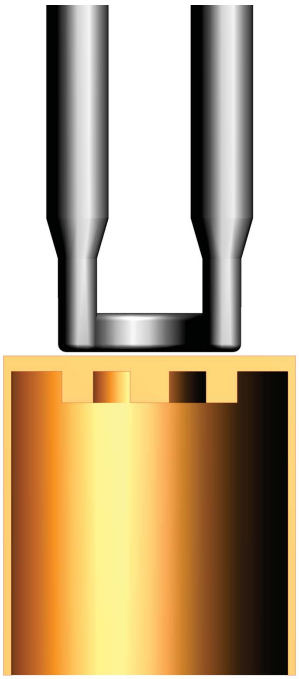

(c) Cut view along the x-axis through the rods (grey) and the sample cylinder (orange).

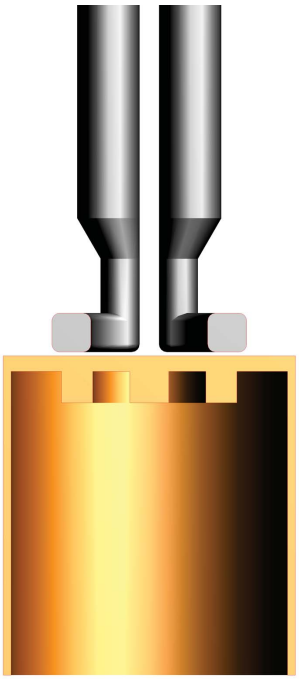

(d) Cut view along the y-axis through the rods (grey) and the sample cylinder (orange).

Figure 4.1.: CST model of the Quadrupole Resonator.

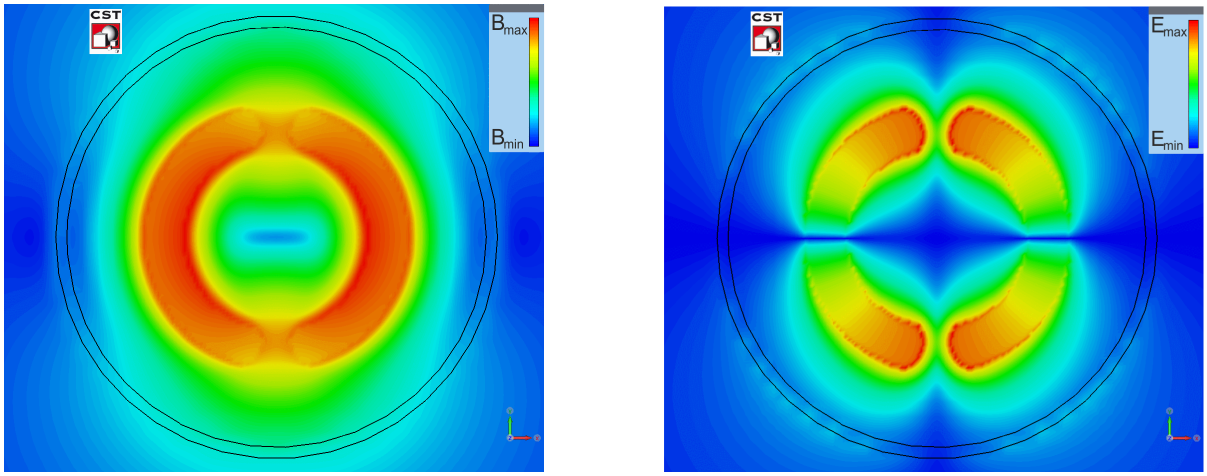

(a) (b)

Figure 4.2.: (a) magnetic and (b) electric field distribution on the sample surface.

the sample reaches 60 mT at 400 MHz, 30 mT at 800 MHz and 25 mT at 1.2 GHz. This limitation to rather low fields is most likely due to a defect on the QPR host cavity surface as it quenches at the same field level for different duty cycles. It must also be kept in mind that the Quadrupole Resonator is manufactured from medium quality (RRR 50 for the cavity, RRR 100 for the rods, RRR 250 for the pole shoes) niobium. This makes defects such as inclusions more likely and lowers the materials capability of stabilising a defect due to the lower thermal conductivity.

In summary, the current set-up allows measurements of the surface resistance:

- at 400 MHz, 800 MHz and 1200 MHz.
- at any temperature between 2 and 15 K.
- up to RF magnetic fields of 60 mT.

For operation, the Quadrupole Resonator is immersed in a 150 litre liquid helium bath cryostat with connections for pumping the cavity vacuum, the isolation vacuum of the thermometry chamber, and the helium bath in order to decrease the boiling point of the helium. A detailed overview over the cryogenic infrastructure can be found in the Appendix A. The helium pumping line is equipped with a butterfly valve and a pressure gauge on top of the top plate of the cryostat. A PID controller regulates the opening of the butterfly valve in order to stabilize the helium pressure to a set reference point. For reference pressures below the λ-point (50 mbar), the liquid helium pressure can be stabilized to $\pm 10\,\mu$bar which corresponds to temperature fluctuations of less than 1 mK. The top plate of cryostat hosts feedthroughs for the helium level gauge, a heater for evaporating the liquid helium, the vacuum pressure gauge of the cavity and temperature sensors and heater, as well as three RF power lines. Figure 4.4 depicts the RF chain for the Quadrupole Resonator.

A signal generator is the source of the incident RF signal which is then amplified and fed into the Quadrupole Resonator via a strongly coupled antenna. The loaded quality factor Q_L is in the order of 10^6 at 400 MHz. Two directional couplers are used to divert a small portion of the incident signal towards a power meter and phase shifter. A circulator protects the amplifier from reflected power from

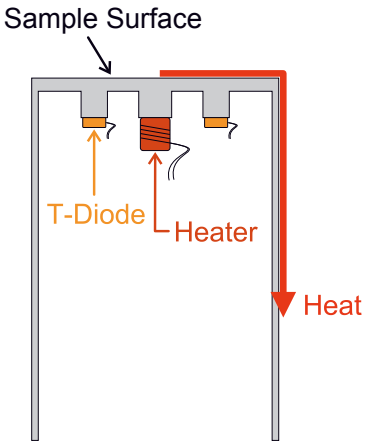

Figure 4.3.: Heat flow along the QPR sample

the cavity by deflecting the power into a load. An additional directional coupler allows measuring the reflected power with a power meter. A second strongly coupled antenna which has the same coupling as the input antenna ($\beta \approx 100$) couples out almost all of the power, leading to only small dissipation in the cavity. The Quadrupole Resonator serves here as a narrow band filter. The output power feeds the phase-locked loop (PLL), which mixes the incident and the output signal and returns a DC signal proportional to the difference in RF frequency of forward and transmitted signal. This signal is used by the signal generator for the frequency modulation. In this way, the resonance is stable under external perturbations like vibrations or changes in helium, vacuum or radiation pressure. The third weakly coupled antenna is used to measure the transmitted power which gives the stored energy in the cavity. A spectrum analyser is used for observing the RF signals and the selection can be made with a switch box with inputs for the incident, reflected and transmitted signal. All data acquisition is done through a LabVIEW interface.

4.1.1. Measuring the Surface Resistance

The measurement principle relies on a calorimetric technique where the dissipated power by the RF is derived by compensating it using a DC heater [92]. Besides the DC heater the sample is equipped with four temperature sensors radial symmetrically distributed as sketched in Figure 4.3.

Figure 4.5 displays how the dissipated RF power is balanced by DC heating: Starting from the temperature of the helium bath T_{bath}, the sample is warmed up to a temperature of interest T_{interest} and the required DC heater power P_{DC1} is measured. The RF is switched on and the sample temperature rises due to dissipation. The DC heater power is then reduced to bring the sample back to the temperature of interest, yielding P_{DC2}. P_{DC1} and P_{DC2} are measured with a 6 1/2 digit voltmeter.

The power dissipated in the sample P_{RF} is the the difference in heater power with and without RF, and is proportional to the surface resistance R_{S}:

$$P_{\text{RF}} = P_{\text{DC1}} - P_{\text{DC2}} = \frac{1}{2\mu_0^2} R_{\text{S}} \int_{\text{Sample}} \left|\vec{B}\right|^2 dS \tag{4.1}$$

The integrated magnetic field over the sample surface S is directly proportional to the stored energy

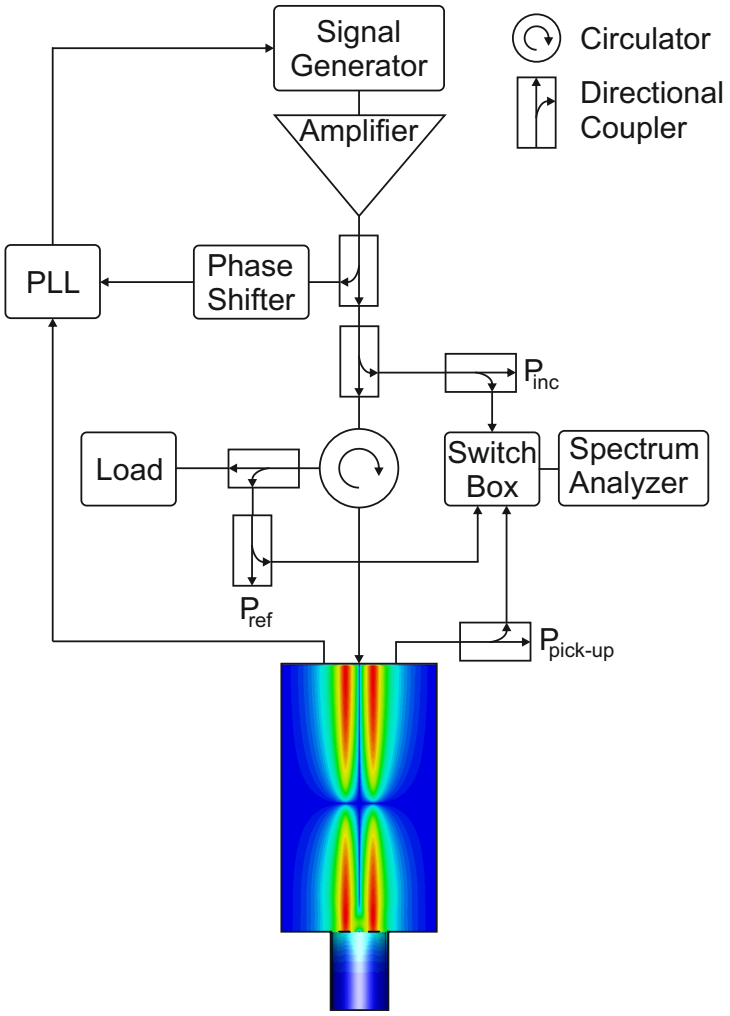

Figure 4.4.: RF chain of the Quadrupole Resonator as installed in CERN's Cryolab. Attenuators for protecting power sensitive equipment are not shown.

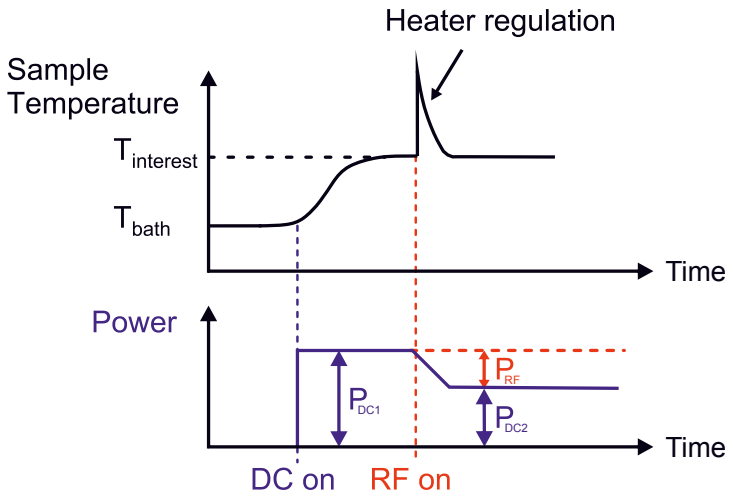

Figure 4.5.: The Calorimetric Technique: The dissipated power P_{RF} is compensated with a DC heater.

Table 4.1.: CST parameters describing the ratio of cavity fields and relating them to the stored energy according to Equation 4.2 and 4.3.

f [MHz]	c_1 [m^{-2}]	c_2 [$T^2\,J^{-1}$]	G_{Sample}
399.6	1408	0.105	106.3
803.1	1403	0.105	212.9
1211.1	1569	0.121	311.6

U in the QPR, and the square of the peak magnetic field on the sample surface B^2_{peak}. A CST simulation yields both relations and we can introduce the constants

$$c_1 = \frac{B^2_{\text{peak}}}{\int_{\text{Sample}} \left|\vec{B}\right|^2 dS} \qquad \text{and} \qquad c_2 = \frac{B^2_{\text{peak}}}{U}. \tag{4.2}$$

Correspondingly to cavity figure of merits, a geometry factor can be introduced:

$$G_{\text{Sample}} = R_{\text{S}} \cdot Q_{\text{Sample}} = 2\mu_0^2 \frac{\omega U}{\int_{\text{sample}} \left|\vec{B}\right|^2 dS} = 2\omega\mu_0^2 \frac{c1}{c2} \tag{4.3}$$

Table 4.1 summarizes c_1, c_2 and the geometry factors for the three available frequency modes. The differences of c_1 and c_2 between the different modes reflect that the field distribution is very similar but not identical, in particular for the 1200 MHz mode.

Making use of the loaded quality factor of the cavity

$$Q_{\text{L}} = \frac{\omega U}{P_{\text{L}}} \tag{4.4}$$

and substituting U in Equation 4.4 with Equation 4.2, the peak magnetic field can be calculated as:

$$B_{\text{peak}} = \sqrt{c_2 \tau P_{\text{L}}} \tag{4.5}$$

where τ is the decay time of the Quadrupole Resonator and P_{L} is the loaded power, i.e. the dissipated power in the cavity walls and the power radiated into the couplers.

Moreover, $\int_{\text{sample}} \left|\vec{B}\right|^2 dS$ can be expressed through c_1 and c_2 and Equation 4.1 transforms to:

$$R_{\text{S}} = \frac{2\mu_0^2 \cdot (P_{\text{DC1}} - P_{\text{DC2}})\, c_1}{c_2 \tau P_{\text{L}}}. \tag{4.6}$$

Since the input and the output antenna have the same coupling ($\beta \approx 100$), no power is reflected and all power is transmitted, and coupled out on the output antenna. This allows the assumption that incident and transmitted power are equal and

$$P_{\text{L}} = 2P_{\text{inc}} = 2P_{\text{t}}. \tag{4.7}$$

A weakly coupled pick-up antenna with the same geometry as the input and output antenna measures directly a fraction of the transmitted power. The relation $P_{\text{inc}}/P_{\text{pick-up}}$ is derived from an RF power calibration for each cold test and each mode individually.

4.1.2. Measuring the Penetration Depth

The change in effective penetration depth can be derived from the shift of resonance frequency with temperature. Applying Slaters theorem [149], the changes in stored energy U is proportional to the changes in the resonance frequency Δf. The penetration of the electric field into the superconductor can be neglected and we find [94]:

$$\frac{\Delta U}{U} \sim \frac{\Delta f}{f_0} = -\frac{\mu_0^2}{4U} \int_V^{V+\Delta V} |H|^2 \, dV \tag{4.8}$$

The change of penetration depth $\Delta\lambda_{\text{eff}}$ indicates a change of electromagnetic volume and can be expressed through the sample's geometry factor and is proportional to the shift in resonance frequency $\Delta f = f_0 - f_{0\text{K}}$:

$$\Delta\lambda_{\text{eff}} = -\frac{G_{\text{Sample}}}{\pi\mu_0 f_{0\text{K}}^2}\Delta f \tag{4.9}$$

f_{0K} is the resonance frequency at 0 K and has to be estimated based on the low temperature values. The penetration depth changes with temperature, following the (empirical) Gorter-Casimir relation:

$$\lambda_{\text{eff}}(T, \ell) = \frac{\lambda(0, \ell)}{\sqrt{1 - \left(\frac{T}{T_c}\right)^4}} \tag{4.10}$$

$\lambda(0, \ell)$ is the penetration depth at 0 K with the finite mean free path ℓ taken into account.

The resonance frequency f_0 can easily be determined with a network analyser. With two ports connected to the two strongly coupled antennas, the transmitted signal $S21$ or $S12$ of the QPR can be measured. A low intermediate frequency (IF) bandwidth ($\leq$ 100 Hz) and a narrow span[1] increase the accuracy of the measurement significantly. Moreover, the network analyser can directly display the 3 dB bandwidth. Using the according centre frequency instead of the frequency with highest power, is more accurate [137]. The resonance frequency is very sensitive to fluctuations in the helium bath pressure but the stability of $\pm 10\,\mu$bar ensures a reasonable precision. In contrast to the penetration depth measurement on a cavity where the frequency shift is typically measured during warm up with the cavity is gasous helium, the QPR stays immersed in liquid helium. Only the sample is warmed up with the DC heater and the frequency shift as function of the sample temperature is measured.

From fitting the effective penetration depth at 0 K, $\lambda(0, \ell)$, and for not too small mean free paths, ℓ can be calculated using Pippards expression cited in Equation 3.37. It follows:

$$\ell = \frac{\pi\xi_0}{2\left(\left(\frac{\lambda(0,\ell)}{\lambda_{\text{L}}}\right)^2 - 1\right)} \tag{4.11}$$

The London penetration depth λ_L and the coherence length ξ_0 are the fundamental material parameters for $\ell \to \infty$ and 0 K. The measured penetration depth is not an absolute measurement but a measurement relative to the fundamental parameters λ_{L} and ξ_0, see Equation 3.39 and 3.40.

The Ginsburg-Landau parameter and RRR can then be calculated from Equation 3.38 and 3.41.

[1] Depending on the mode and the temperature between 500 Hz and 3 kHz

4.1.3. Measuring the Normal Resistance

Measuring the normal resistance of a sample allows an estimate of the RRR which might be used for consistency checks with the results of the penetration depth and low field R_s measurements. For this measurement, the quality factor of the Quadrupole Resonator is measured with a network analyser using the 3 dB method. The measured Q is the loaded Q of the whole system and corresponds to the inverse sum of the quality factors of the QPR host cavity Q_{QPR}, the sample Q_{sample} and the couplers Q_{ext}:

$$\frac{1}{Q_{\mathrm{L}}} = \frac{1}{Q_{\mathrm{QPR}}} + \frac{1}{Q_{\mathrm{sample}}} + \frac{1}{Q_{\mathrm{ext}}} \tag{4.12}$$

The surface resistances of the sample and the host cavity are in the order of tens of nΩ at the helium bath temperature of 1.8 K and 400 MHz. The corresponding quality factors are in the order of 10^{10} for the sample and 10^9 for the host cavity. Both values are orders of magnitude lower than the measured Q_{L} of 10^6. Hence, the measured Q is dominated by coupling of the antennas, i.e. $Q_{\mathrm{L,sc}} = Q_{\mathrm{ext}}$ at low temperature.

When the sample is warmed up to the normal conducting state and its quality factor contributes significantly to the loaded Q. Since the sample is thermally decoupled from the QPR, the host cavity remains at 1.8 K, so that Q_{QPR} does not change and remains negligible. After measuring Q_{ext} in the superconducting state, the quality factor of the normal conducting sample can be derived from measuring Q_{L} with the quenched sample:

$$\frac{1}{Q_{\mathrm{L,nc}}} = \frac{1}{Q_{\mathrm{sample}}} + \frac{1}{Q_{\mathrm{L,sc}}} \tag{4.13}$$

The normal resistance can finally be derived by using the geometry factor and the RRR can be calculated according to the skin effect using the electrical conductivity at room temperature σ_0:

$$R_{\mathrm{nc}} = \frac{G_{\mathrm{sample}}}{Q_{\mathrm{sample}}} = \sqrt{\frac{\pi f_0 \mu_0}{\sigma_0 \cdot RRR}} \tag{4.14}$$

It needs to be considered though that in the normal state the RF probes the material within the skin depth which is for niobium at 400 MHz in the order of single μm. Compared to the penetration depth of the superconducting state, the skin depth is significantly larger and the according normal resistance and RRR correspond to the purity of much thicker surface layer. For bulk samples, this essentially means measuring the bulk properties of the sample while for thin film samples the RF is leaking through the film into the substrate and the resulting value will be a superposition of both materials.

4.1.4. Measuring the Quench Field

The Quadrupole Resonator also allows an estimate of the quench field of the sample under investigation. To do so, the Quadrupole Resonator is excited with high power pulses. A low duty cycle ($\leq$ 10 %) suppresses quenching due to thermal runaway so that the sample will only quench magnetically if the field is sufficiently high. When the rising slope of the power pulse reaches the quench field of the sample the transmitted power breaks down as sketched in Figure 4.6. Since the magnetic field of the Quadrupole Resonator rods is higher than on the sample, the sample temperature has to be chosen such that the quench field of the sample is lower than the quench field of the Quadrupole Resonator for a given

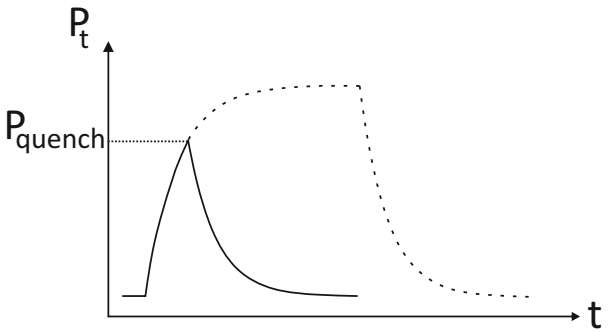

Figure 4.6.: Trace of the transmitted power for the derivation of the quench field.

bath temperature. Due to the fact that the Quadrupole Resonator quenches prematurely (even for the medium material quality), the quench field of niobium samples can only be measured at temperatures above 8 K. Measuring the sample quench field at different (high) temperatures allows then to fit the zero temperature quench field through

$$B_{\text{quench}}(T) = B_{\text{quench}}(0\,\text{K}) \cdot \left(1 - \left(\frac{T}{T_\text{c}}\right)^2\right). \tag{4.15}$$

4.1.5. Thermal Cycling

A fundamental property of the Quadrupole Resonator is that it's sample is thermally decoupled from the host cavity. This allows measuring the resonance frequency shift as function of sample temperature as described in the previous section, but also allows for thermal cycling of the sample independently of the QPR host cavity. Here, thermal cycling means warming the sample up just above the transition temperature typically to 12 K with the DC heater. The sample can be cooled down in a controlled manner, for instance with a defined cooling speed or with a specific ambient magnetic field. The first is achieved by varying the DC heater power during cool down, the latter by powering a small solenoid mounted in the thermometry chamber as will be in detail described in Section 4.3.

4.2. Thermal Simulations

The experimental data that will be presented in Chapter 5 will show that thermal effects must be considered for interpretation. This section therefore introduces thermal simulations of the QPR sample to gain a better understanding of the thermal behaviour of the sample under test. The simulations indicate that due to the single heat source in the center of the sample, temperature gradients arise when that heater is on. This applies not only to warm-up and cool down procedures but also to the steady-state during the RF-DC-compensation measurements. If the temperature gradient is significant depends foremost on the thermal conductivity of the part. For the reactor grade bulk niobium sample, temperature gradients appear quite significant while a Nb/Cu sample benefits from the excellent thermal properties of the copper substrate.

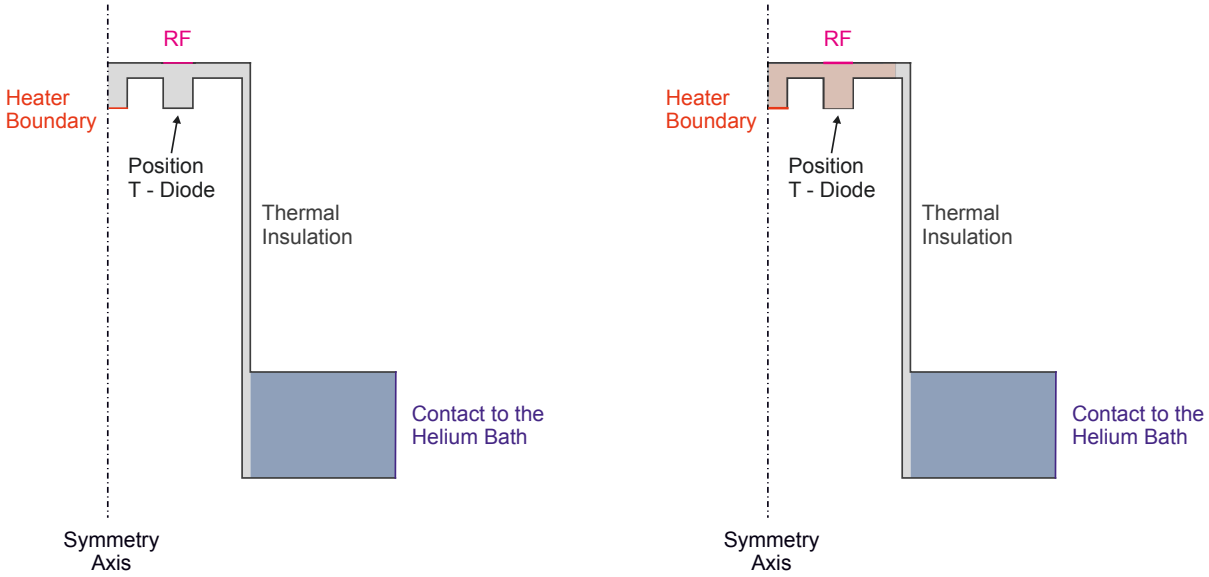

Figure 4.7.: Axial symmetric geometry for the COMSOL simulation for (a) a bulk niobium sample and (b) a copper substrate.

For simulating thermal effects in the Quadrupole Resonator sample, COMSOL Multiphysics® [150] was chosen as it allows both steady-state and time dependent analyses of thermal effects using temperature dependent quantities like the thermal conductivity and specific heat.

Since the sample and the Quadrupole Resonator are thermally decoupled, only the sample with its support needs to be simulated as long as only thermal effects are of interest.

Figure 4.7 shows the COMSOL model of the sample for both niobium and copper, both with a niobium the support tube and a stainless steel support flange. The niobium coating is modeled by assigning the niobium properties just to the surface boundary of the sample, while the sample bulk material is identified as copper. Due to the sample's cylindrical symmetry, the simulation was reduced to two dimensions with a symmetry axis in the center of the sample and its support. All boundaries to vacuum and the interface to adjoining stainless steel flanges of the host cavity were defined as thermally insulating boundaries. The outside of the support flange is the only contact to the helium bath. The helium bath temperature is 1.8 K so the liquid helium is in the superfluid state, which has a very high thermal conductivity in the order of 10^5 to 10^6 W/(m · K) [34]. Therefore the stainless steel-helium interface is set to a fixed temperature boundary of 1.8 K.

The DC heater is represented by a boundary heat source with a defined heat input in Watt. In order to account for dissipated power due to the RF losses, a second boundary heat source is defined on the RF side of the sample surface. The RF boundary heat source is limited to the RF high field region which coincides with the width of the ring on the bottom side of the sample where the temperature diodes are mounted on as shown in Figure 4.7.

The materials used are reactor grade bulk niobium, oxygen-free electronic (OFE) copper and stainless steel 316 LN. Single pieces of bulk niobium and/or copper are electron beam welded while niobium is brazed to the stainless steel flange. Heat transport through the weld, the brazing as well as into the liquid helium are treated as perfect transitions. Figure 4.8a shows the thermal conductivity at cryogenic tem-

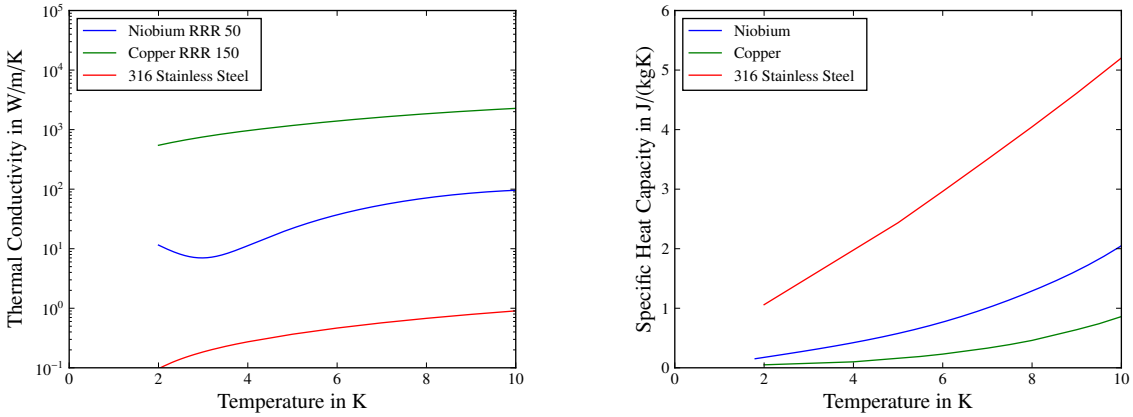

(a) (b)

Figure 4.8.: Thermal conductivity (a) and specific heat (b) for niobium, copper and 316 stainless steel.

peratures as used for the simulation. The thermal conductivity of reactor grade niobium was previously measured in the range between 1.8 K and 10 K [92]. The NIST database provides data for the thermal conductivity of copper with different RRR and different types of stainless steel [151]. As OFE copper has typically RRR values between 100 and 200, a thermal conductivity of copper with RRR 150 is used for this simulation. The NIST database does not provide data on stainless steel 316 LN but only stainless steel 316. The label LN indicates that the steel has an extra low carbon content ($< 0.03\,\%$ compared to $< 0.08\,\%$ for 316) and is nitrogen enriched ($0.10 - 0.18\%$ compared to $0.10\,\%$). As there is no data on the thermal conductivity of 316 LN at cryogenic temperatures, the data for stainless steel 316 is used.

The specific heat of a material is given by the Debye temperature and does not depend on the purity, respectively on the RRR. Cryogenic data for copper and stainless steel 316 is taken from the NIST database as well, but only covers a temperature range down to 4 K. The specific heat data sets are extrapolated following a T^{-3} dependency down to 2 K for an estimate of the given quantity. The thermal conductivities are extrapolated linearly down to 2 K following the Wiedemann-Franz law. The specific heat data for niobium is taken from Reference [152]. The data represents the specific heat of normal conducting niobium down to 1 K but does not account for the change in the superconducting state. The specific heat of superconducting niobium decreases exponentially and is smaller than in the normal state. This will affect any time dependent simulation but the order of magnitude should remain valid.

Figure 4.8 shows the thermal conductivity and specific heat capacity data as used for the simulation. As the thermal conductivity of stainless steel, niobium and high quality copper differ in orders of magnitude, the used data sets should give a good estimate.

4.2.1. DC-RF Compensation Method

The measurement principle of the Quadrupole Resonator relies on the assumption that the heat deposition is the same for pure DC heating and mixed DC-RF heating. The reference point is the temperature of the surface where the temperature diode is mounted on. For an accurate compensation it has to be the same heat deposition independent of source. As outlined in the previous section, the RF heat dissipation

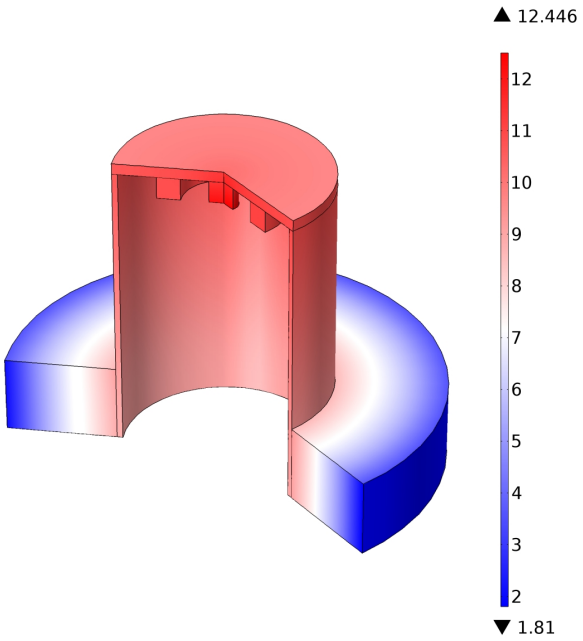

Figure 4.9.: Temperature profile along the sample, sample cylinder and flange. Simulated for 850 mW DC heating power.

is modeled by a heat boundary source matching the high field region as indicated in Figure 4.7.

Step 1: Pure DC heating Figure 4.9 shows the temperature profile when constantly heating with 850 mW using the DC heater, as is typically done for thermal cycling. The simulated steady-state temperature at the position of the temperature diodes of about 11 K is in good agreement with the experiment. The simulation shows that all niobium parts are normal conducting.

Step 2: Heating to 2 K and 4 K In the following the DC heating power required to heat the sample to 2 K respectively to 4 K is simulated and compared with measurement values. For the bulk niobium sample the simulation overestimates the required power by 18 % at 2 K and by 24 % at 4 K. For the copper sample the required DC power is overestimated by 19 % at 4 K and by about 58 % at 2 K. Deviations are plausible considering not only the perfect thermal contacts but also the extrapolation of the thermal conductivity data beyond the actual data and the uncertainty of how well the used material is actually represented by the data. The large deviation for copper at 2 K indicates that the extrapolation of the thermal conductivity below 4 K yields higher values than the measurements imply lower thermal conductivity than estimated.

Step 3: Compensating DC heating with RF Based on the pure DC heating case, the DC-RF compensation is simulated. The required power to heat up to 2 respectively 4 K is split between the DC heater and the RF heater boundary with varying fractions. The heat flow from the DC heater along the sample, the support and into the helium is shown in Figure 4.3. Due to the low thermal conductivity of the bulk niobium sample, the temperature on the face where the temperature diode is mounted on is lower than the reference temperature when the total power is split between DC and RF heating. Since

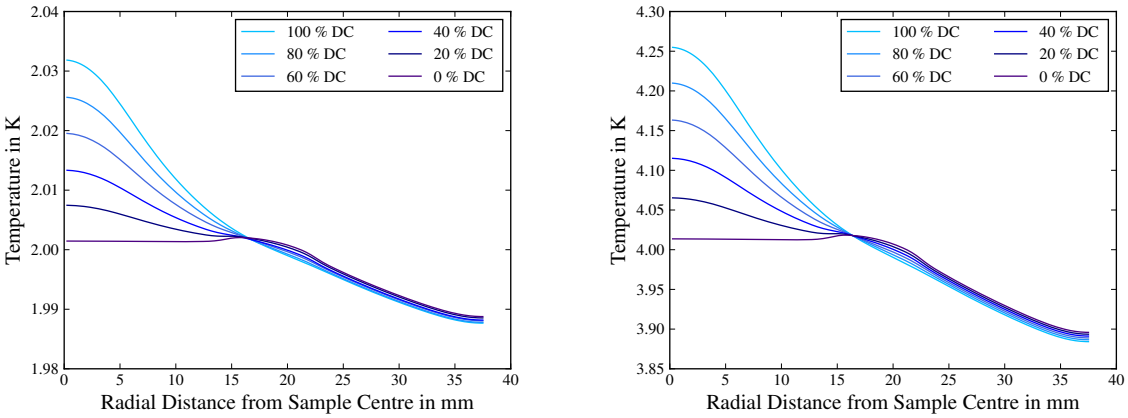

Figure 4.10.: Temperature profile across the sample surface for bulk niobium at (a) 2 K and (b) 4 K.

the DC heater power is controlled by the temperature of the temperature reading at this position, a lower temperature in this position will lead to more DC heating and therefore an overestimation of the surface resistance. The additional DC heater power that is required to bring the position of the temperature diode to the reference temperature is calculated for different fractions of DC/RF heating ranging from 20 % to 100 % RF heating. The additional DC heating power increases with RF heating power so that the DC power in the measurement will be overestimated between 0.08 % at 2 K and 20 % RF heating and 0.61 % at 4 K and 80 % RF heating. The measured power P_{DC2} on reactor grade bulk niobium can be corrected via

$$P_{\mathrm{DC2,corr}} = P_{\mathrm{DC2}} \cdot \left(1 + 0.0061 \frac{P_{\mathrm{RF}}}{P_{\mathrm{DC1}}}\right) \qquad \text{at 2 K and} \tag{4.16}$$

$$P_{\mathrm{DC2,corr}} = P_{\mathrm{DC2}} \cdot \left(1 + 0.0075 \frac{P_{\mathrm{RF}}}{P_{\mathrm{DC1}}}\right) \qquad \text{at 4 K.} \tag{4.17}$$

For typical reactor grade bulk niobium data, this correction will reduce the surface resistance measurement by less than 0.2 nΩ.

For the copper case, the DC heating power will be overestimated by less than 0.02 % for the same combination of temperature at DC/RF ratio. This effect can therefore be neglected and no correction is necessary.

Moreover, the temperature profile across the sample surface changes with the percentage of RF heating. Figure 4.10 and 4.11 show the temperature profiles for the bulk niobium and the copper at 2 and 4 K for different DC-RF heating ratios.

All profiles have in common that the bell shape of the temperature curve vanishes with increasing fraction of RF heating. The temperature difference between sample center and sample edge is however much smaller for the copper than for the bulk niobium. This is again due to the significantly higher thermal conductivity of the copper substrate.

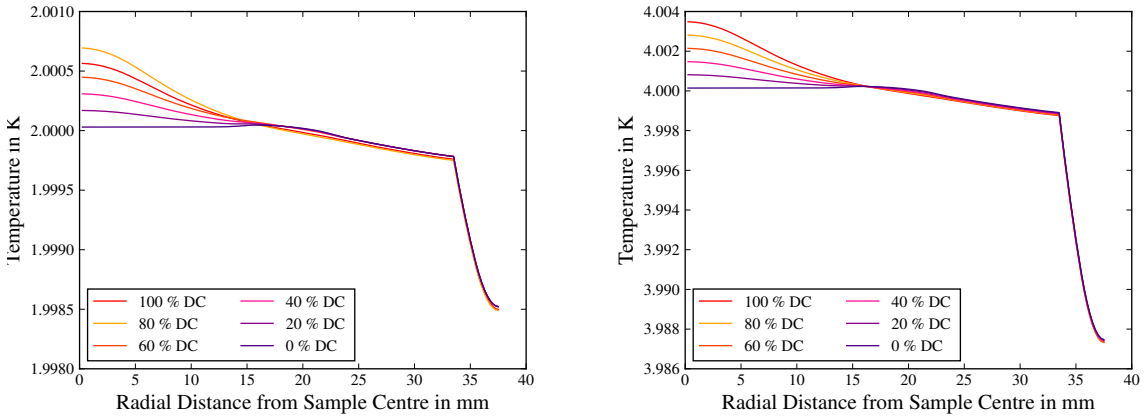

Figure 4.11.: Temperature profile across the sample surface for niobium on copper at (a) 2 K and (b) 4 K.

4.2.2. Superconducting Transition

In order to evaluate the moment of superconducting transition the simulation was extended with a dynamic study.

Corresponding to the thermal cycling as described in Section 4.1.5, the simulation starts with the steady state heating of the sample in the normal conducting state with a DC heating of 850 mW. For the dynamic study, the DC heater power is reduced according to a thermal cycle between 0 mW to 500 mW and the temperature profile of the sample is calculated as function of time.

Figure 4.12 compares how a bulk niobium and a niobium on copper sample becomes superconducting in the absence of DC heating during cool down. The plots show the contour line of the critical temperature, 9.2 K for the bulk niobium, 9.3 K for the niobium film, for different moments in time. Due to the conduction cooling, the sample cools from bottom to top and from edge to the center in both cases. A closer look on the sample and RF surface reveals that the phase front is always normal to the surface in both cases.

For the bulk niobium sample, two isolated normal conducting regions appear during the cool down: the bottom side of the ring onto which the temperature diodes are mounted and the bottom side of the central part that holds the DC heater. Under the right cool down scheme and assuming that not all field can be expelled from the niobium, any ambient field would be pushed along the phase front and might be trapped on the bottom side of the sample where no RF is applied. For the niobium film sample, the T_c contour line travels in the same way as for the bulk niobium. Since copper does not become superconducting, any ambient field would be trapped in the centre of the sample or at the niobium-copper interface close to the center of the sample unless it is expelled.

Besides the temporal transition from normal to superconducting state, the temperature profile across the sample surface in the moment of the transition can be compared. The moment of transition is here defined as the moment when the position of temperature diode crosses the critical temperature as this is also accessible in the experiment. Figure 4.13 shows the temperature profile across the bulk niobium and the copper sample when crossing T_c. Both samples show a bigger temperature difference between

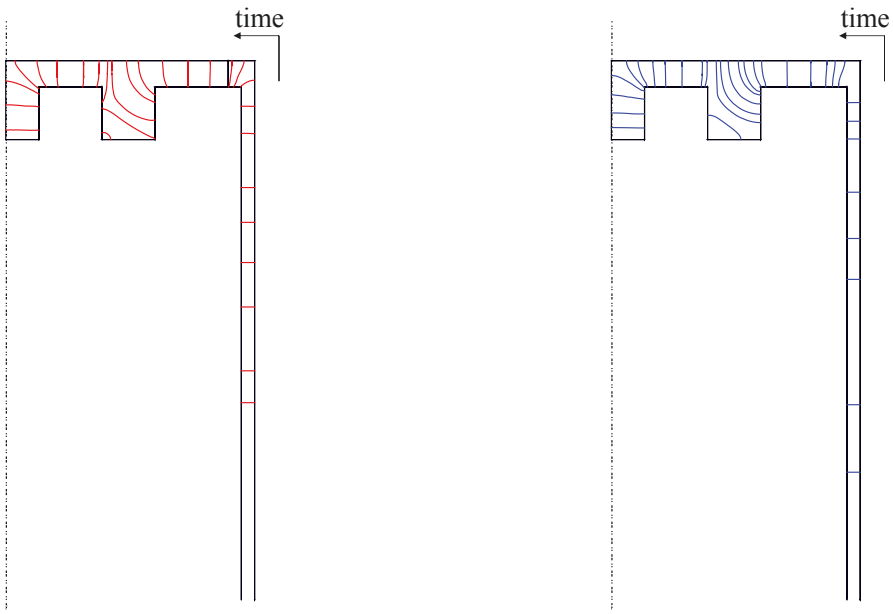

(a) (b)

Figure 4.12.: Superconducting phase transition as the QPR sample cools down for (a) a bulk Nb sample and (b) for a Nb/Cu sample.

sample center and edge with increasing DC heating power during cool down, but the temperature difference is significantly bigger for bulk niobium due to the lower thermal conductivity.

The higher the DC heating power during cool down is, the slower the sample cools down and the slower it crosses the superconducting transition. In Figure 4.14 the temperature difference between sample center and edge is plotted as function of DC heating power and fitted with a linear trend. The temperature gradient across the sample of 37.5 mm radius can be calculated via

$$\Delta T_{\text{bulk}} = (890.5 \pm 6.7)\,\text{mK/W} \cdot P_{\text{DC}} + (11.9 \pm 2.0)\,\text{mK} \quad \text{for the bulk Nb sample and} \tag{4.18}$$

$$\Delta T_{\text{film}} = (61.5 \pm 0.3)\,\text{mK/W} \cdot P_{\text{DC}} + (0.4 \pm 0.1)\,\text{mK} \quad \text{for the Nb/Cu sample.} \tag{4.19}$$

This dependence on the DC heating power will be used in Section 5.1.8 to correlate the measured cooling rate at which a sample becomes superconducting and the according temperature gradient.

4.3. Upgrade: Coil for Trapped Flux Studies

The QPR is upgraded with a small solenoid for applying external magnetic fields to the sample. This allows studying the trapped flux behaviour of the sample under test. The measurements and results which will be presented in Sections 5.1.8 and 5.1.9 are supported by simulations of the magnetic field distribution on the sample depending on the (superconducting) state of the sample. The simulations suggest that the pole shoes and the QPR host cavity which remain superconducting throughout all tests, interfere strongly with the magnetic field created by the coil. As a result, the magnetic field on the sample surface is much lower that if the environment was fully normal conducting. Furthermore, the magnetic

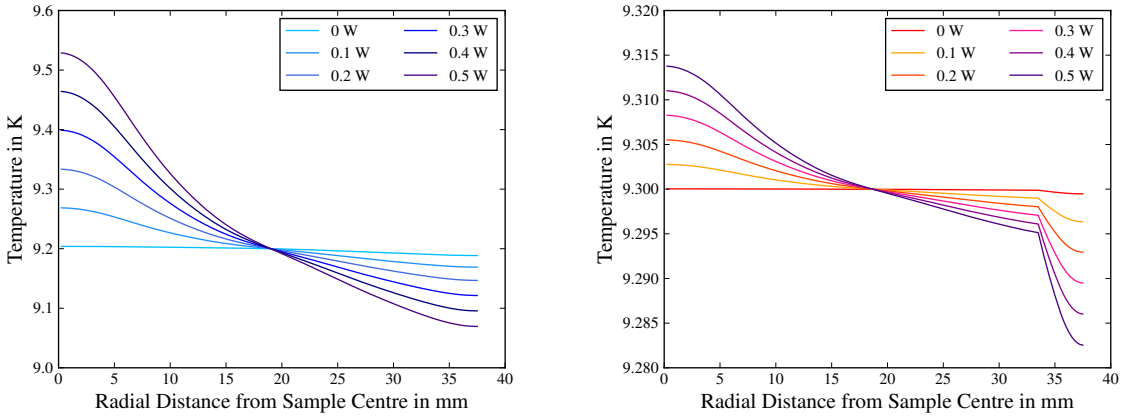

Figure 4.13.: Temperature profile across the sample surface in the moment of superconducting transition for (a) bulk niobium and (b) a niobium film on copper.

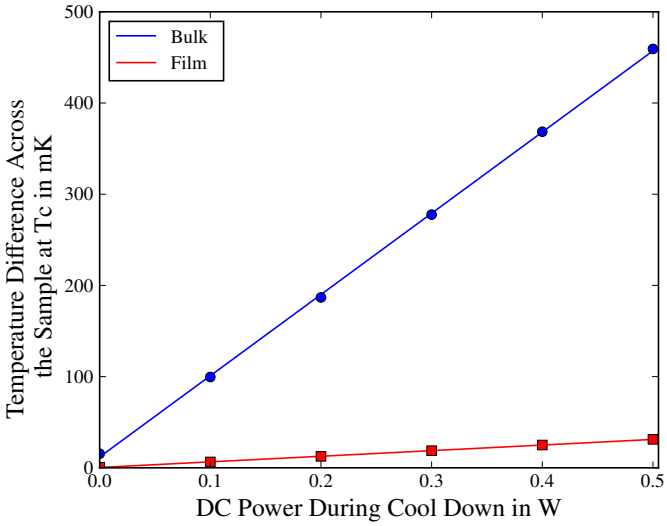

Figure 4.14.: Temperature difference across the sample as a function of DC heating power during cool down in the moment of superconducting transition.

field distortion at the position of the magnetic field probe is too big to make a reliable estimation of the expelled magnetic flux when the sample becomes superconducting in the presence of that field.

4.3.1. Magnetic Coil Design

The inside of the sample cylinder is referred to as the thermometry chamber. It hosts the DC heater and temperature diodes. It was additionally equipped with a small DC coil for trapped flux studies. The coil consists of two layers of 34 turns each, wound around a polytetrafluoroethylene (PTFE) cylinder with an outer diameter of 65 mm. The outside of the coil is in direct contact with the inner side of the sample cylinder and provides cooling. On the inner side of the PTFE support cylinder a single axis magnetic field probe was mounted to monitor the ambient magnetic field. The fluxgate (FG) Mag-01H is designed for small magnetic fields in a cryogenic environment [153]. The sample, its support cylinder and the position of the magnetic field probe FG are indicated in Figure 4.15.

For the simulation of DC magnetic fields, the magnetic screening from all superconducting parts has to be taken into account. Any superconducting surface will expel any ambient field due to the Meissner effect and will therefore alter the local magnetic field distribution. Due to the thermal decoupling of the Quadrupole Resonator and its sample the rods and the host cavity stay superconducting independently of the sample temperature.

4.3.2. Simulation of DC Magnetic Fields

The DC coil was integrated in the existing CST simulation of the Quadrupole Resonator and the DC magnetic field was calculated using the magneto-static solver. The superconducting sample port and the rods which face the sample surface in 1 mm distance have to be taken into account as the magnetic field cannot penetrate these structures. Based on the thermal simulation discussed in Section 4.2, it is assumed that the sample and sample cylinder are fully normal conducting during a thermal cycle so that there is no shielding from these pieces of the structure.

Figure 4.15a shows the magnetic field produced by the DC coil with the superconducting parts of the host cavity in close vicinity. The superconducting rods shield the high magnetic field region of the sample surface from the DC field, and the sample port of the host cavity concentrates the field strongly around the coil.

After accounting for all surrounding superconducting parts the magnetic field at the position of the magnetic field probe can be simulated. In the simulation the magnetic field is integrated over the volume of the field probe which is also indicated in Figure 4.15a including the measurement axis. After subtracting the residual earth magnetic field in the cryostat of 3.0 µT the fluxgate measures 312.5 µT when applying 0.7 A to the coil. In the simulation, the coil current is optimized to yield the same magnetic field and the optimizer returns 0.663 A which agrees with the experiment within about 5 %. Since the field probe is a single axis probe, the alignment of the probe, the imperfection of the coil and the contraction of the system during cooldown can account for the difference between measurement and simulation.

From the magnetic field distribution with the optimized coil current, the magnetic field on the sample surface is calculated. Figure 4.16 shows the profile of the vertical component of the magnetic field across the sample surface for 1 A coil current in the experimental setup (which corresponds to 0.947 A in the simulation). The shielding from the rods and the edges can clearly be seen. For studying the

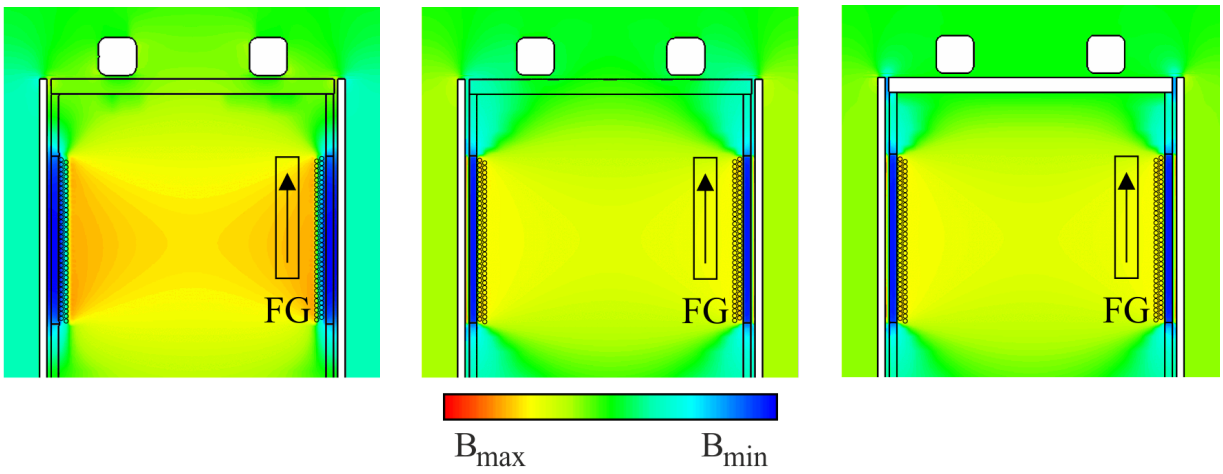

(a) (b) (c)

Figure 4.15.: Magnetic field distribution created by (a) the DC coil with the sample and support normal conducting, (b) trapped flux only in the support and (c) trapped flux in the support and the sample with perfect Meissner shielding. White regions represent objects in the Meissner state.

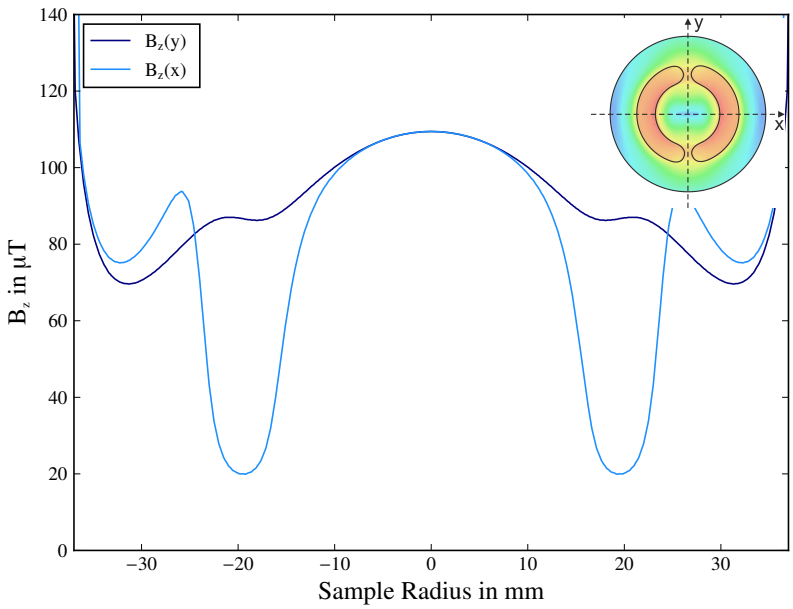

Figure 4.16.: Vertical component of the magnetic field across the sample surface produced by the DC coil with an experimental coil current of 1 A.

influence of trapped magnetic field on the SRF performance, the absolute value of the magnetic field is averaged over the high field region of the sample surface and serves as the reference for the applied field on the sample B_{app}:

$$B_{\mathrm{app}} = I_{\mathrm{coil}} \cdot 105.222 \, \frac{\mu\mathrm{T}}{\mathrm{A}}. \tag{4.20}$$

An additional set of simulations are required to clarify if it is possible to quantify the amount of trapped flux in the sample from the measurements at the position of the field probe: When the sample is cooled down in the presence of the coil field, it has to be assumed that all or almost all magnetic field that is applied to the normal conducting bulk niobium parts is trapped. To simplify the model, the region of the sample tube in close vicinity to the coil is identified with a permanent magnetization to mimic the trapped flux while the coil current is set to 0 A. The magnitude of the magnetization is set to correspond to the field previously induced by the coil at this position. The magnetic field at the fluxgate is then calculated for the case where the sample disk is in the perfect Meissner state (*perfectly electrically conducting* in CST), indicated as white areas, as shown in Figure 4.15c and for the case where the sample has trapped all applied field and does not bend or shield the ambient field as shown in Figure 4.15b. Due to the fact that the field at the sample tube is much stronger than on the sample disk, the magnetic field probe measures mainly the contribution of the trapped field in the tube. The difference in field measured at the field probe position is less than 5 % for the two cases. Considering that this is a very simplified model and that the flux trapping behaviour cannot be predicted means that the amount of trapped flux in the sample for a given field probe reading cannot be predicted at this stage.

5. SRF Performance Results

When assessing the SRF performance of a material or sample, the surface resistance as function of RF magnetic field is of particular interest. However, in order to explain the behaviour, to analyse the performance in detail and to test models, material parameters need to be known as well. Some of these parameters like the mean free path are accessible through low RF field measurements of the surface resistance and the resonance frequency shift as function of temperature. Other properties, especially those related to the materials microstructure or chemical composition need to be characterised with other techniques, using dedicated set ups which often can only host small samples in the order of mm^2. For such studies, coatings are often done with additional witness samples: small pieces of the same (sometimes also different) substrate material, with the same surface treatment which is then coated in the same chamber and the same coating run as the sample for RF testing. This ensures that the coatings are comparable. Alternatively, the sample that has been RF characterised may be cut into smaller pieces for further characterisation. This must be done with great care as any cutting has a high risk of damaging the sample, in particular coatings of µm thicknesses.

5.1. The SRF Performance of a Bulk-Like Film

This section presents the results of an extensive study on an ECR coating prepared in collaboration with JLab. Different measurement on witness samples will give additional insights regarding film microstructure and DC superconducting properties. As will be presented, the ECR coating is considered *bulk-like* with a moderate RRR. It's SRF performance will therefore be compared to the performance of a reactor grade bulk niobium sample.

The bulk niobium sample was machined from a 12 mm thick reactor grade niobium sheet, electron beam welded to the niobium cylinder of the support flange and received a bulk BCP with a total removal of about 150 µm. Prior to baking it was cold tested and showed the same SRF performance as a previously tested reactor grade bulk niobium sample which has been extensively studied elsewhere [92]. The sample then received an in-situ mild baking with the Quadrupole Resonator remaining under ultra-high vacuum (UHV). Figure 5.1 shows the temperature curve for the bake out: The temperature was ramped up within 20 min, kept constant at 112 °C for 48.5 h and then cooled down to room temperature within 3 h.

The niobium film was coated using the ECR technique outlined in Section 2.4.3. This sample is therefore also referred to as the *ECR sample*. The substrate was machined from 12 mm thick OFE copper, which is specified with an oxygen content of 0.0005 %. This copper disk was then mechanically polished to a mirror finish surface [154]. To guarantee a superconducting transition from the coating to

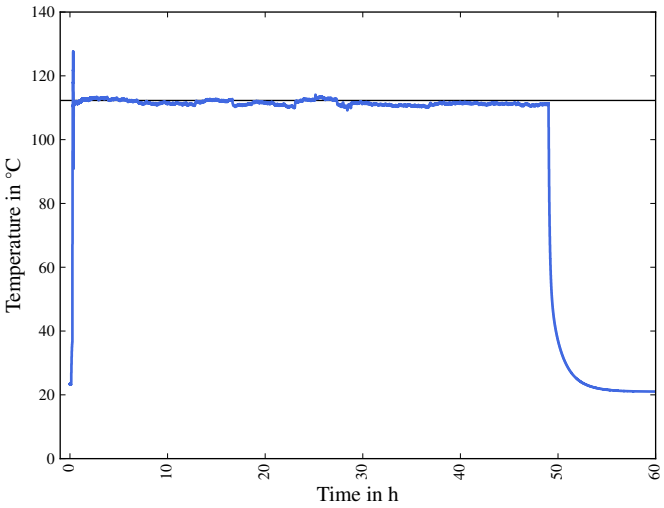

Figure 5.1.: Bake out curve for the reactor grade bulk niobium sample.

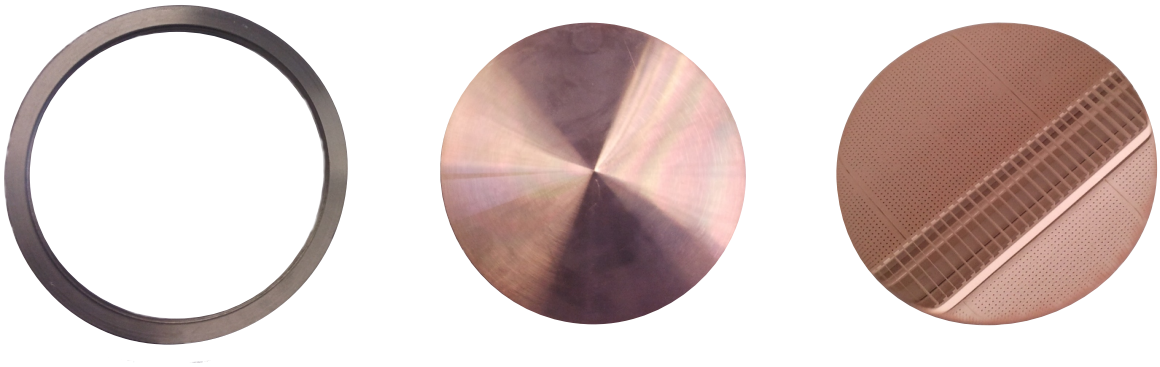

(a) (b) (c)

Figure 5.2.: Substrate of the ECR sample: (a) Niobium ring, (b) copper substrate after machining and (c) copper substrate after mechanical polishing.

the support tube, the copper disk was electron beam welded to a niobium ring as shown in Figure 5.2 as any uncoated area at the edge would compromise the RF measurements severely.

Mechanical polishing yields very smooth surfaces but destroys the crystal structure of the surface layer and holds the risk of embedding abrasive material into the surface. Therefore, about 12 µm of the surface were removed by electro-polishing.

The substrate was then rinsed with ultra pure water, dried and packed under filtered nitrogen in an ISO-5 clean room and shipped to JLab for coating. Prior to coating the substrate was baked in the vacuum chamber at 360° for 24 h to dissolve the native CuO layer into the copper bulk which provides then an epitaxial surface for the niobium coating.

The deposition was done in two steps: For the first stage of nucleation and growth of the first 100 nm, a high ion energy of 184 eV was chosen. The high coating bias provides enough energy to the arriving niobium ions to produce a dense and strong Nb/Cu interface and a good niobium template layer [155].

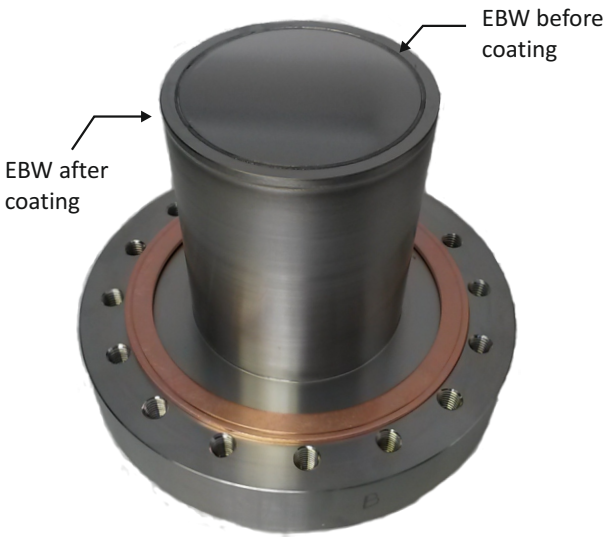

Figure 5.3.: ECR sample welded to the support cylinder.

For the subsequent growth, the ion energy was lowered to 64 eV to create a relaxed niobium layer with minimal defect density [49]. The final film thickness is about 2 µm.

After coating, the sample disk was shipped back to CERN and electron beam welded to the niobium support cylinder. Although the weld is very localized and not on the coating itself, heating of the substrate and the coating could not be fully excluded but was limited to a duration in the order of minutes. The final assembly along with the electron beam welds can be seen in Figure 5.3.

5.1.1. Nibium Film Microstructure

Techniques such as scanning electron microscopy (SEM), electron back scatter defraction (EBSD) and focussed ion beam (FIB)-SEM were used to gain a better understanding about the thin film microstructure. The results show that the ECR coating grew hetero-epitaxially on its copper substrate with a smooth, dense Nb-Cu-interface.

The grain size of the ECR coating is estimated via SEM. Figure 5.4 displays exemplarily two SEM images of the ECR coating. The (surface) grain size is estimated to be in the order of 50 µm [156] which corresponds to the typical grain size of OFE copper. It appears that the film grew hetero-epitaxially on the copper substrate, i.e. the niobium film adapts the crystal structure of the underlying substrate.

From Figure 5.4a can be seen that the film exhibits only very few large scale (> 50 µm) surface features. On average, the density of large features is estimated to be less than 1 /mm^2. In contrast to few large features, many circular features with a diameter of about 0.5 µm to 1 µm are found especially along grain boundaries (compare Figure 5.4b). These are consistent with pits from the EP and are caused by small hydrogen bubbles which stuck to the surface during electro-polishing.

The crystal structure was also studied on a Nb/Cu witness sample; coated in the same coating run on the same kind of substrate. EBSD yields the crystal structure of the film surface and is shown in

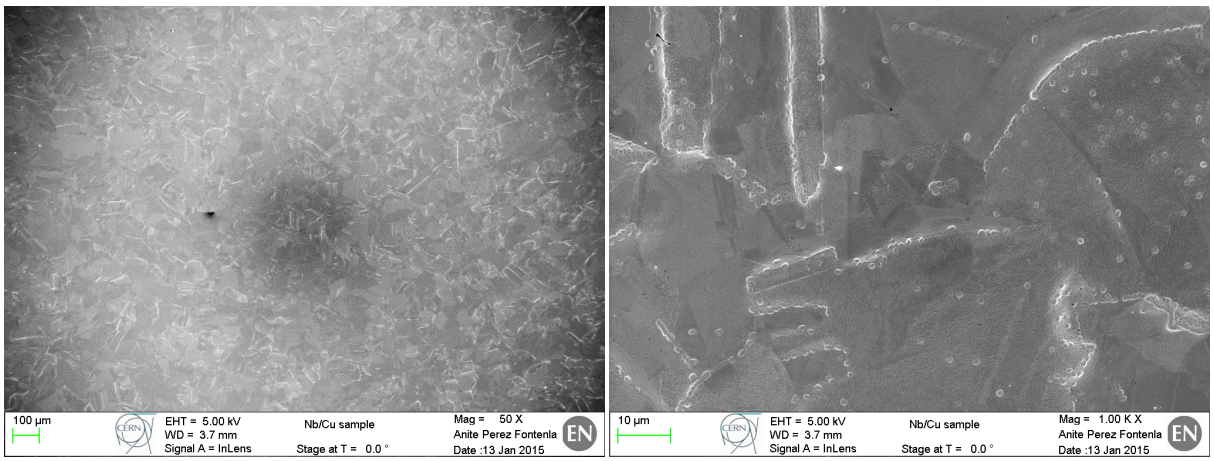

(a) (b)

Figure 5.4.: Surface SEM image of the ECR coating on different length scales. Investigation requested for this thesis; done by A. T. Perez Fontenla (CERN) [156].

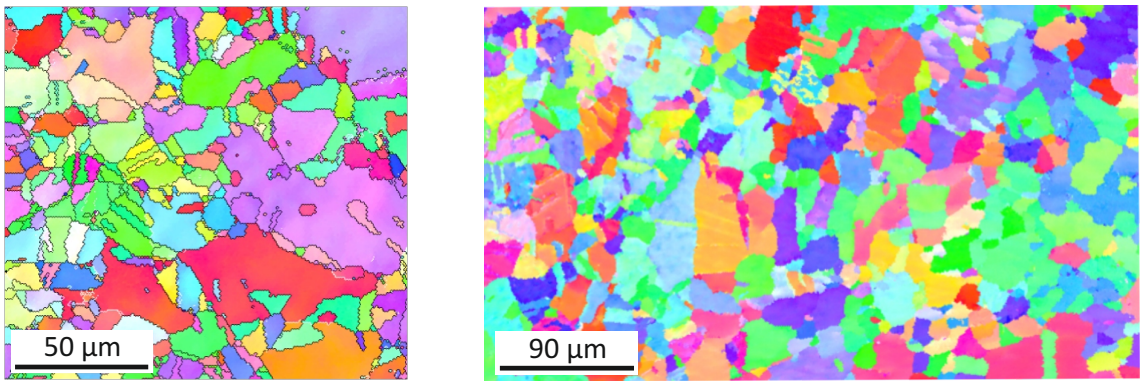

(a) (b)

Figure 5.5.: EBSD maps for (a) typical OFE copper and (b) the ECR sample. Measurements requested by A. M. Valente-Feliciano (JLab); done by R. Crooks (Black-Labs LLC).

Figure 5.5b. The film shows a grain sizes consistent with the SEM images and match a typical Cu EBSD pattern which is displayed in Figure 5.5a for comparison.

As well on a witness sample, the cross section of the coating down to the substrate was investigated. In order to obtain a clean cut through the film without damaging the coating, a small crater is cut into the sample with a FIB. To protect the surface a layer of platinum is deposited onto the region of interest. The cross section imaging is afterwards done with a SEM and two examples are displayed in Figure 5.6. Since the FIB-SEM is a time consuming and delicate technique, only a small region can be studied. The total length of the cross section is 18 µm covering two copper grain boundaries at the interface. The niobium film however does neither show any grain boundaries nor other features across the whole cross section which implies large and dense grains. The minimum visible feature size is estimated to be 10 nm. It can also be seen that the interface between niobium coating and copper substrate is very smooth and narrow. This indicates an excellent adherence and good thermal contact between the two metals. In fact, the big sample for the Quadrupole Resonator tests was exposed to a 100 bar water jet

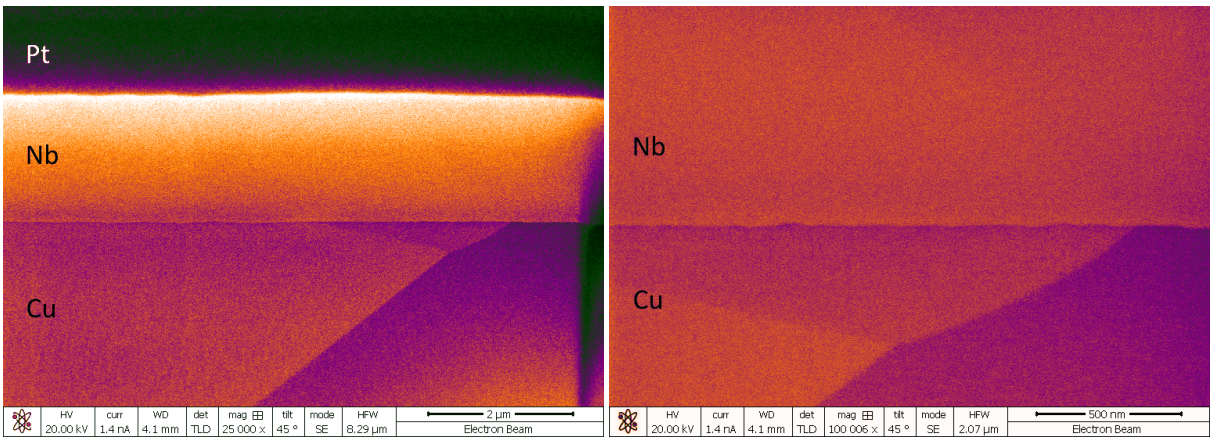

(a) (b)

Figure 5.6.: Cross-section SEM of the ECR coating cut with a focussed ion beam. Measurements requested for this thesis; done by R. Valizadeh (ASTeC).

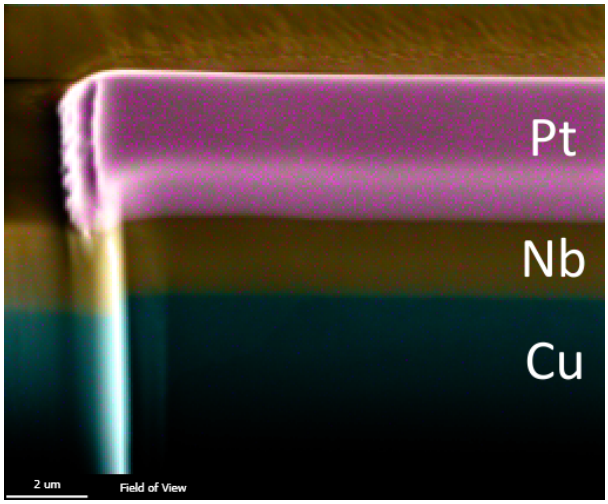

Figure 5.7.: Elemental analysis at the cross-section of the ECR coating. Measurements requested for this thesis; done by R. Valizadeh (ASTeC).

after all testing was finished. No local (or global) peel-off was visible which also proofs good adherence. Moreover, an elemental analysis of the cross section via energy-dispersive X-ray spectroscopy (EDS), shown in Figure 5.7, indicates a very clear interface and no significant diffusion of copper into the niobium coating as was already observed in other Nb/Cu coatings [157].

5.1.2. First Flux Penetration

Measuring the magnetization curve of a superconducting sample allows the derivation of the field of first magnetic flux penetration B_p, i.e. the transition from the Meissner to the Shubnikov phase, and an estimate of the upper critical field B_{c2}. As will be seen, B_p is lower for the ECR sample compared to bulk niobium, while B_{c2} is higher. This suggests weaker grain boundaries and stronger pinning compared to bulk niobium.

The field of first magnetic flux penetration of the ECR coating was measured on a witness samples at the vibrating sample magnetometer (VSM) at the University of Geneva [158]. The sample is placed in a uniform magnetic field parallel to the surface. By mechanically displacing the sample the magnetic field is changed according to Faradays law and the change can be measured by a pick up coil. In order to increase the sensitivity a Superconducting quantum interference device (SQUID) is used instead of a regular pick up coil. This is especially important for measuring the magnetic properties of a thin film sample since the film thickness of 2 µm will result in a very small signal.

Figure 5.8a shows the magnetization curve for the ECR witness sample at 2 K. Due to the fact that the niobium film is deposited on a metallic substrate, it has to be ensured that the effect of eddy currents in the substrate can be neglected. To do so, the magnetization was measured with different field ramps between 0.2 mT/s and 20 mT/s which lead to the same results and indicates that eddy current do not contribute to the signal. Starting at the origin of the curve, i.e. where magnetic moment and applied field are 0, the field of first flux penetration B_p is the point where measurements points deviate from the linear trend and is estimated to

$$B_\mathrm{p} = (51.5 \pm 1.0)\,\mathrm{mT}. \tag{5.1}$$

In order to verify the derived field of first flux penetration, two magnetic sweeps were performed: First, the magnetic field was increased from 0 mT to 45 mT, lowered to −45 mT and returned to 0 mT. As can be seen in Figure 5.8b, there is no change in magnetisation after reaching maximum field strength, hence, no hysteresis. The sample remains in the Meissner state up to this field. Secondly, the sweep was repeated in the same way, but this time up to ±55 mT. In contrast to the sweep up to 45 mT a hysteresis loop is observed which can be seen in Figure 5.8b. This suggests flux penetration and pinning and supports the level of estimated first flux penetration.

The upper critical field B_{c2} can be identified in Figure 5.8a as the field where the magnetization moment becomes 0 again, i.e. the sample becomes normal conducting. A linear fit yields

$$B_{c2} = (635 \pm 16)\,\mathrm{mT} \tag{5.2}$$

which is significantly higher than measurements bulk niobium in the order of 280 mT but typical for niobium films which is explained by stronger pinning [35, 159]. In contrast, the field of first flux penetration is lower for the ECR film that for bulk niobium. Measurement on high RRR found values ranging from 90 mT to 160 mT depending on the treatment history [159]. The earlier flux penetration is consistent with grains that are not as well connected as in the bulk material. Alternatively, the flux could be entering through the edge of the sample or even the back of it since the sample is placed inside the magnetic field. This would not be the case in an SRF cavity where the superconducting film is a closed surface and the RF magnetic field in only applied on the inside respectively the coated side of the cavity. The magnetization measurement on this sample has been repeated in other institutions yielding consistent results [160]. Hence, a misalignment or a systematic error in the set-ups can be ruled out.

It is worth mentioning here that the RF measurements at 400 MHz were limited to about 50 mT although the Quadrupole Resonator in principle allows measurements up to 60 mT. However, above

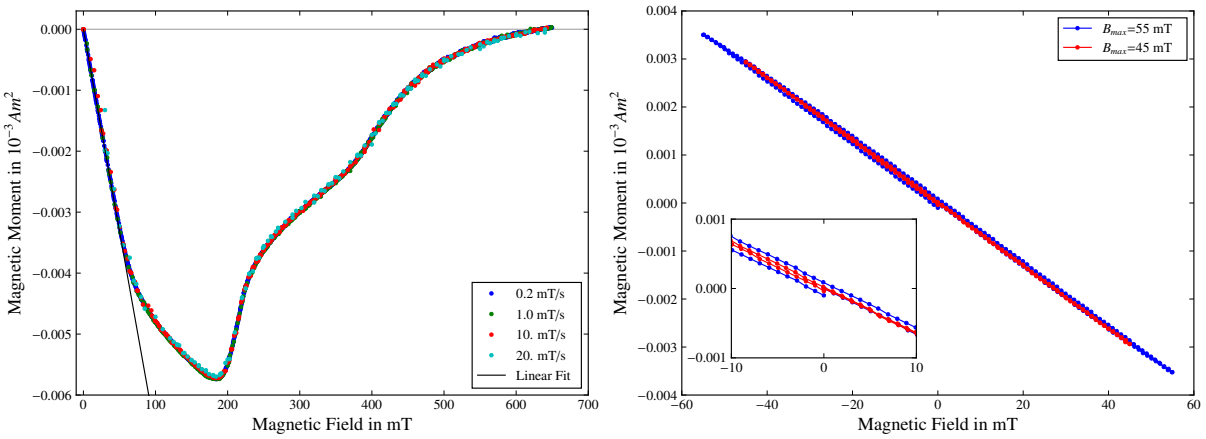

(a) Magnetization curve for the ECR sample with the DC field applied parallel to the surface. The end of the Meissner phase is indicated by the deviation from the linear trend at low field.

(b) Magnetic field sweep up to just below and above the threshold for first flux entry shows a pure Meissner phase respectively flux penetration and pinning.

Figure 5.8.: Magnetization measurements of the ECR sample. Measurements requested for this thesis; done by M. Bonura (University of Geneva).

50 mT the RF signal became very unstable and prohibited further measurements. On the basis of the magnetization measurements, one could speculate that (at least) in this case RF and DC field of first flux penetration coincide and that flux penetration caused the RF field limitation.

5.1.3. The Low Field Properties

The penetration depth as well as low field, low temperature behaviour of the surface resistance are dominated by material parameters which in turn depend on the microstructure and contamination including oxidation. As will be presented in this section, the ECR coating exhibits a mean free path and superconducting gap comparable to the reactor grade bulk niobium reference, but higher residual resistance R_{res} and stronger increase of R_{res} with frequency. However, only the ECR coatings BCS parameter A_{BCS} follows the quadratic increase with frequency, indicating no significant other low field loss mechanisms. The data on the bulk niobium sample suggests normal conducting contaminants, most likely due to the presence of Nb-oxides and Nb-hydrides.

The penetration depth is derived from measuring the resonance frequency shift as function of temperature as outlined in Section 4.1.2. The shift in penetration depth for the ECR coating and the bulk Nb sample before and after mild baking are displayed in Figure 5.9. It can be seen that all three data sets follow the $1/\sqrt{1-t^4}$ dependence with the reduced temperature $t = T/T_{\mathrm{c}}$. The slopes of the ECR coating and the bulk niobium sample before baking are very similar, while the the slope of the bulk niobium sample after baking is significantly steeper. A linear fit of the slopes yields the (effective) penetration depth at 0 K, λ_0, from which the mean free path, ℓ, and the RRR can be derived according to Equation 3.37 and 3.41. The resulting values along with the critical temperature, T_{c}, for the ECR coating and the bulk Nb sample are listed in Table 5.1. The penetration depth of the ECR coating is

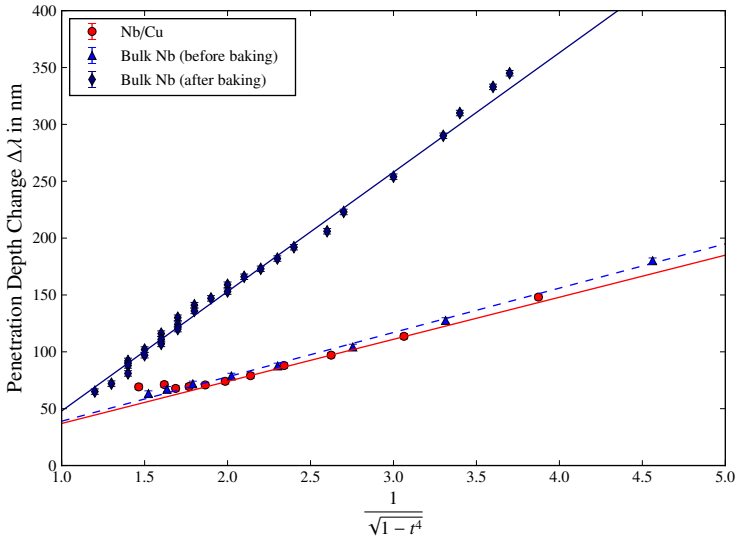

Figure 5.9.: Measurements of the penetration depth as function of temperature for the niobium film and a reactor grade bulk niobium sample.

Table 5.1.: Material parameters derived from the penetration depth.

	λ_0 in nm	ℓ in nm	RRR	T_c in K
Niobium film	37 ± 2	182 ± 24	67 ± 9	9.36 ± 0.01
Bulk niobium before baking	39 ± 2	126 ± 18	47 ± 7	8.99 ± 0.03
Bulk niobium after baking	90 ± 1	8.9 ± 0.3	3.3 ± 0.1	9.12 ± 0.05

slightly lower as the one of the bulk Nb before baking although the values are overlapping within their error interval. The smaller penetration depth corresponds to a longer mean free path and a higher RRR. A significantly larger penetration depth and corresponding shorter mean free path for the baked bulk niobium is typical for mild baking [161, 162].

The fact that the grain size, penetration depth and mean free path of the ECR sample are comparable to the reactor grade bulk niobium sample before baking allows the ECR coating to be considered as *bulk-like*.

Measuring the surface resistance R_S as function of temperature allows the derivation of the residual resistance R_{res}, the BCS factor A_{BCS} that depends on frequency and material parameters and the superconducting gap Δ/k_B where k_B is the Boltzmann constant. All curves are taken at low RF field, approximately 10 mT, to allow neglecting the field dependence of the surface resistance. Only exception is here the 1.2 GHz curve of the Nb coating which locally quenched at a RF field as low as 2 mT. The $R_S(T)$ curve was hence performed at 1 mT.

For temperatures below $T_c/2$ the data can be fitted according to Equation 3.4. Like in the previous Section the fit is performed with Δ/k_B as a common fit parameter for all frequencies. It was derived by calculating the weighted average of each curve (per data set) so that the $R_S(T)$ reduces to a two parameter fit afterwards. Figure 5.10 displays the $R_S(T)$ curves of both samples for three frequencies with the final fit results.

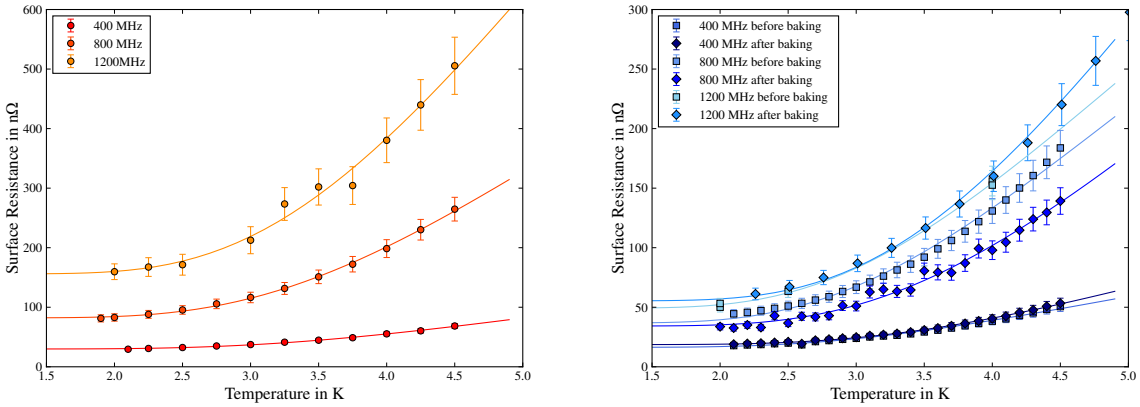

(a) (b)

Figure 5.10.: Surface resistance of (a) the Nb film and (b) the bulk Nb sample as function of temperature at 400 MHz, 800 MHz and 1200 MHz.

Table 5.2.: Superconducting material parameters derived from the $R_S(T)$ curves.

Frequency	Nb Film		Bulk Nb before baking		Bulk Nb after baking	
	R_{res} in nΩ	Δ'	R_{res} in nΩ	Δ'	R_{res} in nΩ	Δ'
400 MHz	29.9 ± 0.2		16.3 ± 0.3		18.6 ± 0.2	
800 MHz	82.2 ± 0.9	2.02 ± 0.03	36.8 ± 1.2	1.94 ± 0.22	34.2 ± 1.1	2.19 ± 0.14
1200 MHz	156 ± 7		49.3 ± 1.3		55.4 ± 1.9	

With the critical temperature from the penetration depth measurement the reduced superconducting energy gap $\Delta' = \Delta/k_B T_c$ can be derived. The residual resistances and the reduced gap values are listed in Table 5.2. The gap measurement of the Nb film is consistent with other Nb/Cu measurements: $R_S(T)$ measurements on 1.5 GHz dcms coated cavities find a superconducting gap of $\Delta' = 1.98 \pm 0.05$ averaged over 14 coatings [13]. The same publication finds an average $\Delta' = 2.02 \pm 0.03$ for five bulk Nb cavities made from RRR 300. The slightly smaller superconducting gap of the Nb coating is due to the higher critical temperature. A critical temperature above 9.3 K is commonly observed in niobium films and is attributed to stress in the crystal lattice due to the different lattice parameters of copper (3.6 Å) and niobium (3.3 Å). The bulk niobium sample shows typical values before and after baking.

The individual fit parameters for the BCS factor A_{BCS} and the residual resistance R_{res} are plotted in Figure 5.11.

A_{BCS} should theoretically increase quadratically with frequency, but has often been reported to increase with $f^{1.7-2}$. The following frequency scalings were found:

$$A_{BCS,film} \sim f^{1.8\pm0.3} \quad \text{for the ECR coating,} \tag{5.3}$$

$$A_{BCS,bulk,bb} \sim f^{1.0\pm0.6} \quad \text{for the bulk sample before mild baking and} \tag{5.4}$$

$$A_{BCS,bulk,ab} \sim f^{1.3\pm0.1} \quad \text{for the bulk sample after mild baking.} \tag{5.5}$$

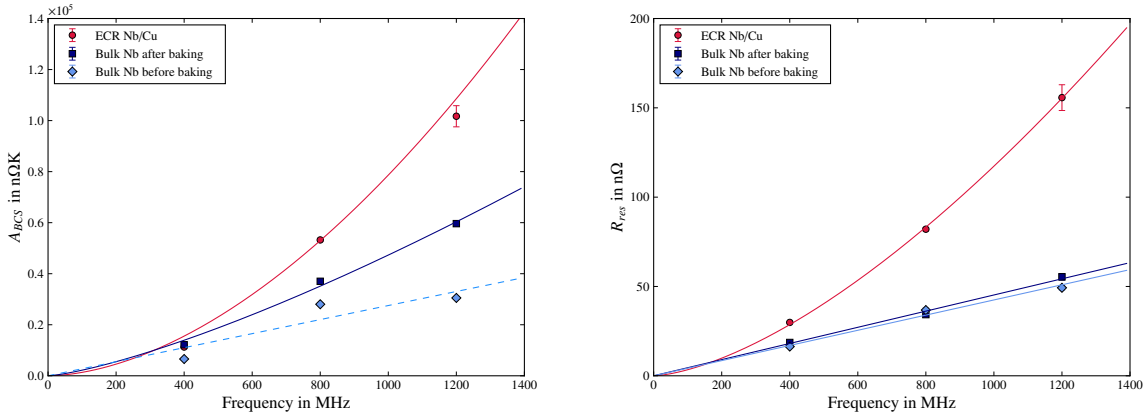

(a) (b)

Figure 5.11.: Increase of (a) the BCS factor A_{BCS} and (b) the residual resistance with frequency.

The scaling with $f^{1.8\pm0.3}$ for the Nb/Cu sample agrees well with expectations ($A_{\mathrm{BCS}} \sim f^2$) while the bulk niobium sample scales only with $f^{1.0\pm0.6}$ before and $f^{1.3\pm0.3}$ after baking. This suggests normal conducting regions within the surface which scale according to the skin effect with $\sqrt{f}$ and which in turn suppress the quadratic dependence. As can be seen from Figure 5.11a, the BCS factor is the highest for the ECR coating and the lower for the baked bulk niobium sample. A increasing BCS factor is consistent with increasing purity, i.e. longer mean free path which has already been found in the penetration depth measurement.

The frequency dependence of the residual resistance depends on the dominant loss mechanism. By analysing a large data set of cavity measurements, a quadratic frequency dependence of residual resistance was already found for high quality bulk niobium [91] with an increase of $(1.9 \pm 0.6)\,\mathrm{n\Omega/GHz^2}$. For the samples under study here, we find the residual resistance to increase with $f^{1.54}$ for the Nb/Cu sample and only linearly for the bulk Nb sample:

$$R_{\mathrm{res,film}} = (2.8 \pm 0.8)\,10^{-3}\mathrm{n\Omega} \cdot (f[\mathrm{MHz}])^{1.54\pm0.04} \quad \text{for the ECR coating,} \tag{5.6}$$

$$R_{\mathrm{res,bulk,bb}} = (4.2 \pm 0.1)\,10^{-2}\mathrm{n\Omega} \cdot f[\mathrm{MHz}] \quad \text{for the bulk sample before mild baking and} \tag{5.7}$$

$$R_{\mathrm{res,bulk,ab}} = (4.5 \pm 0.1)\,10^{-2}\mathrm{n\Omega} \cdot f[\mathrm{MHz}] \quad \text{for the bulk sample after mild baking.} \tag{5.8}$$

Despite the lower frequency scaling, the increase of R_{res} with frequency is much stronger than the reported quadratic increase in Reference [91] for all cases.

Comparing the reactor grade bulk niobium data before and after mild baking, it was found that the baking shortened the mean free path and increased the superconducting gap, the critical temperature and the residual resistance. This is consistent with measurements on high grade niobium cavities and is explained by transformation of the surface oxides from Nb_2O_5 to NbO_2 and NbO and a reduction of the oxide layer thickness [163, 164]. Moreover, it was found that the mild baking mitigates the formation of lossy nanohydrides [108].

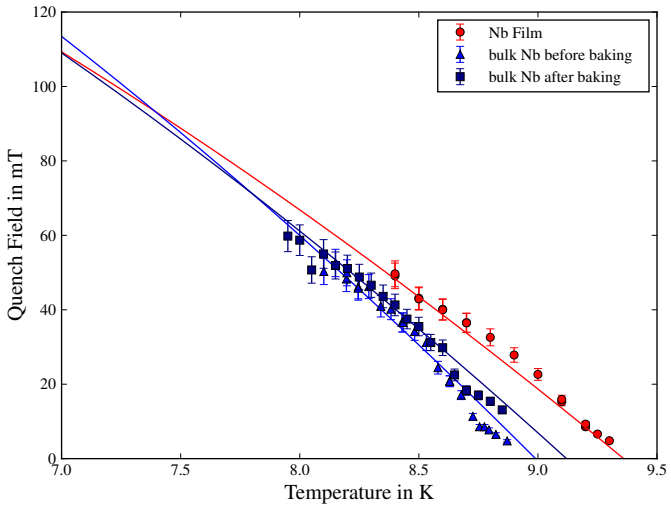

Figure 5.12.: Quench field of the ECR coating and the bulk Nb sample as function of temperature.

5.1.4. The Quench Field

Measuring the quench field of a given sample and comparing it to relevant models allows a determination of the mechanism causing the break down. As will be discussed in the following, the ECR sample breaks down at a field consistent with the superheating field. This supports that the field limit for Nb/Cu films is also the superheating field - if the quality is high enough.

The Quadrupole Resonator allows an estimation of the quench field of the sample under investigation. For this, the Quadrupole Resonator is excited with high power pulses at low duty cycle ($\leq 10\,\%$) to suppress quenching due to a thermal runaway. When the onset slope of the power pulse reaches the quench field of the sample the transmitted power breaks down as sketched in Figure 4.6. As the magnetic field of the Quadrupole Resonator rods is higher as on the sample, a sample temperature has to be chosen where the quench field of the sample at the given temperature is lower than quench field of the Quadrupole Resonator at the bath temperature. Due to the field limitation of the Quadrupole Resonator, the quench field of the sample can only be measured at temperatures above 8 K.

Figure 5.12 shows the quench field for both samples as function of temperature. As all critical fields of superconductivity scale with $1 - t^2$ with the reduced temperature $t = T/T_c$, the same temperature dependence is assumed and the data can be linearly fitted versus $1 - t^2$. The slope can then be identified with the quench field at 0 K.

Following Section 3.3.1, the Ginsburg-Landau parameter has been calculated from the results of the penetration depth measurement according to Equation 3.38:

$$\kappa(0\,\mathrm{K}, \ell) = \frac{2\sqrt{3}}{\pi} \frac{\lambda_L \left(1 + \frac{\pi\xi_0}{2\ell}\right)}{\xi_0} \tag{5.9}$$

On this basis, the theoretical critical fields and the superheating field according to the different approximations can be calculated and compared to the measured quench fields. Table 5.3 lists the measured

Table 5.3.: Extrapolated quench field for both samples compared to the superheating field predictions according to different approximations. The Ginsburg-Landau parameter κ was derived from the penetration depth measurement. All fields apply to 0 K.

	Bulk Nb before baking	Bulk Nb after baking	ECR Coating	Equation
GL parameter κ	1.34 ± 0.06	7.1 ± 0.2	1.21 ± 0.04	5.9
Measured B_{quench} in mT	288 ± 5	265 ± 9	248 ± 5	
Calculated B_c in mT	206	206	206	3.44
Calculated $B_{c1,\kappa<20}$ in mT	140	50	149	3.48
Calculated B_{c2} in mT	389	2048	352	3.46
Calculated $B_{sh,\kappa\approx1}$ in mT	265	265	265	3.51
Calculated $B_{sh,Transtrum}$ in mT	250	195	255	3.55
Calculated $B_{sh,MSJ}$ in mT	253	194	257	3.52
Calculated B_{VLNM} in mT	153	29	170	3.58

quench fields B_{quench} and the calculated critical and superheating fields of the ECR coating and the bulk niobium sample before and after baking.

The unbaked bulk niobium sample quenches at a field consistent with the predictions for the superheating within about 15 %. All models for the superheating field for low κ values find similar values for the bulk niobium sample before baking. The critical fields and the vortex line nucleation model find values which are very different from the measured values so that the quench field can be identified with the superheating field.

The baked bulk niobium sample has a κ value much bigger than 1 due to the short mean free path. This results in a suppression of the theoretical lower critical, superheating and vortex nucleation field and an increase in upper critical field. The measured quench field however is about 14 % lower than what has been measured before baking. This can be explained by the fact that the mild baking acts only the surface layer of the niobium and leaves the bulk properties unchanged [14, 165]. From the measurements imply that if the surface layer with low RRR and low quench field becomes normal conducting, the bulk niobium underneath which has not been affected by the baking remains superconducting and quenches when reaching the superheating field. The superposition results in quench field lower, but close the superheating field of the sample before baking.

The quench field of the ECR coating agrees well with the predictions for the superheating field and not with any other critical field or the vortex line nucleation field. This suggests that the ultimate field limitation for niobium coatings is also the superheating field if the quality of the film is high enough. The superheating field can then be predicted in the same way as for bulk Nb but requires taking into account the Ginsburg-Landau parameter κ for an accurate prediction.

5.1.5. RF Field Dependence

This section presents the dependence of the surface resistance on the RF magnetic field. As will be discussed, the 120 °C baked reactor grade bulk niobium behaved atypical for (clean) bulk niobium and

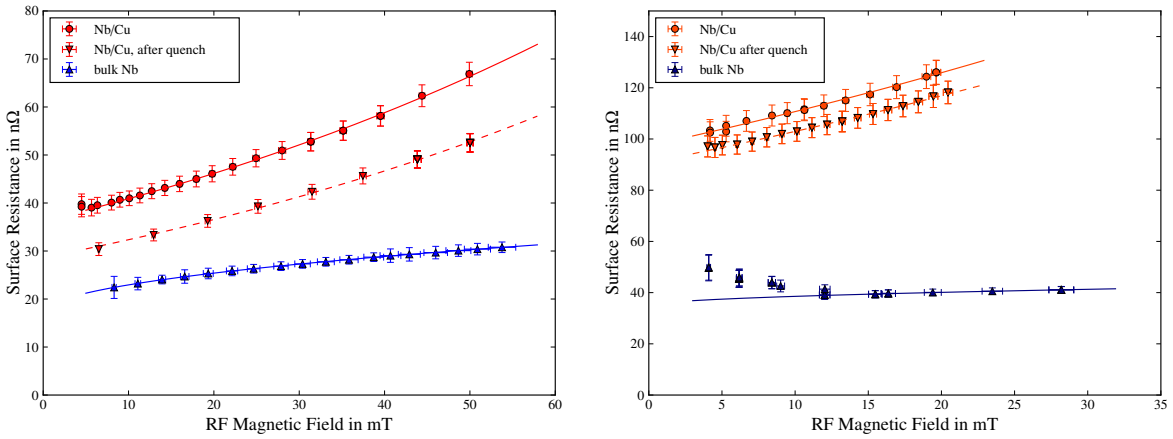

(a) (b)

Figure 5.13.: Comparison of the surface resistance of the bulk and the film sample as function of RF magnetic field at 2.5 K for (a) 400 MHz and (b) 800 MHz.

suggests strong oxidation of the surface. The ECR sample was found to follow the Nb/Cu-typical exponential increase with field but -as will be discussed in Section 5.1.7 - significantly flatter than all other Nb/Cu coatings to-date. In comparison with the reactor grade Nb sample, the ECR samples Q-slope is still worse. The ECR data before and after quench already suggests that cooling conditions have an impact on the surface resistance. This will be further explored in Section 5.1.8 and 5.1.9. Finally, the finding that the Nb/Cu Q-slope is worse for lower temperature cannot be explained by the temperature dependence of the superconducting parameters. The Kapitza resistance at the Nb-Cu interface could give a qualitative explanation and motivates the application of the thermal boundary resistance model at the end of this section. This analysis supports a well attached Nb/Cu film and supports the validity of this model to explain the Q-slope in Nb/Cu in general.

The RF performance of reactor grade bulk niobium has been extensively studied in the past [92] and shall not be reproduced in this work. Therefore, only the bulk niobium data after mild baking will be subject to comparing the RF performance of the bulk sample with the ECR coating and the unbaked data will only be considered for additional discussions on the trapped flux behaviour in Section 5.2.

While the low RF power measurements allow insights regarding the material parameters, it is the behaviour under moderate and high magnetic fields that defines the RF performance of a superconductor. As outlined in Section 4.1, RF fields up to 60 mT at 400 MHz and 30 mT at 800 MHz can be reached on the sample surface due to the quench fields of the QPR host cavity. In a TESLA cavity this would correspond to a maximum accelerating gradient of 14 MV/m at 400 MHz respectively 7 MV/m at 800 MHz [6].

At 1.2 GHz, the ECR coating locally quenched at a low RF field of 2 mT above which the surface resistance increased from 200 nΩ to 20 μΩ. Therefore, the R_S (B_{RF}) data was discarded and the discussions are restricted to the behaviour at 400 MHz and 800 MHz.

Figure 5.13 shows the performance of the bulk niobium sample at 2.5 K for 400 MHz (5.13a) and

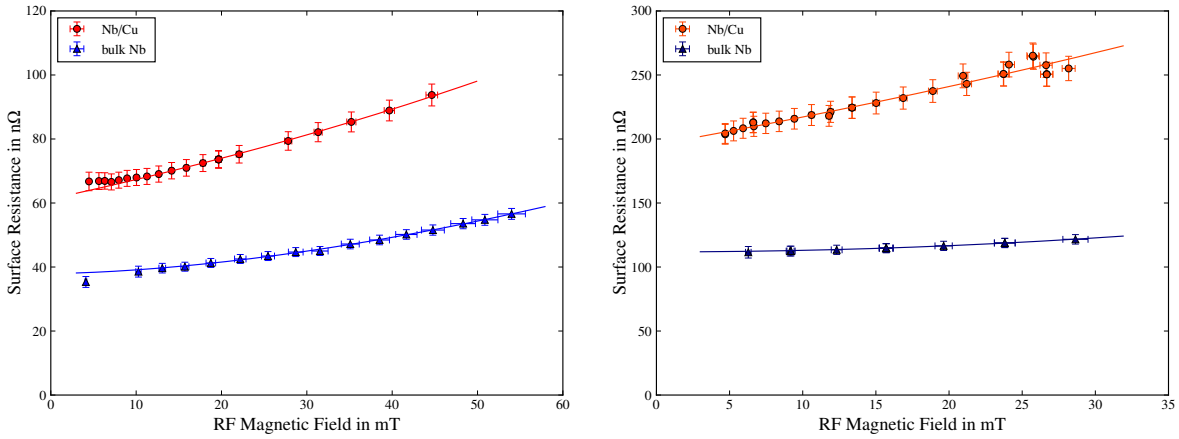

(a) (b)

Figure 5.14.: Comparison of the surface resistance of the bulk and the film sample as function of RF magnetic field at 4.0 K for (a) 400 MHz and (b) 800 MHz.

800 MHz (5.13b). For RF fields above 10 mT, the surface resistance increases with $\sqrt{B}$. This is a weaker dependence than the typical linear or quadratic behaviour but has been found previously in cold worked, low RRR bulk niobium at low frequencies up to 500 MHz [166]. Cold worked niobium is characterized by strong oxidation and a network of weak links reaching several micrometers into the surface. The corresponding losses scale with $\sqrt{B}$ which can be explained by the decrease of critical current with field for oxidation deep into the surface [93].

Fitting the 2.5 K data with $R_S = m_1 \sqrt{B} + m_2$ yields essentially the residual resistances for m_2 (with deviations less than 1 nΩ) and

$$m_1\,(400\,\mathrm{MHz}) = (1.872 \pm 0.008)\,\mathrm{mT}^{-1/2} \quad \text{for the 400 MHz curve and} \tag{5.10}$$

$$m_1\,(800\,\mathrm{MHz}) = (1.19 \pm 0.05)\,\mathrm{mT}^{-1/2} \quad \text{for the 800 MHz curve.} \tag{5.11}$$

As discussed in Reference [93], the hysteresis losses scale linearly in frequency but depend also on the depinning behaviour which has been discussed in Section 3.2.2. Both fit parameters should present this frequency dependence, but while the residual resistance matches the linear trend as shown in Figure 5.11b, the parameter m_1 even decreases with frequency instead of increasing. This indicates a change in pinning behaviour, represented by the factor $g(\omega) = 1/\left[1 + (\omega/\omega_0)^2\right]^{3/2}$ in Reference [93], and suggests a depinning frequency ω_0 in the order of a few hundred MHz. If the depinning frequency is in the same order as the measurement frequencies, $g(\omega)$ can decrease for higher frequencies, partly compensating the underlying linear increase of the surface resistance with frequency.

At 4.0 K the surface resistance of the bulk niobium sample increases stronger with field than at 2.5 K as shown in Figure 5.14. The field dependence is stronger than linear but weaker than quadratic. Fitting the data yields

Table 5.4.: Fit parameters for the exponential fit of the $R_S(B_{RF})$ data of the ECR sample.

Frequency in MHz	Temperature in K	R_0 in nΩ	b in 10^{-2}/mT
400	2.5	36.2 ± 0.1	1.21 ± 0.01
	2.5 (after quench)	28.6 ± 0.2	1.22 ± 0.01
800	2.5	97.3 ± 0.5	1.29 ± 0.04
	2.5 (after quench)	90.7 ± 0.3	1.26 ± 0.02
400	4.0	61.3 ± 0.1	0.94 ± 0.01
800	4.0	195.7 ± 2.8	1.04 ± 0.04

$$R_S\,(400\,\mathrm{MHz}, 4\,\mathrm{K}, B_{RF}) = \left[(3.4 \pm 0.9)\,10^{-2} \cdot B_{RF}^{(1.58\pm0.07)} + (37.50 \pm 0.07)\right]\mathrm{n\Omega} \quad \text{respectively} \tag{5.12}$$

$$R_S\,(800\,\mathrm{MHz}, 4\,\mathrm{K}, B_{RF}) = \left[(4.3 \pm 0.5)\,10^{-2} \cdot B_{RF}^{(1.65\pm0.03)} + (110.72 \pm 0.09)\right]\mathrm{n\Omega} \tag{5.13}$$

and suggests additional losses on top of the hysteresis losses which are dominating at 2.5 K. According to Reference [93] magnetic flux penetration through weak links cause losses scaling with f^2 and also depend on temperature: $R_{WL}\,(T, B_{RF}) \sim R_{WL}\,(T, 0) \cdot B_{RF}^2$. The superposition of the two loss mechanisms may explain the increase of surface resistance with $B_{RF}^{1.6}$. The fact that the field related fit parameters overlap within their uncertainties shows that the increase of surface resistance does not exhibit any significant frequency dependence. This might be again the result of superposing a change in pinning behaviour as discussed for the 2.5 K case and the expected f^2 scaling from the weak link model.

The performance of the ECR Nb/Cu film is directly compared to the bulk niobium sample in Figures 5.13 and 5.14. Typical for Nb/Cu films, the surface resistance increases exponentially with RF field for all frequency-temperature combinations and the data can be fitted via

$$R_{S,film}\,(B_{RF}) = R_0 \exp\,(b \cdot B_{RF}) \tag{5.14}$$

where R_0 comprises the low field BCS and residual part of the surface resistance and b characterises the field dependence. b is therefore also referred to as the Q-slope parameter.

The measurement at 800 MHz and 4.0 K had a thermal runaway which lead to a sample quench. Afterwards the residual resistance was found to be significantly lower than before which further discussed in Section 5.1.8. Due to the high BCS contribution at 4 K, the change is negligible and is not shown but the improvement at 2.5 K is sufficiently prominent and therefore plotted in Figure 5.13. Table 5.4 summarizes all resulting fit parameters for the data shown in Figures 5.13 and 5.14. A comparison of the exponential parameter b indicates that this Q-slope parameter is not only insensitive to the cooling dynamics (before/after quench) but also does not depend on frequency. However, as the total surface resistance is a product of frequency dependent BCS contribution and the exponential field dependence, the slope will appear stronger for higher frequencies (at a given temperature).

Figure 5.15 displays the weighted average values for both temperatures. As can be seen, independently of the BCS contribution (given by R_0), the slope appears to be worse for lower temperatures. The temperature dependence of the superconducting (DC) properties can not explain this: The penetration

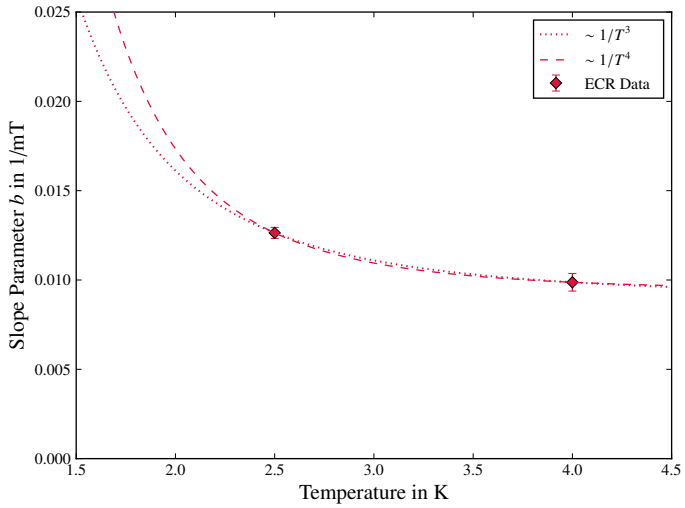

Figure 5.15.: Slope parameter b as function of temperature and typical temperature dependencies for the Kapitza resistance.

depth λ as the characteristic length for the shielding currents becomes smaller for lower temperature. Probing a thinner surface layer with the RF is expected to result in lower losses. The coherence length ξ is the characteristic size of the normal conducting core of a (trapped) flux line in the superconductor. ξ increases with temperature and should as well result in lower losses for lower temperature. The superconducting gap and all critical fields decrease with temperature and should also decrease the performance for higher temperatures. Moreover, all properties mentioned above change only marginally between 2.5 K and 4.0 K.

Since the superconducting properties cannot qualitatively explain why the slope parameter increases with decreasing temperature, thermal effects might be considered. As discussed in Section 4.1, the sample is thermally decoupled from the hosting Quadrupole Resonator. A change in sample temperature does not affect the host cavity and the latter remains at the temperature of the superfluid helium bath. In terms of heat transfer this means that the Kapitza resistance of the QPR-Helium interface and therefore the cooling power is always the same – independently of the sample's temperature.

All considered, the Kapitza resistance at the niobium-copper interface remains a candidate to qualitatively explain a stronger slope at lower temperatures. At cryogenic temperatures, the Kapitza resistance of metal-metal interfaces was found to scale with T^{-3} to T^{-5}[167, 168, 169]. The higher the thermal contact resistance, the higher the surface resistance respectively the stronger the slope so that $b = f(T^{-n})$ is proposed.

The most common dependencies, T^{-3} and T^{-4}, are indicated in Figure 5.15. They suggest that the slope does not change significantly between 4.0 K and 4.5 K which facilitates comparing data, but significant changes can be expected between 1.7 K and 2.1 K as long as the exact temperature dependence is not clear. In any case, it can be concluded that the thermal contact resistance shall not be neglected when studying losses in Nb/Cu cavities. In this context, not only the heat transfer between film and substrate has to be taken into account but also defects at the interface locally prohibiting the heat transfer need to be considered. This will be discussed in the Section 5.1.6.

A general comparison between the bulk Nb and the Nb/Cu sample shows that the increase of the surface resistance with RF field of the niobium film is still stronger than for the bulk niobium. A comparison with other Nb/Cu coatings is subject to Section 3.2.1. Calculating the surface resistances at 10 mT and 45 mT which corresponds roughly to 2 MV/m to 10 MV/m for the TESLA geometry yields a twice as strong increase for the ECR film at 400 MHz and 4 K compared to the bulk niobium sample. This factor increases slightly for lower temperature (2.7 for 2.5 K) and significantly when comparing the 800 MHz data (factor 4 for 4 K and a factor of 13 for 2.5 K). One reason though is the high residual resistance, especially at 800 MHz which couples directly with the slope.

Future measurements need to show if the slope parameter can be sustained for lower residual resistance values as this will directly result in a flatter overall slope. However, magnetron sputtered cavities often showed a steeper slope for lower residual resistance [170, 171]. Since this observation has not been explained yet, it is unclear if the same behaviour has to be expected in energetically condensed Nb/Cu films.

5.1.6. Thermal Boundary Resistance

The recently proposed thermal boundary resistance model which is summarised in Section 3.2.1 allows quantifying the quality of a given film as it yields the fraction of surface that is not well attached to the surface and a distribution function that can be compared to other coatings. The weakness of the model is that a solution can be found for any set of data points without any physical meaning. The data sets taken with the Quadrupole Resonator are ideal to test the model for consistency: Applying the model to any $R_S(B_{RF})$ curve of the niobium coating should result in the same distribution function for all frequencies and temperatures. If the model is applied to $R_S(B_{RF})$ curves at different frequencies and/or temperatures of the bulk niobium sample, the results should not agree with each other.

To test the model, the fit of the surface resistance as function of temperature has to be modified. The function 3.4 can only serve as a fit function for a temperature range up to $T_c/2$. Since the thermal runaway of a microscopic hot spot shall be modeled, the fit function is extended to account for the temperature dependence of the superconducting gap:

$$R_S(T) = \frac{A\omega^2}{T} \cdot \exp -\frac{\Delta_0}{k_B T} \sqrt{\cos\left(\frac{\pi}{2}\left(\frac{T}{T_c}\right)^2\right)} + R_{res} \tag{5.15}$$

The $R_s(T)$ data sets for the ECR coating and the bulk niobium sample are fitted with Equation 5.15 while having a common superconducting gap for all frequencies.

From measuring the Q of the Quadrupole Resonator with a quenched sample as outlined in Section 4.1.3, the normal conducting surface resistance R_{nc} just above T_c can be derived for the different frequencies. These values as well as the fit parameters from the $R_s(T)$ fit are used as input parameters for the thermal boundary model and are listed in Table 5.5 and Table 5.6.

Subsequently, the quench field for a given thermal boundary resistance R_B can be calculated as discribed in Section 3.2.1. The resulting functions are plotted in Figure 5.16 and show similar behaviour for the bulk and the film sample. Due to the higher dissipation at higher temperatures and higher frequency, the quench field is lower for 800 MHz than for 400 MHz and lower for 4.0 K than for 2.5 K.

Table 5.5.: Input parameters for the thermal boundary resistance fit on the ECR Nb/Cu data. All parameters were derived from RF measurements with the Quadrupole Resonator.

f_{res}	$A\omega^2$	Δ_0/k_B	R_{res}	R_{nc}
400 MHz	0.953×10^{-5} Ω/K	18.09 K	29.4 nΩ	0.9 mΩ
800 MHz	4.488×10^{-5} Ω/K		80.2 nΩ	1.5 mΩ

Table 5.6.: Input parameters for the thermal boundary resistance fit on the bulk Nb data. All parameters were derived from RF measurements with the Quadrupole Resonator.

f_{res}	$A\omega^2$	Δ_0/k_B	R_{res}	R_{nc}
400 MHz	1.101×10^{-5} Ω/K	19.23 K	18.74 nΩ	2.0 mΩ
800 MHz	3.351×10^{-5} Ω/K		31.49 nΩ	2.8 mΩ

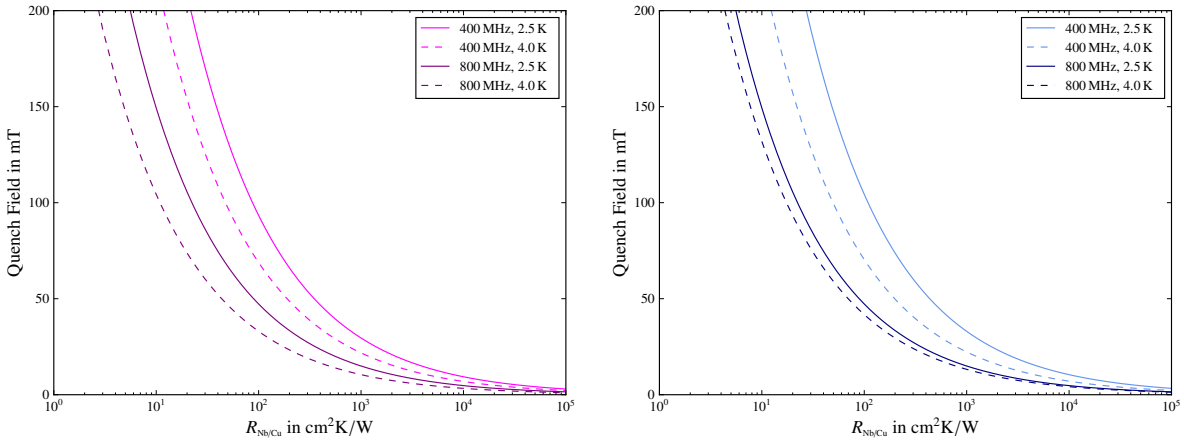

(a) (b)

Figure 5.16.: Quench Field as Function of Thermal Boundary Resistance for (a) the ECR niobium film on copper and (b) for bulk niobium.

Table 5.7.: Fraction of film surface that is detached from the substrate according to Equation 5.16.

	f_{res}	T	Fraction of detached film
ECR Nb/Cu	400 MHz	2.5 K	3.3×10^{-5}
		4.0 K	3.1×10^{-5}
	800 MHz	2.5 K	1.6×10^{-5}
		4.0 K	5.7×10^{-5}

Table 5.8.: Fraction of surface that would be detached from the substrate according to Equation 5.16 when applying the thermal boundary resistance model to bulk niobium data.

	f_{res}	T	I
bulk Nb	400 MHz	2.5 K	3.1×10^{-6}
		4.0 K	1.1×10^{-5}
	800 MHz	2.5 K	-8.1×10^{-6}
		4.0 K	5.9×10^{-6}

The relation between quench field and thermal boundary resistance and the normal conducting resistance is then used to assign a $R_{Nb/Cu}$ value and a value of the distribution function to every data point of each R_S (B_{RF}) curve. Figure 5.17 shows the calculated distribution function and thermal boundary resistance values for the four data sets for the niobium film and the bulk niobium data with a corresponding power law fit. It can be seen that the resulting distribution functions for all Nb/Cu data match well while for the bulk niobium they are more scattered.

Integrating each distribution function over all values of R_B, yields the fraction of detached area:

$$I = \int_r^\infty f\left(R_{Nb/Cu}\right) \mathrm{d}R_{Nb/Cu} \tag{5.16}$$

The minimum thermal boundary resistance r corresponds to the highest RF magnetic field value of the R_S (B_{RF}) curve and is for all curves of both samples in the order of 200 $\mathrm{cm^2 K/W}$.

Table 5.7 lists the resulting values for the detached surface area of the ECR film. All values are similar as expected which reinforces the applicability and significance of the thermal boundary resistance model. After averaging the fraction values the total detached surface area of the ECR sample can be estimated to:

$$A_{detached} = (3.4 \pm 0.7)\, 10^{-5} \cdot \pi r^2_{sample} = (0.15 \pm 0.03)\, \mathrm{mm^2}. \tag{5.17}$$

The fraction of 0.0034 % is one order of magnitude less than the value reported for one of the best 1.5 GHz DC magnetron sputtered cavities [97]. This further supports the expectations of significantly improved film adherence and interface quality for energetic condensation techniques.

Table 5.8 shows the integration results of the distribution functions of the bulk Nb data. The values for the fraction of *detached surface* spread over almost one order of magnitude for three data sets. Moreover, the 800 MHz/2.5 K curve yields a negative fraction which is physically meaningless. This supports the non-applicability of the model to bulk niobium data which in turn further supports its validity for the Nb/Cu system.

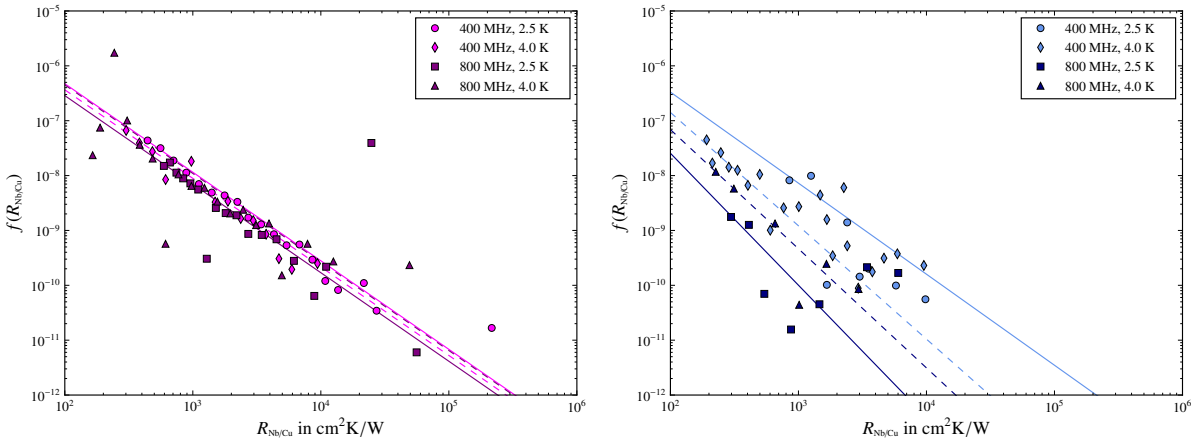

(a) (b)

Figure 5.17.: Calculated distribution function versus thermal boundary resistance for all data sets of (a) the ECR niobium film on copper and (b) the bulk niobium sample.

5.1.7. Comparison with Sputtered Cavities

This section is dedicated to benchmark the performance of the ECR sample to other Nb/Cu coatings: As will be laid out, the Q-slope does not depend on frequency, which allows a comparison across different cavity projects. ECR samples Q-slope is significantly flatter than most other coatings. Only the example of one of the best dcms coatings from CERNs R&D program on 1.5 GHz cavities, has comparable performance and suggests that the typical steep Q-slope is not inherent to the DCMS technique.

The Q-slope data presented in Section 5.1.5 suggested that it has an intrinsic temperature dependence which becomes stronger at lower temperature, in particular around and below 2 K. On this basis, only the 4 K data of the ECR sample is now compared to cavity data between 4.0 K and 4.5 K of various Nb/Cu projects which are listed with their frequency and exact temperature in Table 5.9. The total surface resistance is as previously applied to the ECR coating fitted via

$$R_s = R_0 \cdot \exp(b \cdot B_{RF}) \tag{5.18}$$

and data and fit function are shown in Figure 5.18a. As can be seen, the fit matches well the data for all curves and for RF fields above 10 mT.

Figure 5.18b compares the ECR coating with typical LEP and LHC data as all three have comparable frequencies of 352 MHz and 400 MHz. Although the RF field dependence of the ECR coating is still stronger than bulk niobium, it is by far flatter than the standard magnetron sputtered films of the past and supports again the potential of energetic condensation techniques for SRF films.

The low field surface resistance R_0 from Equation 5.18 comprises BCS and residual parts for each coating. Due to the lack of $R_S(T)$ data, the low field, 0 K residual resistance cannot be extracted and hence R_0 cannot be deconvoluted into BCS and residual contributions. As a consequence, a comparison of R_0 for the different coatings is not meaningful.

Table 5.9.: Nb/Cu coatings used for an analysis of Q-Slopes.

Project/ Accelerator	Frequency [MHz]	Temperature [K]	Geometry	Coating Technique	Reference/ Cavity ID
HIE-Isolde	101	4.5	Quarterwave	Diode Sputtering	QS5.2 [173]
LEP	352	4.5	Elliptical, $\beta = 1$	DCMS	[2]
LHC	400	4.5	Elliptical, $\beta = 1$	DCMS	[40]
low-β R&D	600	4.5	Elliptical, $\beta = 0.8$	DCMS	[40]
QPR	400	4	flat disk	ECR	this thesis
QPR	800	4	flat disk	ECR	this thesis
HIPIMS R&D	1300	4.2	Elliptical, $\beta = 1$	DCMS-like HIPIMS	M2.7 [174]
DCMS R&D	1500	4.2	Elliptical, $\beta = 1$	DCMS	[13]

Nevertheless, the Q-slope parameter b can be compared and is plotted as function of frequency in Figure 5.19. It shows clearly a separation of the magnetron sputtered cavities of the 1980s and early 1990s, i.e. LEP and LHC, from the rest. Considering that LEP was the first accelerator to use niobium coated cavities and the technology was quickly adapted for LHC, it is not surprising that this group is lower performing than more recent projects. Within the LEP/LHC group, it can be seen that the $\beta = 0.8$ performs worse compared to the $\beta = 1$ cavities. This is well in line with the general finding of performance reduction of low(er) β elliptical cavities [70, 172].

A vigorous R&D programme in the late 1990s pushed the further development of the sputter coating technique on 1.5 GHz cavities involving over 100 coated cavity cold tests. The improvement can clearly be seen here - the typical 1.5 GHz Nb/Cu cavity has a Q-slope parameter comparable to the ECR coating. It remains the most optimized coating process for Nb/Cu cavities. Also the more recent projects, HIE-Isolde and the HIPIMS development on 1.3 GHz cavities, perform significantly better than the coatings from the LEP era.

HIE-Isolde with its quaterwave resonator geometry benefits from the high mass of the substrate which allows a coating temperature of 650 °C. The higher temperature increases the mobility of arriving particles on the surface and improves hence the film microstructure.

The HIPIMS development is based on the 1.5 GHz programme. The cavity M2.7 which is presented here was coated with the HIPIMS technique but without any bias on the cavity. Most recent findings suggest that an unbiased HIPIMS coating will result in a microstructure comparable to the magnetron sputtering [75]. The data is therefore rated as dcms-like.

It can be concluded that although early in the development, the Q-slope of the ECR coating is not only significantly mitigated compared to LEP and LHC but also reduced compared to the more recent Nb/Cu projects. The comparison also supports the speculation from Section 5.1.5 that the Q-slope parameter may not depend on frequency. Nonetheless, this analysis also shows that a much weaker Q-slope can be achieved if the process is highly optimised.

5.1.8. The Effect of Cooling Conditions on the Performance

This section presents the impact of cool down on the surface resistance: As will be shown, the surface resistance of bulk niobium is lower for *slow* cooling resp. large temperature gradients. The effect is in the order of few nΩ or 10 %. In contrast, the ECR Nb/Cu sample shows smallest residual resistance and

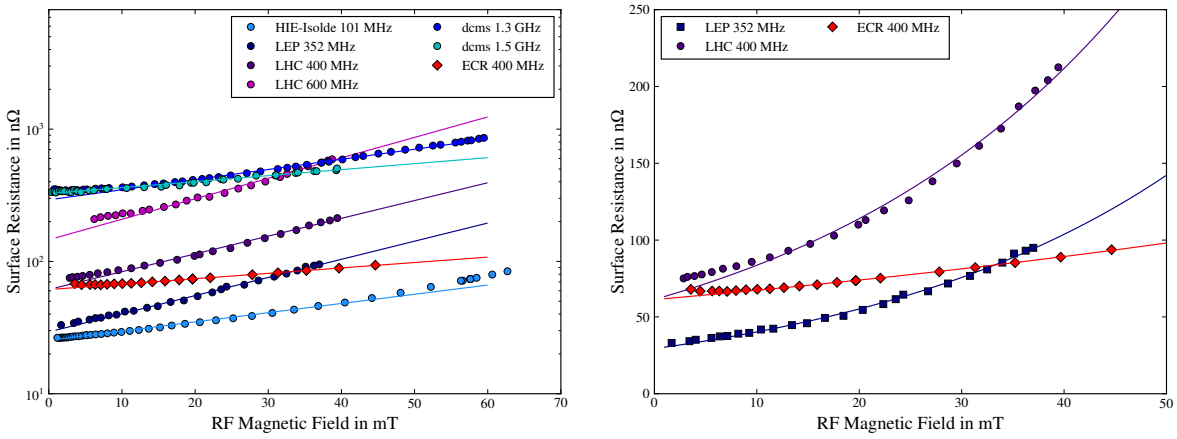

(a) Comparison of typical Nb/Cu performances for various projects at 4 K to 4.5 K.

(b) Comparison of the ECR coating at 400 MHz and 4 K with LEP and LHC at 4.5 K.

Figure 5.18.: Typical Q-slopes for Nb/Cu films.

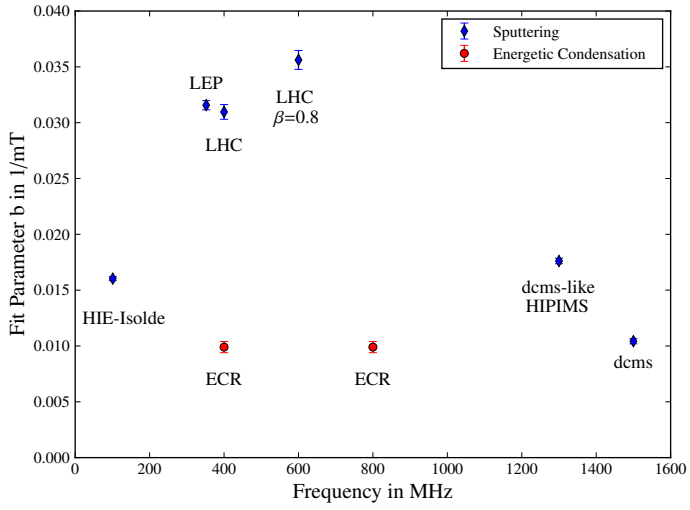

Figure 5.19.: Exponential Q-slope parameter from fitting the Q-Slope for different coatings.

flattest Q-slope for *fast* cooling, resp. minimal temperature gradient. The impact for cooling conditions is much greater than in bulk Nb, almost doubling the residual resistance.

The thermal decoupling of the Quadrupole Resonator from the sample allows thermal cycling of the sample, i.e. warming the sample above the transition temperature and cooling it down again under defined conditions, within one to two hours. Typically, the sample was warmed up to 15 K to ensure that the whole sample cylinder was normal conducting. In any case, the maximum temperature was always kept below 20 K to avoid Q-disease due to the formation of niobium hydrides above 50 K.

Figure 5.20 shows two typical cool down curves from a *slow* and a *fast* cool down. The cooling rate is determined by linearly fitting the temperature decrease around T_c with a temperature span of 0.2 K for slow cooling. For fast cool downs this fit range was increased in 0.1 K steps until at least 4 points are covered. For the fastest cool downs this corresponds to a maximum temperature fit range of 1.8 K around T_c.

Due to the DC heater in the center of the sample being the only heat source and the contact to the helium bath through the flange being the heat sink, cooling rate and the spatial temperature gradient across the sample cannot be changed independently from each other. Moreover, since the temperature diodes are all in the same radial distance from the heater, the temperature gradient cannot be measured. Nonetheless, the thermal simulations presented in Section 4.2.2 showed that the slower the samples are cooled, the bigger the temperature gradient across the sample is. A thermal voltage would therefore built up along the sample surface: from the sample centre towards the edge and downwards along the sample cylinder.

It is well known that the cooling conditions have a strong influence on the residual resistance of high quality bulk niobium as well as Nb/Cu films. To explain this, two effects have to be considered: When a temperature gradient is present, a thermal voltage builds up and induces a thermal current if the current path is closed. Thermal currents can in turn induce magnetic fields that can be trapped and cause additional losses [23, 24]. The thermal voltage and currents are proportional to the temperature gradient and the effect can be emphasised at a metal-metal interface [175]. The cooling conditions might also act on the flux trapping efficiency, i.e. how much of the ambient field is not expelled from the superconductor [19, 176]. In some vertical tests it was found that at temperature gradient across the cavity can support flux expulsion [22, 177].

The change of surface resistance of the reactor grade bulk niobium sample with cooling rate at 2.5 K and 15 mT for 400 MHz and 800 MHz is shown in Figure 5.21 . The secondary x-axis shows an estimate of the temperature gradient across the sample from center to edge based on the thermal simulation and Equation 4.18. The measured cooling rate for a given input heating power is plotted in Figure 5.22 with a linear trend for intermediate values. The resulting function is matched with the results from the thermal simulation which related heating power with temperature gradient across the sample from the center to the edge where it connects to the sample cylinder. Finally, the temperature gradient as function of cooling rate v_{cool} can be estimated via

$$\Delta T_{\mathrm{Bulk}} = (688 \pm 45)\,\mathrm{mK} - (1.72 \pm 0.10)\,\mathrm{s} \cdot v_{\mathrm{cool}}. \tag{5.19}$$

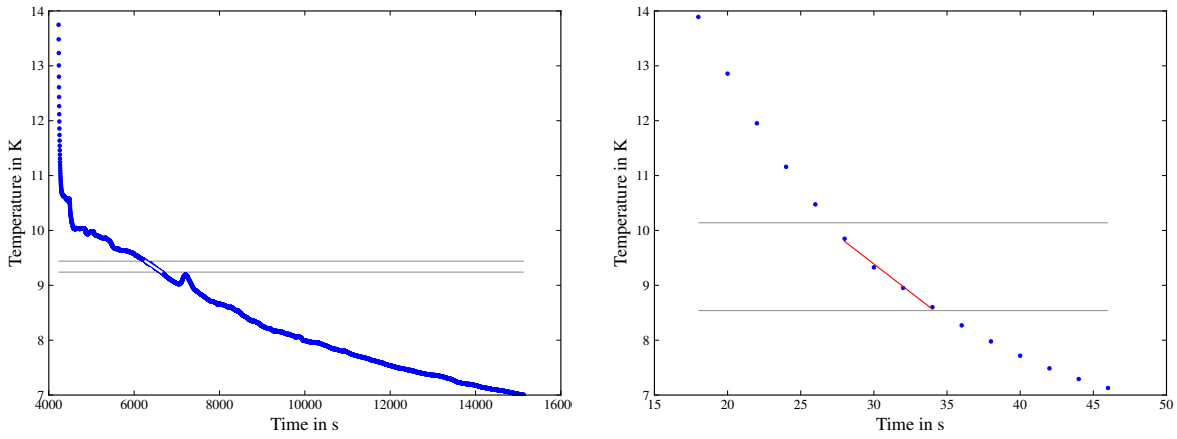

(a) (b)

Figure 5.20.: Cooldown curves and fit lines for determining the cooling rate for (a) the initial cool down and (b) the thermal cycle #6 of the ECR sample. The grey horizontal lines indicate the fit range which depends on the number of points around T_c.

The temperature gradient values should serve as a qualitative estimate since it remains unknown how well the simulation describes the actual cooldown.

The surface resistance does not show a dependence for cooling rates above 200 mK/s, but decreases for lower cooling rates. Thermal currents can be excluded as an explanation since there is no return path from the sample or the Quadrupole Resonator back to the sample centre. Moreover, the surface resistance would be expected to increase with slower cooling as the temperature gradient across the sample increases. Other extrinsic factors such as a change in ambient magnetic field can also be ruled out: The residual magnetic field in the cryostat could change when the magnetic properties of the surrounding materials change or when additional fields are created. A passive magnetic shielding is placed around the cryostat, reducing the ambient field around the Quadrupole Resonator to less than 3 µT. The magnetic shield remains at room temperature so that its magnetic properties do not change. Alternatively, the DC heater could in principle create an additional magnetic field which superposes the residual field in the cryostat. If oriented in the opposite direction of the residual field the sample would be exposed to smaller fields when cool down is slowed down. To rule out this possibility, the surface resistance was measured for both polarities of the DC heater, yielding the same surface resistance trend as function of cooling rate.

The lower surface resistance for slow cooling is well in line with temperature gradient assisted flux expulsion: The higher the gradient, the stronger the sweep force, pushing the external magnetic field either out of the sample or to the sample centre which only sees low RF fields.

For the RF characterisation of the ECR sample the setup allowed measuring the DC heating power during cool down directly and the thermometry chamber was equipped with a magnetic field probe. Figure 5.22 shows the correlation between the measured cooling rate and measured DC power used to slow down the cooldown. The data follows roughly a linear trend which is correlated with the

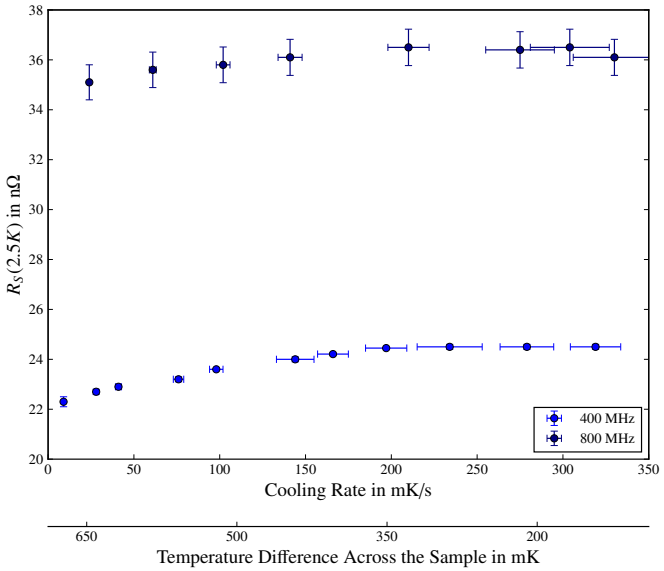

Figure 5.21.: Surface Resistance of the reactor grade bulk niobium sample at 400 MHz, 2.5 K and 15 mT as function of cooling rate.

Table 5.10.: $R_S(T)$ fit parameters for different cool down schemes.

Parameter	Initial cool down	Thermal cycle #6
A_{BCS} in nΩK	9898 ± 1096	10 096 ± 1606
Δ/k_B in K	17.7 ± 0.5	18.3 ± 0.7
R_{res} in nΩ	35.5 ± 0.5	29.6 ± 0.6

simulated relation between DC heating power and temperature gradient across the sample as described by Equation 4.19. The according temperature gradient as function of cooling rate can be described since

$$\Delta T_{Film} = (33.9 \pm 4.7)\,\text{mK} - (0.093 \pm 0.010)\,\text{s} \cdot v_{cool}. \tag{5.20}$$

Also for this sample, the temperature gradient values serve primarily as rough estimate as it remains unknown how well the simulation describes the actual cool down. Nonetheless, it must be noted that the expected temperature gradient across the Nb/Cu sample is more than one order of magnitude smaller than the expected temperature gradient of the bulk niobium sample.

In order to confirm that also for this niobium film the cooling conditions only act on the residual part of the surface resistance, R_S was measured as function of temperature for both of the two thermal cycles presented in Figure 5.20. The data was exponentially fitted according to Equation 3.4 and the resulting fit parameters can be found in Table 5.10. As can be seen from the fit parameters and in Figure 5.23, the two curves differ only in an offset. The fact that the BCS factor A_{BCS} as well as the superconducting gap overlap within their error bars, indicates that only the residual resistance R_{res} changes and the BCS contribution and hence the material parameters remain unchanged with the thermal cycle. Therefore the thermal cycle studies are focussing on the residual resistance and the study is restricted to 400 MHz and 2.0 K.

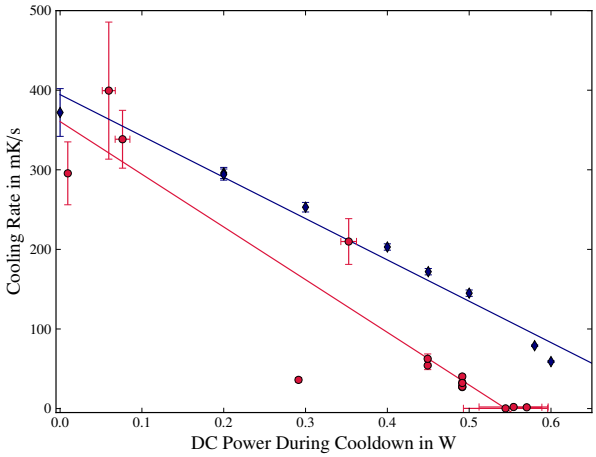

Figure 5.22.: Measured cooling rate as function of DC heating during cool down. Blue symbols indicate the bulk niobium sample; red symbols indicate the ECR sample. The data is combined with Equations 5.19 and 5.20 to estimate the temperature gradient across the sample with the cooling rate.

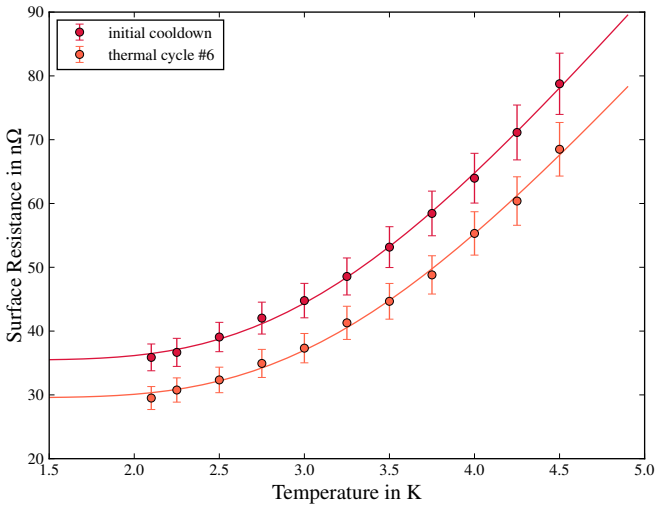

Figure 5.23.: Surface resistance of the ECR sample as function of temperature for the initial cool down and thermal cycle #6. The thermal cycle acts only on the residual part of the surface resistance.

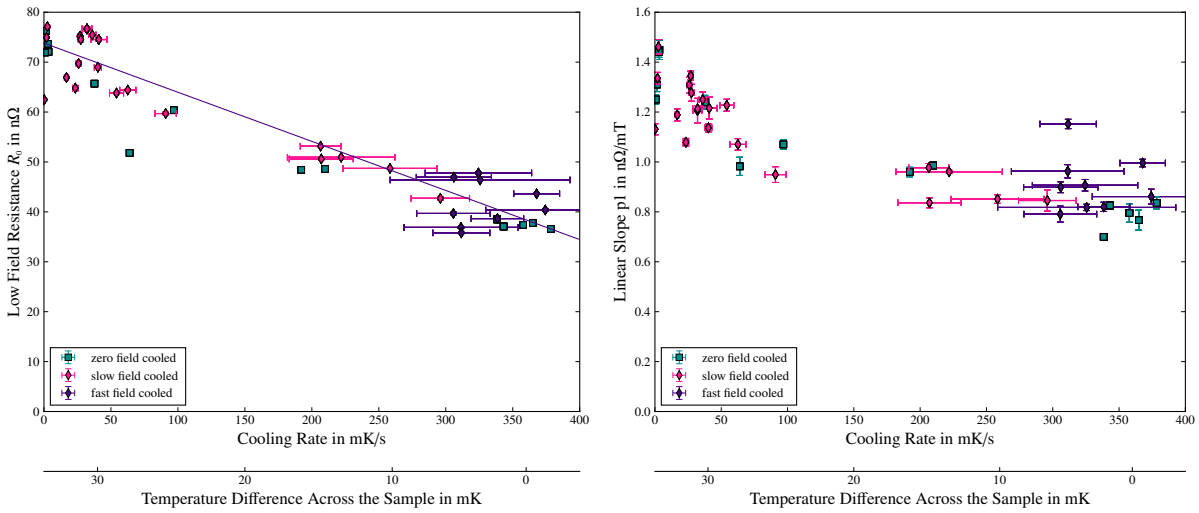

(a) (b)

Figure 5.24.: (a) The low field surface resistance of the ECR sample and (b) the linear slope as function of cooling rate.

Each thermal cycle is categorised according to the specific cooling conditions: *Field cooled* refers to the field of the DC coil which created up to 150 µT on the sample surface. Accordingly, the sample is only cooled down in the residual ambient field of about 3 µT for the *zero field cooled* case. The cooling rates were rated as *fast* for rates above 300 mK/s and *slow* for rates below 300 mK/s.

The surface resistance was measured under various cooling rates and with and without an external DC magnetic field. At 2 K, not the full RF magnetic field range is accessible due to the high residual resistance. As a result, the increase of R_S with B_{RF} is too flat for a meaningful exponential fit, therefore the data is fitted with a linear trend:

$$R_S\,(B_{RF}, 2.0\,\mathrm{K}) = p1 \cdot B_{RF} + R_0, \tag{5.21}$$

where the parameter $p1$ represents the linear slope and R_0 is the low field surface resistance which matches approximately the residual resistance as the BCS resistance at 400 MHz and 2.0 K is in the order of 1 nΩ.

Figure 5.24 shows how the low field resistance and the slope parameter increase for slower cooling. Three aspects need to be addressed: First, in contrast to the bulk niobium sample, the surface resistance increases for lower cooling rates. Second, R_0 and $p1$ increase by about a factor of 2 while the surface resistance of the bulk niobium sample changed by about 15 % or 3 nΩ. Third, there is no obvious difference between the zero field cooled data and the field cooled data for neither parameter.

Potential mechanisms for the strong dependence on cooling rate are flux expulsion, lossy niobium hydride formation and thermal currents.

If flux expulsion was the dominant mechanism, the change in surface resistance should decrease with increasing temperature gradient. This is not the case here. Moreover, the effect of the cooling rate is significantly stronger than the effect of trapped (ambient) flux although external fields up to 150 µT were

applied. Even if the sample was only cooled in the residual ambient field of about 3 µT R_0 increases by 40 nΩ when cooled very slowly.

The fact that the sample was never warmed up above 20 K, the performance is reversible with thermal cycling and the material parameters remain unchanged excludes also chemical reactions such as niobium hydride formation or diffusion processes as possible cause for the performance change.

The larger surface resistance for larger temperature gradients supports the hypothesis of thermal currents. As argued for the bulk niobium case, no current flow is possible from the support flange of the sample as coldest point back to the sample center as the warm end. However, in contrast to the bulk niobium case, the ECR sample represents a two-metal-system with two interfaces: a copper-niobium interface at the welding between the support tube and the sample disk and a copper-niobium interface between film and substrate themselves. As the sample cools down, a temperature gradient dT arises with components normal to and along the samples surface as discussed in Section 4.2.2. According to the Seebeck effect, a voltage U_{thermo} drop is created between the two metals

$$U_{\text{thermo}} = \int_{T1}^{T2} (S_{\text{Cu}}(T) - S_{\text{Nb}}(T))dT, \tag{5.22}$$

with the material specific and temperature dependent Seebeck coefficients S_{x} for Nb and Cu. U_{thermo} is proportional to an electric field E which is linked to a current density j via Ohms law $\vec{j} = \sigma\vec{E}$. With the conductivity of niobium σ_{Nb} drastically increasing as the temperature approaches the critical point T_{c}, the current density must increase to the same extend in order to sustain the electric field, resp. the thermo voltage.

As these thermo-electric currents built up, magnetic fields are created, mainly in the Nb-Cu interface plane resp. parallel to it.

These findings are in line with measurements on HIE-Isolde quarterwave resonators which also show lower surface resistance and mitigated Q-slope for more uniform cooling, i.e. smaller temperature gradient across the cavity [178]. Also here it holds that the change in surface resistance due to the cooling exceeds the effect of trapped flux from an ambient field by far.

5.1.9. The Influence of Trapped Flux

This section discusses the role of ambient magnetic field on the surface resistance. As will be discussed, the ECR Nb/Cu sample trapped 100 % of ambient field up to a threshold field of > 111 µT. The amount of trapped flux beyond this threshold field appears not to depend on the cooling rate. Furthermore, the trapped field causes only very small additional surface resistance and is outweighed by the additional losses related to cooling conditions.

The DC coil described in Section 4.3 is used for studying the effect of trapped flux in the sample. For this, the coil was switched on during thermal cycling when the sample was normal conducting and switched off after the sample was fully superconducting again. As discussed in Section 4.3, the magnetic fields measured by the fluxgate have to be extrapolated to the actual fields on the sample surface. Where applicable, the scaled fields are plotted as a secondary axis while the directly measured field remains on the primary axis. After the sample temperature is well below the transition temperature, the coil is

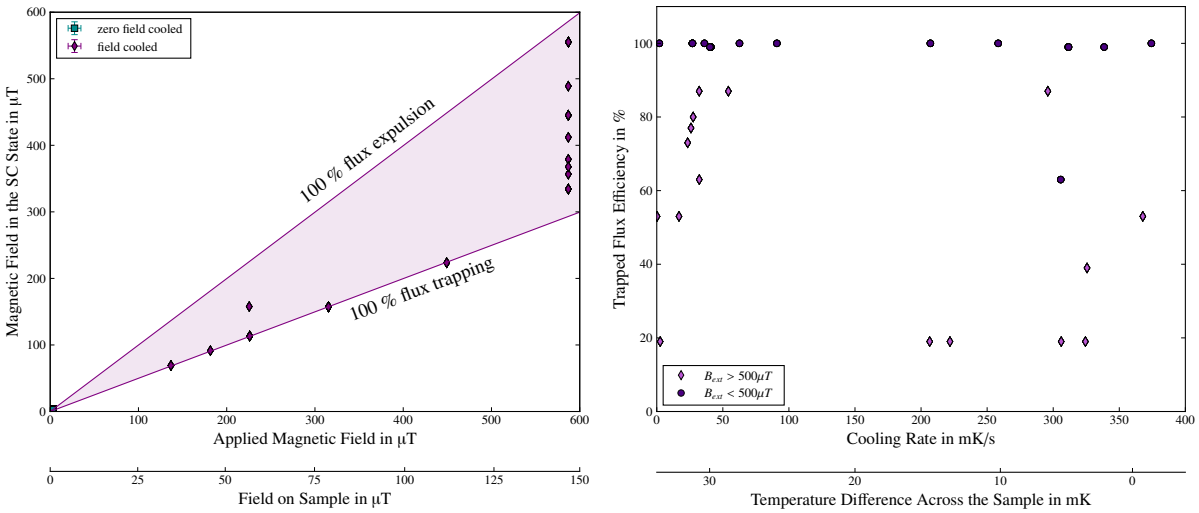

(a) (b)

Figure 5.25.: Influence of (a) the strength of the applied field and (b) the cooling rate on the trapped flux efficiency of the ECR sample.

switched off and the surface resistance is measured in the usual way after the sample reached equilibrium at the helium bath temperature.

To determine the trapped flux efficiency, Figure 5.25a compares how much field is applied and how much is measured after cooling down and switching off the coil. For low fields the ratio of trapped field and applied field is constant (neglecting one outlier). This ratio cannot be predicted by the simulation as discussed in Section 4.3.2 but based on the findings that sputtered Nb/Cu films show 100 % flux trapping and considering that the ratio of applied field and trapped field deviate throughout the different thermal cycles within less than 0.1 %, this ratio is identified with a flux trapping efficiency of 100 %. Linear extrapolation yields the ratio of measured magnetic field in the normal conducting and superconducting state equivalent to 0 % flux trapping, i.e. 100 % flux expulsion which is also indicated in Figure 5.25a.

The trapping efficiency follows 100 % except for one outlier and the set of measurements at the highest applied fields of 587 µT (at the position of the magnetic field probe). It appears that there is a threshold field above which a fraction of the applied field is not trapped. This threshold field is between 111 µT to 145 µT on the sample. Figure 5.25b plots the trapped flux efficiency versus the cooling rate. There is no correlation between the trapped flux efficiency and the cooling rate: Not only stretches the 100 % flux trapping data over the whole cooling rate range, also the data set with flux trapping efficiencies between 20 % to 90 % does not show any trend with cooling rate[1]. For this sample, it has to be concluded that as soon as not all the applied field is trapped, the actual efficiency is not driven by the cooling rate.

[1]Note: the specified field range for this fluxgate is up to 290 µT and effect might be due to saturation of the probe.

The influence of trapped field on the RF performance can be described by the *trapped flux sensitivity* S_{TF}. Figure 5.26a shows the low field surface resistance which was derived by fitting $R_{\mathrm{S}}\,(400\,\mathrm{MHz}, 2\,\mathrm{K}, B_{\mathrm{RF}})$ according to Equation 5.21 as function of trapped magnetic field. The data set was again split into three subgroups as previously introduced: zero field cooled and slow and fast field cooled. The fast field cooled group comprises data for cooling rates between 306 mK/s to 374 mK/s and was used to derive the trapped flux sensitivity S_{TF}, i.e. the additional surface resistance for a given trapped field. A linear fit finds:

$$S_{\mathrm{TF,\,ECR}}\,(400\,\mathrm{MHz}) = (0.0218 \pm 0.0007)\,\frac{\mathrm{n\Omega}}{\mu\mathrm{T}} \qquad \text{and} \tag{5.23}$$

$$S_{\mathrm{TF,\,ECR}}\,(800\,\mathrm{MHz}) = (0.075 \pm 0.009)\,\frac{\mathrm{n\Omega}}{\mu\mathrm{T}} \tag{5.24}$$

The trapped flux sensitivity of the bulk niobium sample was also derived by fitting the low field surface resistance for cooling rates around 300 mK/s versus applied field and is shown in Figure 5.26b for comparison. The sensitivity of

$$S_{\mathrm{TF,\,bulk}}\,(400\,\mathrm{MHz}) = (0.204 \pm 0.007)\,\frac{\mathrm{n\Omega}}{\mu\mathrm{T}} \qquad \text{and} \tag{5.25}$$

$$S_{\mathrm{TF,\,bulk}}\,(800\,\mathrm{MHz}) = (0.382 \pm 0.008)\,\frac{\mathrm{n\Omega}}{\mu\mathrm{T}} \tag{5.26}$$

for the bulk niobium is about 8 resp. 5 times higher than the ECR film. The trapped flux sensitivity of the niobium film agrees well with measurements of sputtered niobium films such as 0.024 nΩ/μT to 0.035 nΩ/μT for HIE-Isolde [179] and 0.04 nΩ/μT to 0.08 nΩ/μT for the 1.5 GHz DCMS cavities [13]. The trapped flux sensitivity of the bulk niobium sample is significantly lower than an expected value of 4.7 nΩ/μT (for 400 MHz derived from scaling the reference of 3.6 nΩ/μT [35] with $\sqrt{f/1.5\,\mathrm{GHz} \cdot 300/RRR}$. This discrepancy will be subject to Section 5.2.

Finally, the impact of trapped flux on the Q-slope is determined: Comparing the ECR field cooled data with the zero field cooled data shows that the influence of the cooling rate is much stronger: While the low field surface resistance can only be increased by around 20 % over the available field range, the cooling rate can as much as double the low field resistance. It must be noted that the available field range is about 3 times the earth magnetic field, the cooling rate range covers typical cooling rates for e.g. HIE-Isolde cavities. The corresponding temperature gradients per unit length are comparable with HIE-Isolde [178] and the 1.3 GHz Nb/Cu cavities at CERN [174] and in the order of 1 K/m which is much smaller than typical for bulk niobium with easily 50 K/m [24, 177]. A 3 D plot showing the low field surface resistance R_0 as function of cooling rate and trapped field is shown in Figure 5.27.

The spread of the linear slope is too big to correlate $p1$ with the trapped field, but as Figure 5.28 shows, in general the higher the low field resistance, the stronger the slope, holds. Fitting the zero field cooled and the slow field cooled data with a linear trend yields

$$p1 = (0.0143 \pm 0.0003)\,1/\mathrm{mT} \cdot R_0 + (0.23 \pm 0.02)\,\mathrm{n\Omega/mT} \tag{5.27}$$

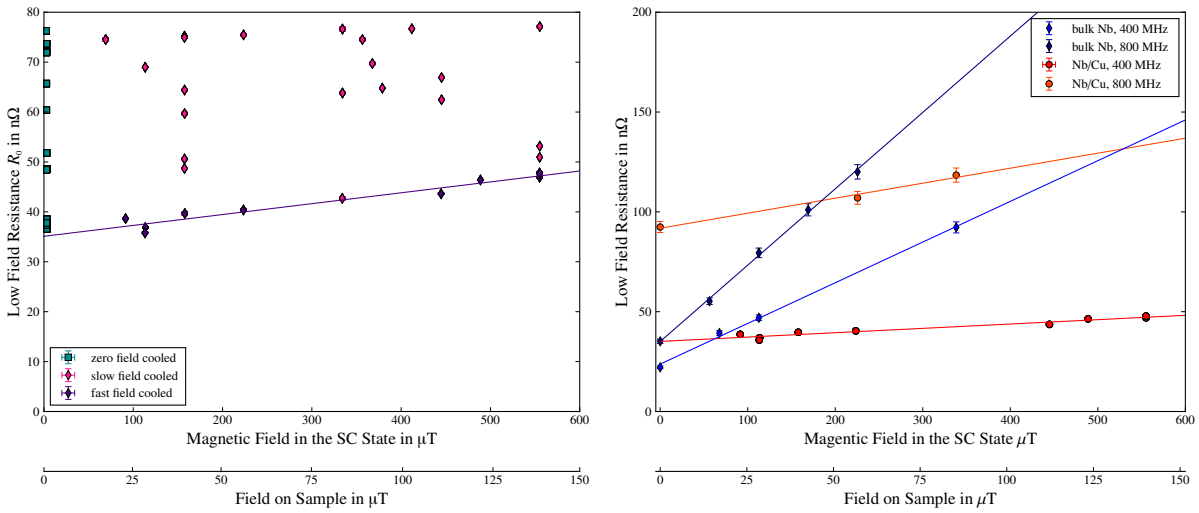

(a) (b)

Figure 5.26.: (a) Low field surface resistance as function of trapped field for the ECR coating with different cooling schemes. Compare also Figure 5.27 for a 3 D view. (b) Low field surface resistance as function of trapped field for the bulk Nb sample compared to the ECR sample for fast cooldowns (> 300 mK/s).

which is even for zero residual resistance about twice of bulk niobium.

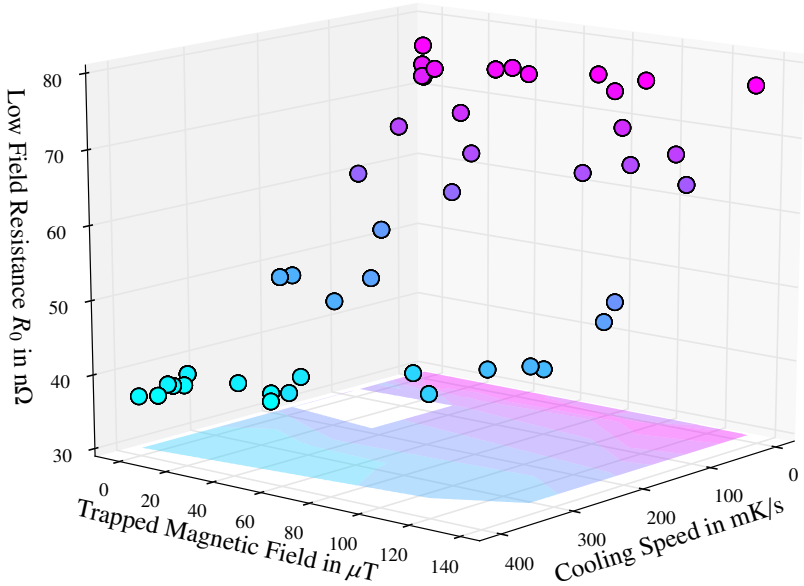

Figure 5.27.: Low field surface resistance as function of trapped magnetic field and cooling rate for the ECR sample.

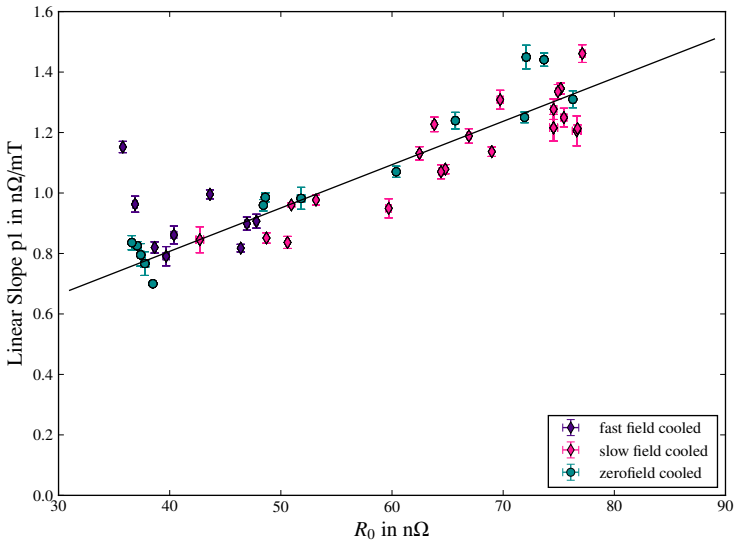

Figure 5.28.: Correlation between the linear slope $p1$ and the low field surface resistance R_0 of the ECR sample.

5.2. The Trapped Flux Sensitivity

This section is dedicated to further discuss the differences in trapped flux behaviour between bulk Nb and Nb/Cu films. It is believed that the depinning frequency plays a crucial role in these differences, so an empirical formula based on the available literature values is derived and tested against the QPR data. The model considers not only RRR and operational frequency, but also (relative) pinning strength. It supports the hypothesis that the stronger pinning in Nb/Cu films causes the lower trapped flux losses while low to moderate RRR and low frequency are additionally beneficial.

Experimental data for trapped flux sensitivity as function of mean free path or RRR exists mostly for the combinations of high RRR and high frequency (bulk niobium) or low RRR and low frequency (niobium films). Both scenarios describe the two plateaus for the depinning but trapped flux measurements on the slope of the depinning curve (see Figure 3.3) would be required for a derivation of the depinning frequency. However, one data set from the 1980's is available, describing the flux trapping behaviour for RRR 110 at 500 MHz [180, 181]. The authors derive a flux trapping sensitivity of

$$S_{\mathrm{TF,meas}} = 1.22\,\mathrm{n\Omega/\mu T}. \tag{5.28}$$

The reference value, assuming 100 % flux trapping and full depinning is 3.6 nΩ/μT at 1.5 GHz for RRR 300 material [105]. This flux trapping sensitivity S_{TF} scales with $\sqrt{f_0/RRR}$. Scaling down to RRR 110 at 500 MHz yields an expected trapped flux sensitivity of

$$S_{\mathrm{TF,ref}} = 3.4\,\mathrm{n\Omega/\mu T} \tag{5.29}$$

which does not agree with the experimental value.

This discrepancy can be attributed to a different depinning behavior. Comparing the experimental value with the expected value yields a depinning efficiency of about

$$\varepsilon_{\mathrm{pin}} = \frac{1.22}{3.4}\mathrm{n\Omega/\mu T} \approx 35\,\% \tag{5.30}$$

and places this measurement on the slope of the depinning curve.

The depinning frequency for RRR 110 can now be derived using Equation 3.27,

$$f_{\mathrm{p}}\,(RRR = 110) = \sqrt{\frac{f_0^2\left(\varepsilon_{\mathrm{pin}} - 1\right)}{\varepsilon_{\mathrm{pin}}}} = 673\,\mathrm{MHz} \tag{5.31}$$

This result is used as a new reference point: Figure 5.29 shows the depinning frequency as function of RRR following the $1/RRR$ scaling from Equation 3.26 across the typical RRR range under the assumption that the pinning mechanism does not change significantly.

Table 5.11 lists a few examples of RRR values with the corresponding depinning efficiency for a typical operating frequency. It can be seen that the expectation of (almost) full depinning for typical bulk niobium with RRR 300 at 1.3 GHz and (almost) full pinning for typical Nb/Cu with RRR 15 at 400 MHz is fulfilled.

Table 5.11.: Calculated depinning frequency based on Equation 5.31

RRR	Depinning frequency	Typical operation frequency	Depinning efficiency
15	4.94 GHz	400 MHz	<1 %
47	1.56 GHz	400 MHz	6 %
67	1.10 GHz	400 MHz	12 %
300	247 MHz	1.3 GHz	97 %

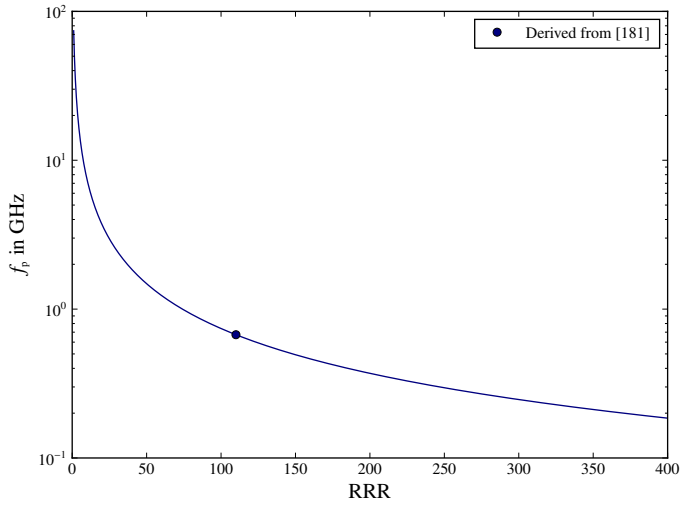

Figure 5.29.: Depinning frequency f_p as function of RRR.

For a prediction of the additional surface resistance due to trapped flux, three aspects have to be accounted for: the amount of trapped field, the losses of the normal conducting regions and the depinning of trapped flux. The first factor is given by the ambient field B_{ext} and the flux trapping efficiency ε_{TF}. It has been shown that the treatment history of the material has a strong influence of the percentage ε_{TF} that is trapped, ranging from 40 % to 100 % [19] . Moreover, the cool down speed and/or temperature gradient might change the amount of ambient field that is actually trapped [23, 21]. Secondly, the losses of trapped flux can be related to the normal electrical conductivity of the material and to the operation frequency and scale therefore like the normal resistance with $\sqrt{f_0/RRR}$ which is already reflected in Equation 3.28. Lastly, the mean free path defines the depinning frequency but also the size of the pinning center p has an influence. The latter cannot be measured, but the scaling following Equation 3.26, i.e. with p/RRR, may apply.

Based on the estimation of the depinning frequency and accounting for the scaling of the different factors, an empirical formula is introduced to estimate the additional surface resistance due to trapped flux, R_{TF}:

$$R_{\text{TF}} = 3.6\,\text{n}\Omega/\mu\text{T}\sqrt{\frac{f_0}{1.5\,\text{GHz}}\frac{300}{RRR}}\cdot\frac{f_0^2}{f_0^2+\left(p\cdot 673\,\text{MHz}\frac{110}{RRR}\right)^2}\cdot B_{\text{ext}}\cdot\varepsilon_{\text{TF}} \tag{5.32}$$

The trapped flux sensitivity is accordingly:

$$S_{\text{TF}} = 3.6\,\text{n}\Omega/\mu\text{T}\sqrt{\frac{f_0}{1.5\,\text{GHz}}\frac{300}{RRR}}\cdot\frac{f_0^2}{f_0^2+\left(p\cdot 673\,\text{MHz}\frac{110}{RRR}\right)^2}. \tag{5.33}$$

Since the pinning center size p cannot be measured, it is normalised to 1 so that relative changes of the trapped flux sensitivity due to changes in frequency, RRR and p can be evaluated.

Figure 5.30 shows the trapped flux sensitivity as function of RRR for 400 MHz, 800 MHz and 1200 MHz. The curve has a maximum that is strongly mitigated for low frequencies but pronounced at 1.2 GHz. As a result, the trapped flux sensitivity of high frequency ($>$ 1 GHz) cavities become very sensitive to treatments that significantly shorten the mean free path such as the 120 °C baking or nitrogen doping.

Figure 5.31 shows the trapped flux sensitivity as function of normalized pinning center size for different RRR values and compares it between 400 MHz (Figure 5.31a) and 1.2 GHz (Figure 5.31b). The pinning center size has almost no impact on the trapped flux sensitivity for high RRR and high frequency cavities. The smaller the RRR becomes the more important is the size of the pinning center which impedes predictions.

In order to evaluate the impact of the pinning center size, Figure 5.32 combines the RRR and frequency dependence of the trapped flux sensitivity for normalized pinning sizes of 0.5, 1 and 2. For $p = 1$ the trapped flux sensitivity is highest for high frequencies and moderate RRR. Low RRR values show low trapped flux sensitivity across a wide range of frequencies while for RRR 300 only very low frequencies come with low trapped flux sensitivity. For $p = 0.5$, the region of high trapped flux sensitivity reaches further towards medium frequencies ($\approx$ 600 MHz) and covers almost the entire RRR range for high frequencies. For $p = 2$, the region of high trapped flux sensitivity has moved to high frequency and high RRR . The low trapped flux sensitivity region covers the majority of the typical application range.

Object	RRR	Frequency (GHz)	meas. TF sensitivity (nΩ/μT)	calc. TF sensitivity (nΩ/μT)	ε_{TF}	Ref.
Cavity	110	0.5	1.22	1.22	100 %	[180]
Cavity	300	1.5	3.6	3.5	100 %	[105]
LG Cavity + BCP	200	1.5	2.5 ± 0.2	3.0	73 %	[182]
LG Cavity + 1250 °C + BCP	200	1.5	1.43 ± 0.12	1.75	42 %	[182]
N doped cavity	3.3	1.3	11.3	0.09	100 %	[183]
cavity + 120 °C	8.5	1.3	3.7	0.44	100 %	[183]

Table 5.12.: Measured and calculated trapped flux sensitivity for different bulk Nb.

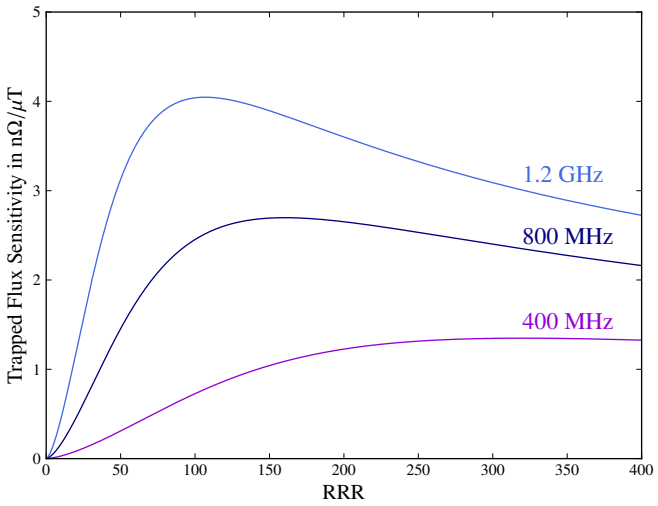

Figure 5.30.: Trapped flux sensitivity as function of RRR for different frequencies.

Finally, Equation 5.32 is used for calculating the additional residual resistance and to test the formula against experimental data. Unfortunately, the penetration depth from which the mean free path respectively the RRR can be derived is rarely measured and/or reported with surface resistance measurements. Therefore general assumptions on the effect of a certain treatment on the mean free path or approximated RRR values have to be used for the calculation. Table 5.12 lists the available trapped flux measurements and compares it with the calculated value.

The predictions fit reasonable well with standard bulk niobium data, but agrees poorly with the 120 °C baked and N doped cavities. The higher trapped flux sensitivity can be qualitatively explained by the combination of low (surface) RRR and high frequency and suggests that both heat treatments transform the pinning centres. Hydrogen and oxygen tend to segregate at grain boundaries and lattice defects but it was shown that both treatments lead to a more homogeneous distribution of hydrogen respectively oxygen in the crystal lattice [14, 184]. A more uniform distribution of hydrogen and oxygen and less segregation at grain boundaries can then be associated with smaller pinning centers.

Lastly, the results from the Quadrupole Resonator shall be tested against this empirical model. The Quadrupole Resonator allows measuring the trapped flux sensitivity for different fre-

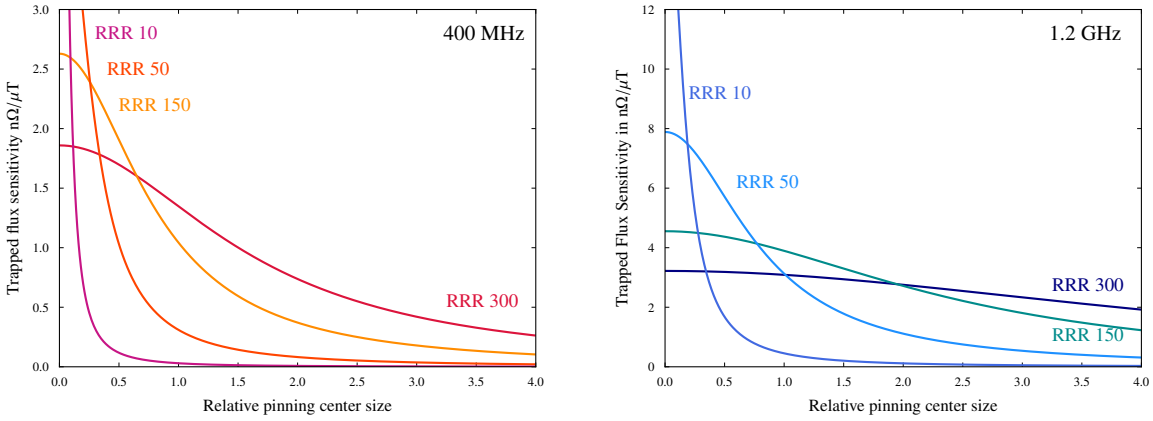

(a) (b)

Figure 5.31.: Trapped flux sensitivity as function of pinning center size for (a) 400 MHz and (b) 1.2 GHz.

quencies. Figure 5.33 shows the trapped flux sensitivity as function of frequency for the reactor grade bulk niobium sample before the mild baking. As expected, the trapped flux sensitivity increases with frequency and the data can be used to fit the relative pinning center size according to Equation 5.32. Using the measured mean free path as additional input parameter leaves p and an offset as the remaining fit parameters which represents the DC transport properties. The fit yields $p = (5.1 \pm 0.2)$ as relative pinning centre size which agrees with the expectation that lower quality niobium shows stronger pinning with bigger pinning centres than high RRR bulk niobium.

For the ECR and the baked bulk niobium no trapped flux data is available at 1.2 GHz so the 400 MHz and 800 MHz data can only be used for a consistency check. Both data sets are included in Figure 5.33. The trapped flux sensitivities of the mild baked bulk niobium sample matches the sensitivities of the sample before baking within the error bars. This is plausible considering the small effect of the mild baking on the general RF performance so that a similar pinning center size can be assumed.

The ECR sensitivity approaches zero for the DC case which implies very strong pinning. Also a fit through the origin and the data as indicated by the dashed line in Figure 5.33 yields $p_{\mathrm{ECR}} = (11.6 \pm 0.1)$, i.e. twice as big pinning centres as the reactor grade bulk niobium. This is also agrees with expected thicker grain boundaries in a deposited film compared to bulk niobium material or even pinning at the niobium-copper-interface. It is also well in line with the findings of the VSM measurements in Section 5.1.2 which support strong pinning.

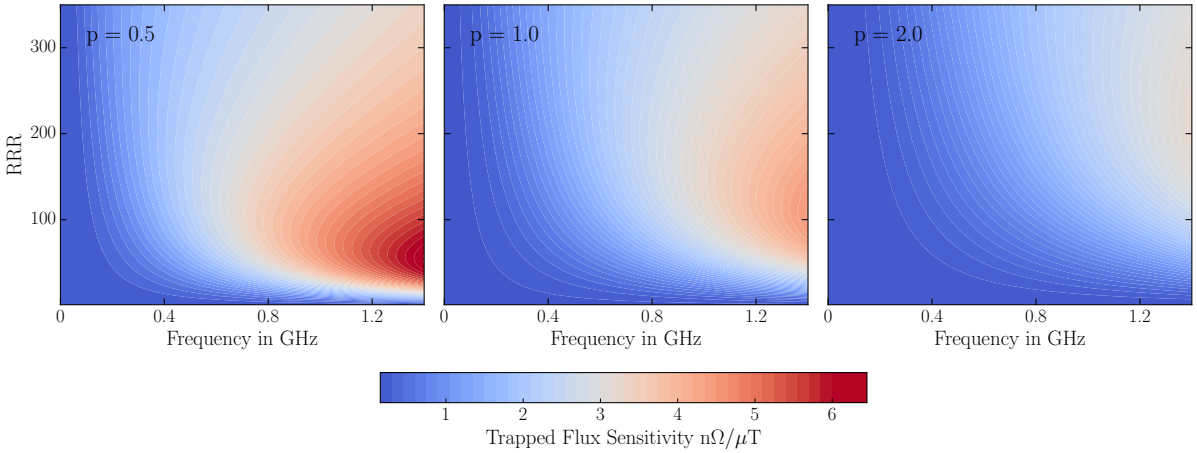

Figure 5.32.: Trapped flux sensitivity as function of RRR and operating frequency for different pinning center sizes.

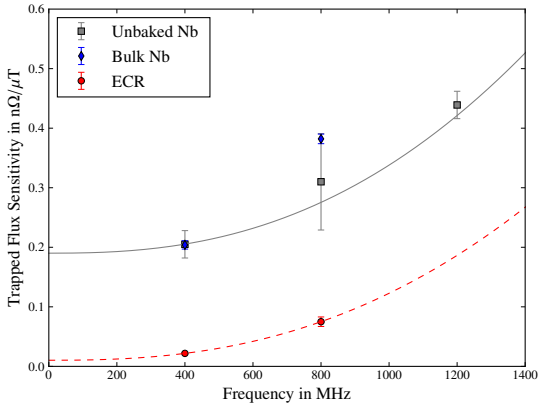

Figure 5.33.: Trapped flux sensitivity as function of frequency measured in the Quadrupole Resonator on unbaked reactor grade bulk niobium. The relative pinning center size can be derived from fitting Equation 5.32 accordingly. The sensitivities of the baked bulk niobium and the ECR sample are shown for comparison.

6. The SEY of Potential SRF Materials

In the seek for SRF materials other than niobium, the secondary electron yield (SEY) must not be neglected. A too high SEY value will limit the application of a certain superconductor to gradients below the multipacting band of an elliptical cavity. Moreover, it will exclude the material from application in more multipacting sensitive cavity geometries like most low-β structures. At CERN, there is a dedicated set-up for SEY measurements which is combined with an XPS[1] set-up. This allows coupled SEY and XPS measurements without breaking the vacuum and thus altering the surface conditions. The SEY chamber is schematically shown in Figure 6.1 and a thorough description of the set-up including a description of the electron gun and the vacuum system can be found in [185]. Primary electrons emitted from an electron gun with a defined energy bombard the surface of the mounted sample. Secondary electrons as well as scattered primaries leave the sample surface and will be absorbed by the surrounding collector and measured as a current I_c. Re-emission from the collector is suppressed by positively biasing the collector. In order to calculate the SEY, the current of the primary electrons I_p has to be known. As the source is not stable over time, it is more accurate to electrically isolate the sample from the collector, negatively bias it and measure the current through the sample I_{sample}. The secondary electron yield can be derived as follows:

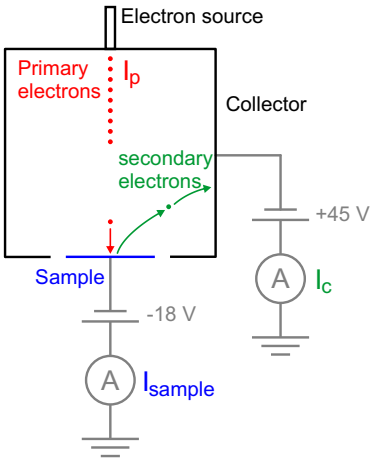

Figure 6.1.: CERN's SEY set-up.

$$\mathrm{SEY} = \frac{I_{\mathrm{secondary}}}{I_p} = \frac{I_c}{I_{\mathrm{sample}} + I_c} \tag{6.1}$$

All measurements are performed at room temperature, under ultra high vacuum $\left(< 10^{-8}\,\mathrm{mbar}\right)$ and with a low primary electron dose $\left(< 10^{-6}\,\mathrm{C/mm^2}\right)$.

6.1. Bulk Niobium (Nb)

In the literature, values for the SEY of Nb can be found to be around 1.3 [186, 187]. Most of the SEY data goes back to the 1930's although there is some available from the 1980's. In either cases, the information on the quality of the niobium along with the surface preparation is incomplete or even unavailable. Additionally, these studies focused on the SEY of the pure metal, not of the metal with a technical surface, i.e. a surface with its native oxide as well as hydrocarbons from air exposure.

[1] X-ray photoelectron spectroscopy

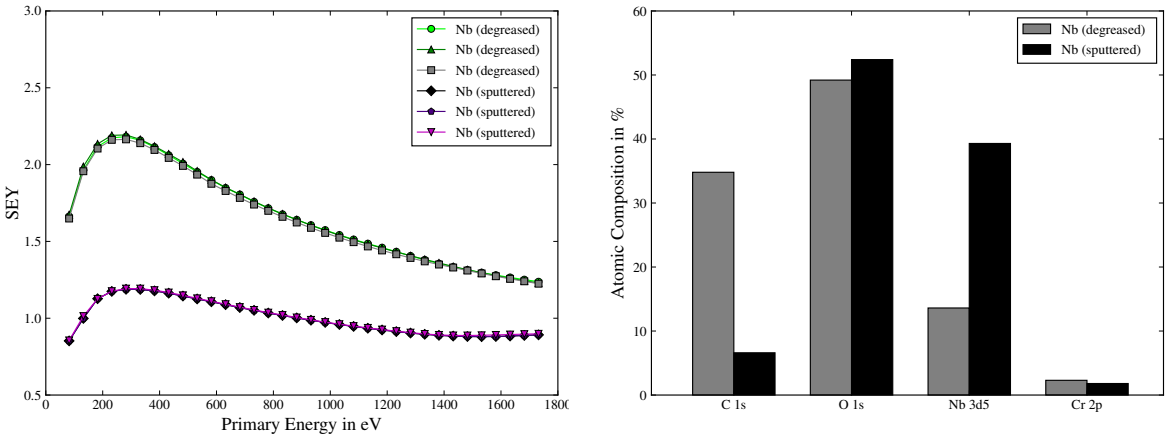

(a) (b)

Figure 6.2.: SEY (a) and chemical composition (b) of an EP finished bulk niobium sample before and after sputtering.

Therefore, the surfaces were sputter cleaned to remove the oxide layer as and any adsorbates so that the SEY of the pure metal could be determined. For accelerator applications these data have to be considered with cautions as the SEY of a clean technical surface will always differ from the pure material.

A technical niobium surface can be assumed to be a layered system of pure niobium covered with a few nm of different niobium oxides, in particular niobium pent-oxide Nb_2O_5, plus a layer of hydrocarbon including water molecules embedded into the hydrocarbons [133]. The thickness of the latter strongly depends on the handling, time of air exposure, chemical treatment of the surface and heat treatment. Reference [133] estimates a secondary electron escape depth for metals in the range of 3 nm to 5 nm. Considering an oxide layer of a few nm thickness and a contamination layer in the order of 1 nm , the SEY will be strongly influenced by the surface condition and will be a superposition of the SEY values of the different components. The secondary electron yield of the pure niobium oxides NbO, NbO_2 and Nb_2O_5 were found to be lower than the one for pure niobium, with SEY $\leq$ 1.2 [187]. Also the SEY for pure niobium carbide powder and niobium nitride powder were found to be 0.8 and the authors of Reference [187] estimate an SEY increase of 20 % to 25 % for bulk material. Auger electron spectra indicate the transformation of hydrocarbons to niobium carbide during heat treatments above 300 °C [133]. Despite the low SEY values for the common niobium compounds, the SEY of technical metal surfaces, particularly of niobium surfaces, are reported to be higher than for atomically clean niobium or its oxides [131, 133, 188]. This is contributed to the organic contamination layer and water adsorbed on the surface. The SEY of water was estimated to 2.3 by condensing 200 monolayers of water molecules on a liquid nitrogen cooled surface [131]. A SEY determination for hydrocarbons is not possible because it would be necessary to grow or condense a layer of hydrocarbons thick enough to neglect any influence of the substrate. However, the SEY can be estimated by comparing the SEY of insulators and metals and how it changes between atomically clean and technical surface: The SEY of metals increases under the influence of hydrocarbons (and water). But for insulators the SEY decreases in the presence of hydrocarbons. From this, one can conclude that the SEY of hydrocarbons is ranging

between pure metals and pure insulators [133].

On the surface of an SRF cavity, one has to assume that besides the pure niobium also niobium oxides, hydrocarbons and condensed water will be present.

For an SRF cavity representative reference, a sample from RRR 300 niobium sheet was prepared with a bulk electro-polishing of 200 µm, in order to expose the material to a typical chemical treatment and create a representative surface roughness. Afterwards, the sample was again degreased to reduce the amount of hydrocarbons on the surface. On this sample, the SEY was measured on three spots on the surface and an XPS spectrum was recorded. The surface was then sputter cleaned until the carbon peak vanished and XPS and SEY measurements were repeated. Both measurements are displayed in Figure 6.2 and serve as a baseline for the SEY measurements on alternative SRF materials.

The chemical composition reveals besides niobium also carbon, oxygen and a small contamination with chromium which most likely came from tooling. Also clean metallic Cr is reported with a low SEY (1.1 [189]). The relatively high SEY can therefore be explained by the presence of hydrocarbons and water on the surface. Following the XPS, the surface was sputter cleaned until the carbon peak in the XPS spectrum disappeared. Based on the sputtering rate, a total removal of 3 to 5 nm was estimated. After the sputtering, the XPS data shows significantly less carbon and a reduction of niobium oxides. The latter is concluded from the shift of the niobium peaks in the XPS spectrum towards lower binding energies. The SEY measurement following the sputtering shows a significant reduction of secondary electron emission and agrees well with the literature values for Nb and its native oxides.

6.2. Niobium Titanium Nitride (NbTiN)

NbTiN qualifies as a candidate for SRF cavities due to its high T_c and low normal resistance [190] and has recently re-gained attention at Jefferson Lab as a potential superconductor for multilayer systems as described in Section 2.2.2.

For the SEY measurement, Jefferson Lab kindly provided a 100 nm thick NbTiN film on a bulk Nb substrate. In contrast to the multilayer structures, the film was deposited via HIPIMS instead of dc reactive sputtering which is expected to result in denser films [73].

Prior to the SEY measurement, the sample was degreased to reduces surface contamination. The SEY was then measured in three different locations across the sample surface. The measured curves were as similar as for the bulk Nb sample shown in Figure 6.2a, so only one representative SEY curve is shown in Figure 6.3a to increase readability. The SEY measurement was followed by an XPS measurement. The surface was then sputter cleaned until the carbon peak disappeared then transferred back to the SEY chamber for an additional SEY measurement.

The atomic composition calculated from the XPS spectra is shown in Figure 6.3b. As can be seen, only carbon, oxygen and the film constituents are present on the surface. The secondary electron emission of the NbTiN film is before and after sputtering almost identical to the bulk Nb. This is due to the fact that niobium, the niobium oxides and niobium nitride have similar and low SEY and that the surface is (even after sputtering) dominated by the niobium compounds. It can therefore be expected that NbTiN would show the same multipacting activity as bulk Nb.

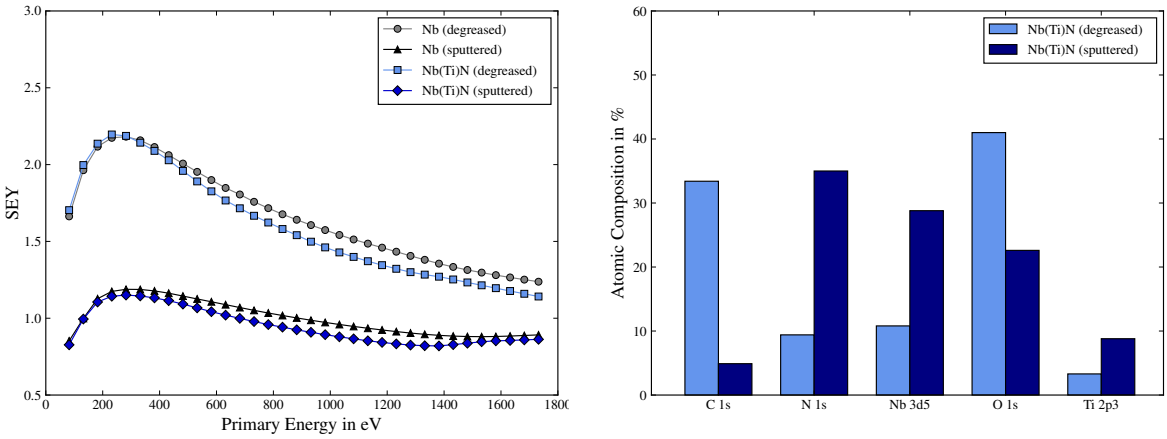

(a) (b)

Figure 6.3.: SEY measurement compared to bulk Nb (a) and chemical composition of the surface (b) of the NbTiN sample before and after sputtering.

6.3. Niobium-Tin (Nb_3Sn)

Nb_3Sn is the most advanced SRF material beyond niobium. Recent success was made at the Cornell University, by coating a 1.3 GHz single cell niobium cavity with Nb_3Sn via vapour diffusion based on the *Wuppertal recipe* [47].

The shape of the cell follows the Cornell ERL design and is very similar to the TESLA shape, for which extensive multipacting simulations and data exist. As far as multipacting is concerned TESLA, low loss and re-entrant shaped cavities are comparable [3] and experience gained on TESLA cavities can serve as a good reference. The first two point multipacting band is calculated to be at 21 MV/m with a width of a few MV/m [191] and agrees well with multipacting observations in the range of 17 MV/m to 22 MV/m [3, 191, 192]. The Nb_3Sn cavity reaches a maximum gradient of about 13 MV/m and stays well below the multipacting band.

The Nb_3Sn sample used for these SEY studies was kindly prepared by the Cornell group in the same way as the cavity and represents therefore the properties of this specific Nb_3Sn coating. Figure 6.4 shows a representative SEY measurement and the chemical composition of the described sample. The sample appears as clean as the niobium reference, but the SEY is slightly higher with a maximum value of 2.4. Nb_3Sn is very resistant against oxidation; however no SEY data is available on SnO_2. The higher SEY could therefore be caused by this or another oxidation state of tin or by more/different hydrocarbon content on the surface. After sputtering, the SEY decreases to almost the same level as Nb and NbTiN. Significantly severer multipacting activity is therefore not expected for Nb_3Sn cavities.

6.4. Magnesium Diboride (MgB_2)

High quality magnesium diboride (MgB_2) coatings were successfully produced by reactive evaporation [53] at Superconductor Technology Inc. (STI) and hybrid physical–chemical vapour deposition [54] at Temple University on various substrates. STI generously coated 500 nm MgB_2 onto a 75 mm big sample

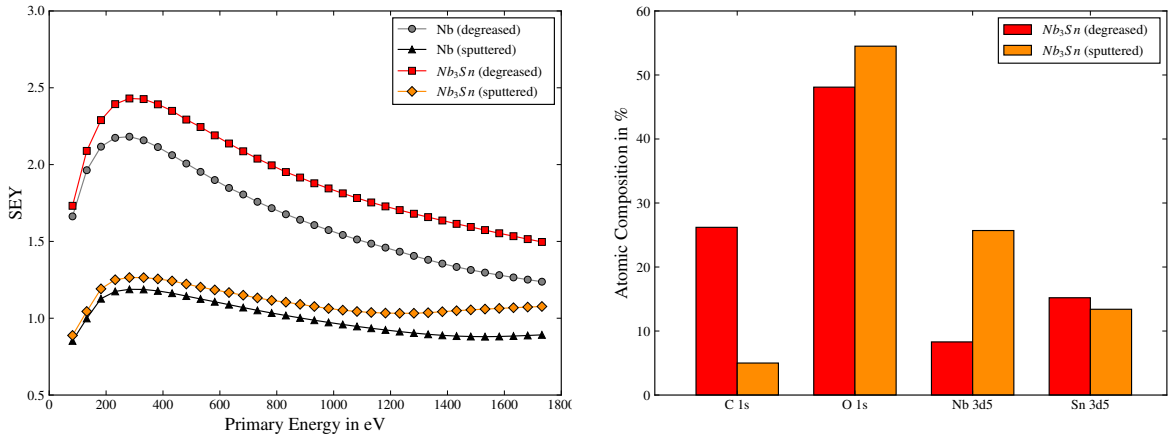

(a) (b)

Figure 6.4.: SEY measurement compared to bulk Nb (a) and chemical composition of the surface (b) of the Nb_3Sn sample before and after sputtering.

for the Quadrupole Resonator. An electro-polished reactor grade bulk niobium sample was prepared at CERN and served as the substrate. In order to minimise the degradation of the MgB_2 under humidity, the sample was stored under nitrogen atmosphere and rinsed with ethanol instead of water. The first RF cold test showed strong electron loading which made reasonable surface resistance measurements impossible. The electron loading even worsened after dismounting and newly (ethanol) rinsing. After the second cold test, the MgB_2 coating exhibited visible damage in the regions of highest electric surface field as shown in Figure 6.5b.

A main difference between the SRF set-ups used for characterising MgB_2 samples at Jefferson Lab and MIT and the Quadrupole Resonator is that in the Quadrupole Resonator the sample surface is exposed to not only magnetic but also electric fields. This circumstance in combination with the different RF performances demanded measuring the SEY on pure, clean MgB_2 to distinguish intrinsic from extrinsic cause.

As STI had discontinued their MgB_2 activities in the meantime, the Temple University kindly provided two small, clean and pure MgB_2 samples for SEY measurements at CERN.

Figure 6.6 shows the SEY for these samples in comparison with bulk Nb and their chemical composition as calculated from the XPS spectra. To avoid contamination of the vacuum chamber with boron, no sputter cleaning was performed. As for the previous samples, the SEY was measured in three different spots but only one representative curve is shown in Figure 6.6a. The SEY values of 2.6 (1080c) and 2.7 (1080d) are about 20 % higher than for Nb.

From the XPS multiplex can be seen that both samples are very clean, which supports that the SEY of the actual sample is measured and not any unusual contamination on the surface. The little higher SEY for sample 1018d is consistent with the higher amount of carbon on the surface. Moreover, the XPS data reveals a similar oxygen content as for the other samples. The effect on the SEY is however different. While the niobium oxides have low SEY, the SEY of magnesium oxide MgO ranges from 4 to 10. In fact, dynodes in photomultipliers are often coated with MgO due to its high secondary electron yield

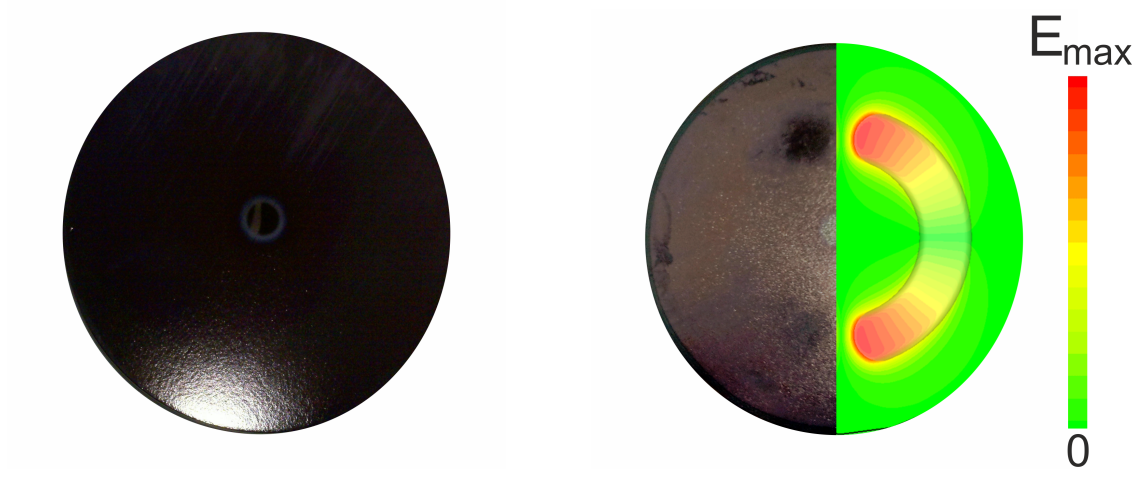

(a) (b)

Figure 6.5.: Photo of the Quadrupole Resonator MgB_2 sample after coating (a) and after the second cold test (b).

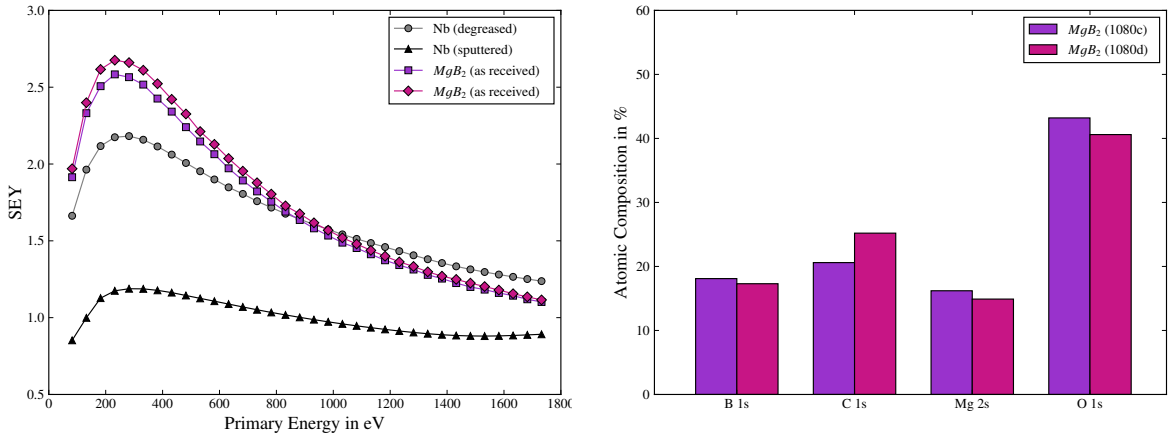

(a) (b)

Figure 6.6.: SEY measurement compared to bulk Nb (a) and chemical composition of the surface (b) of the MgB_2 samples 1080c and 1080d.

[193]. Due to the reported very high SEY of MgO, the SEY of the MgB_2 samples may be attributed not only to hydrocarbons and water but also to the presence of MgO.

MgB_2 is known to degrade under humidity, resulting in the formation of MgO. The presence of a significant amount of MgO makes bare MgB_2 unsuitable for any RF exposed surface unless a passivation layer prevents the formation of MgO. A thickness of few nanometers is considered to be sufficient but the protection layer needs to have low RF power dissipation as it will be exposed and fully penetrated by the RF. The combination of low SEY and low RF losses is very restrictive to potential materials: Insulators have usually high SEY values. Metals have low SEY but either a normal resistance or in case of superconductors, the critical field limits the maximum accelerating gradient. MgB_2 still remains a candidate for SRF multilayer structures given that the RF exposed surface is a different material.

7. Summary and Conclusion

The Quadrupole Resonator (QPR) is the ideal tool for systematic studies of the SRF properties of a given sample. Previous work covered RF simulations, the refurbishment of the 400 MHz operation and the extension to 800 MHz and 1200 MHz [92] while for this thesis the QPR was further upgraded, additional aspects have been simulated and the first energetically condensed niobium film has been extensively studied.

Thermal Simulations

Within this thesis, thermal effects were simulated to give insight regarding the cooling dynamics of a QPR sample which are currently not accessible through measurements. In particular, the temperature gradients across the sample and its dependency on the cool down rate have been studied. It could be shown that in contrast to SRF cavities slow cooling of the QPR geometry leads to higher temperature gradients across the sample surface. Quantifying the temperature gradient depends on the thermal conductivity of the sample: For reactor grade bulk niobium the temperature gradient can be as high as 12 K/m while about 1 K/m can be achieved for niobium on copper films.

Additionally, the superconducting transition was simulated. The simulation reveals that a bulk niobium sample is most likely to trap magnetic flux on the bottom side of the sample center which is the last area to become superconducting and which is not exposed to the RF. For a Nb/Cu sample flux trapping can be expected in the sample center which is exposed to the RF as well as at the interface between niobium and copper which is not directly exposed to the RF but is in very close vicinity (given by the film thickness).

Upgrades

Two hardware upgrades have been implemented to the QPR. Firstly, the QPR was extended with a solenoid to apply DC magnetic fields to the sample surface. This upgrade enables studying the influence of trapped magnetic flux on the surface resistance. The corresponding field distributions were simulated taking into account shielding from superconducting parts in the vicinity of the RF surface. A cryogenic magnetic field probe was additionally installed so that the ambient magnetic fields could be monitored and compared to the simulation results and linked to SRF performance.

Secondly, a new thermometry chamber was designed to enable the SRF characterisation of flat, thin samples. This shall facilitate collaborations by resolving one disadvantage of the QPR: a sample thickness of 12 mm which is 4 times as thick as typical high grade niobium sheets and typically not available. The new design relies on pressing the temperature sensors and the heater against the underside of the sample in contrast to screwing both directly onto the underneath surface. The new chamber is also equipped with a magnetic field coil and a cryogenic magnetic field probe for trapped flux studies and

was commissioned with a thin bulk niobium sample. This sample however shows evidence of contamination due to an unsuccessful nitrogen doping process. A full commissioning of the new thermometry chamber will require validation with a plain bulk niobium sample with standard surface preparation.

RF Characterisation

This thesis presents the first SRF performance results of a niobium thin film on copper which was deposited by the electron cyclotron resonance (ECR) technique, which belongs to the class of energetic condensation techniques. Surface analysis techniques such as SEM, EBSD, FIB and EDS reveal a high quality film microstructure with a very smooth niobium-copper interface and no visible porosity.

Although the low field superconducting properties, like the superconducting energy gap, the electron mean free path and superheating field are comparable to a reactor grade bulk niobium reference, the RF performance is still different: The residual resistance of the ECR coating is not only higher but also increases much stronger with frequency although the frequency dependence matches typical bulk niobium. Moreover, the residual resistance retains the for niobium films typical low sensitivity to trapped magnetic flux and the strong dependence on the cool down dynamics. It was found that the residual resistance decreases with faster cooling which translates to smaller temperature gradients across the sample. Furthermore, there is a clear positive correlation between residual resistance and Q-slope, i.e. the increase of surface resistance with RF magnetic field becomes stronger for higher residual resistance. Combining the results of the trapped flux and the cooling dynamics studies indicates that trapped flux from the ambient field can not explain the increase of surface resistance for larger temperature gradients. This suggests a different mechanism than just a change in flux expulsion efficiency. It can be speculated that thermal currents are created at the niobium-copper interface and therefore in proximity to the RF surface, inducing strong magnetic fields in the film which are trapped and contribute to the surface resistance. Due to the low trapped flux sensitivity, these fields would need to be in the order of 1 mT.

The magnetic field dependence of the ECR coating at 2.5 K and 4 K follows the Nb/Cu-typical exponential increase but comparison with sputter coated cavity data shows strong mitigation of the Q-slope. This is particularly true for a comparison with LEP and LHC data where both cavity geometries have similar resonance frequency. However, the increase with field is still stronger than for the reactor grade bulk niobium. From this it can be concluded that the lower mean free path in Nb/Cu films is not the defining factor for their RF performance.

The thermal boundary resistance model offers an explanation to the differences in RF performance: The QPR provides RF characterisation at different frequencies and temperatures without changing the cooling properties, which allows testing the thermal boundary resistance model for consistency. The comparison of different data sets from the ECR coating and the bulk niobium strongly supports the applicability of the model. The model yields a fraction of detached surface area which is an order of magnitude lower than the best sputtered cavities. This is in line with the findings that the studied coating is dense and well adhered and reinforces the expectation that energetic condensation deposition techniques create denser and better adhered coatings compared to sputtered coatings in general.

A direct comparison of the ECR data with other Nb/Cu data suggests that the exponential surface resistance increase with field does not depend on frequency but on temperature. The temperature de-

pendence suggests that thermal effects play a role while the deconvolution from the BCS and residual part allows quantitative comparison of coatings throughout different projects and frequencies.

In conclusion can be stated that this ECR coating shows significantly improved RF performance compared to sputter coated niobium films which proves the superiority of energetic condensation techniques over standard sputtering. The combination of material analyses with the low RF field behaviour, analysis of the Q-slope and the trapped flux sensitivity implies that the grain boundaries and/or the niobium-copper interface are still not as dense as in bulk niobium. It can also be concluded that the Q-slope in Nb/Cu films is not directly caused by the lower RRR values. Further improvement towards a denser microstructure and perfect adhesion to the substrate promises to cure the Q-slope but might also result in a higher trapped flux sensitivity. Nonetheless, the trapped flux sensitivity remains relatively small for medium RRR and low frequency cavities so that unshielded cavities might be still beneficial after considering the costs for magnetic shielding and the resulting additional complexity of a cryomodule design.

Trapped Flux Sensitivity

This thesis offers an extended model to estimate the trapped flux sensitivity of bulk niobium taking into account the losses in the normal core of a trapped flux line, the trapping efficiency and the depinning behaviour as function of frequency, RRR and the size of the pinning center. It also offers a qualitative explanation for the significantly different trapped flux sensitivities of nitrogen doped and 120 °C baked cavities and Nb/Cu films.

Secondary Electron Yield of New SRF Materials

The quest for SRF materials beyond niobium require to address multipacting as a potentially reoccurring performance limitation. A set of measurements has been performed to measure the SEY of the most promising candidates currently under development. The study of the technical surfaces of the niobium compounds, Nb_3Sn and Nb(Ti)N, shows comparable SEY values to niobium. Moreover, the atomically clean materials, i.e. without hydrocarbons on the surface, show similar behaviour than clean niobium. This is most likely due to the similar oxidation states as all niobium oxides have low SEY values.

MgB_2 is know to degrade when exposed to air. The formation of MgO on the surface will increase the SEY of an originally MgB_2 surface dramatically and an RF exposed surface might suffer severe damage from electron loading as has been observed on a QPR sample. It can be concluded that bare MgB_2 is unsuitable for an RF exposed surface and a passivation layer has to be found which combines low electrical resistivity with a low SEY value.

8. Outlook

The Quadrupole Resonator remains the unrivaled test system for systematic SRF material studies. Since this work has been done, first data on other material systems, such ans Nb_3Sn and NbTiN became available [194]. As a follow-up to the work in this thesis, the performance of the Nb/Cu coating was repeated on the full sample holder avoiding EBW after coating. It shows no major impact of the welding and proves reproducibility [195].

The future niobium film development should focus on understanding the role of the grain boundaries and the niobium-copper interface. To gain further insight regarding the role of the films microstructure, the same coating, i.e. a coating with the same coating parameters, should be deposited onto two different OFE copper substrates: Depositing the same coating on OFE copper with large (cm^2) grains might give insights regarding the role of the number and density of grain boundaries. Secondly, the same coating should be deposited onto oxidised OFE fine grain copper to study the impact of the substrate surface on the SRF performance. In the past, the 1.5 GHz DCMS cavities showed better performance when coated on oxidised copper in contrast to coating on the clean metallic (oxide free) surface. This is contrary to the expectations since the copper oxide layer is amorphous and results in fibre growth with smaller and less well connected grains in the niobium film. One possible explanation is that the copper oxide serves as a diffusion barrier which protects the growing niobium film from pollution through the bulk copper. It should be investigated if also energetically condensed films will yield better RF results when deposited on amorphous copper oxide. Optimisation of the coating parameters shall then be done on the most suitable substrate.

For all cases, additional material characterisations shall provide information about thickness and degree of oxidation of the surface, grain boundaries and interface. Also the intermixing of copper and niobium at the interface, the porosity and the segregation of hydrogen and the formation of niobium hydrides may be studied and correlated with the RF results. Moreover, the field of first flux penetration may be subject to a thorough investigation, and a link between DC and RF measurements would be of great benefit.

From an operational point of view, the effect of cool down dynamics need further investigation: Especially identifying the cause of the strong influence of the thermal gradient is crucial to ensure optimal performance also in a cryomodule respectively an accelerator.

Since ECR is only one of several energetic condensation techniques, the same studies should be performed on HIPIMS and CAD films. This should also allow at some point rating these techniques among each other and find the most suitable for SRF cavity production.

Finally, all coating techniques have to be demonstrated on a 3D structure.

Appendix

A. Cryogenic Infrastructure

Figure A.1 shows the cryogenic infrastructure in CERN's central cryogenic laboratory. The Quadrupole Resonator is immersed in a 150 litre liquid helium bath cryostat with connections for pumping the cavity vacuum, the isolation vacuum of the thermometry chamber, and the helium bath in order to decrease the boiling point of the helium. The cryostat is refilled from a liquid helium dewar.

The helium pumping line is equipped with a butterfly valve and a pressure gauge on top of the top plate of the cryostat. A PID controller regulates the opening of the butterfly valve in order to stabilize the helium pressure to a set reference point. For reference pressures below the λ-point (50 mbar), the liquid helium pressure can be stabilized to $\pm 10\,\mu$bar which corresponds to temperature fluctuations of less than 1 mK.

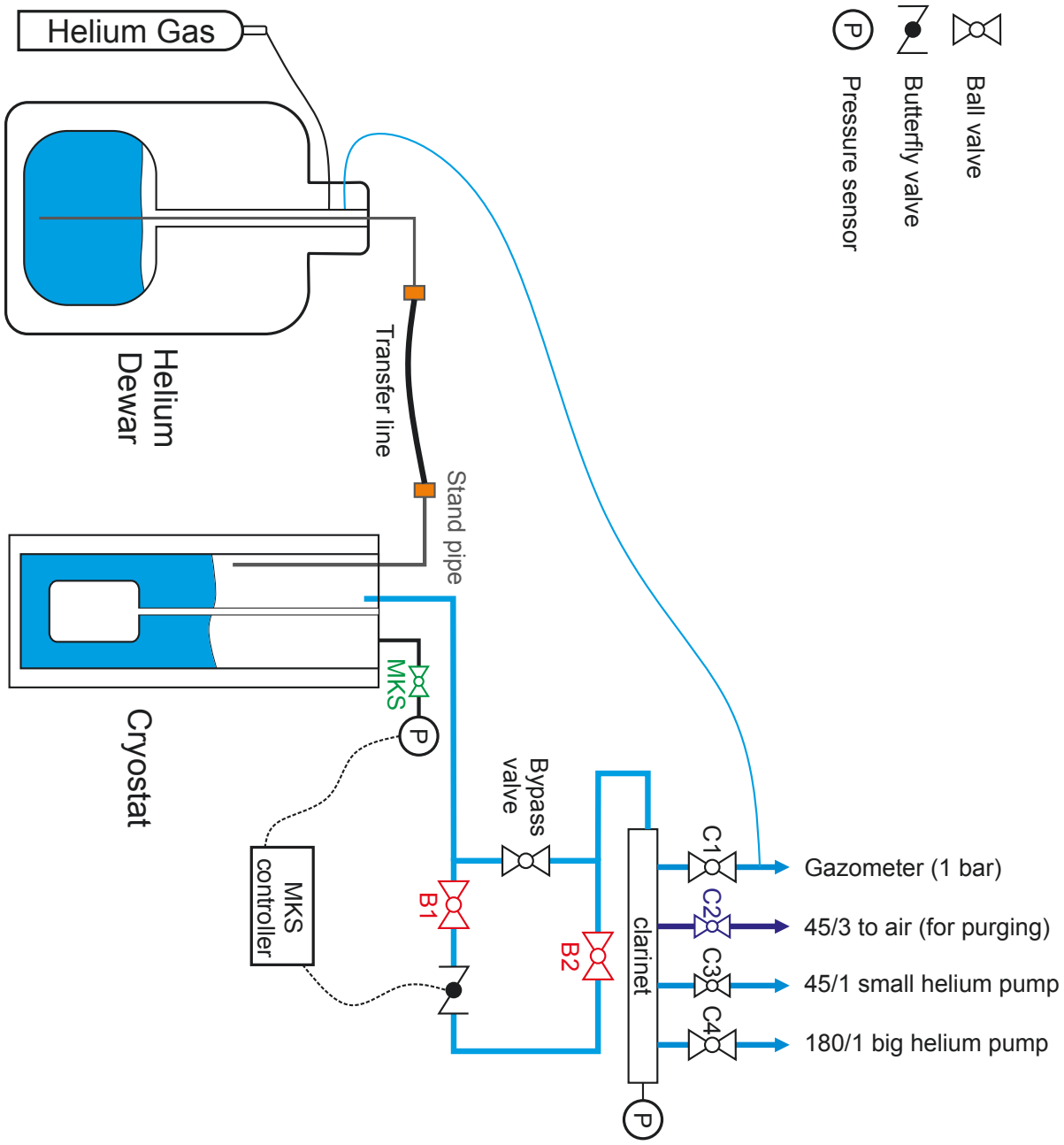

Figure A.1.: Cryogenic infrastructure in CERN's central cryogenic laboratory. Not to scale.

Bibliography

[1] L. Tavian. Cryogenics Expert, Private Communication, 2017. 1

[2] LEP Design Report, Vol. 3 : LEP2. Technical report, CERN, Geneva, Switzerland, 1996. Vol. 1-2 publ. in 1983-84. 2, 14, 89

[3] R.L. Geng. Review of New Shapes for Higher Gradients. *Physica C: Superconductivity*, 441(1-2):145–150, July 2006. 6, 110

[4] R.L. Geng, G.V. Eremeev, H. Padamsee, and V.D. Shemelin. High Gradient Studies for ILC with Single-Cell Re-entrant Shape and Elliptical Shape Cavities Made of Fine-Grain and Large-Grain Niobium. In *Proceedings of the 22nd Particle Accelerator Conference*, pages 2337–2339, Albuquerque, USA, June 2007. 6

[5] Z.A. Conway, E.P. Chojnacki, D.L. Hartill, M.U. Liepe, D.J. Meidlinger, and H.S. Padamsee. Multi-Cell Reentrant Cavity Development and Resting at Cornell. In *Proceedings of the 23rd Particle Accelerator Conference*, pages 930–932, Vancouver,Canada, May 2009. 6

[6] B. Aune, R. Bandelmann, D. Bloess, B. Bonin, A. Bosotti, M. Champion, C. Crawford, G. Deppe, B. Dwersteg, D.A. Edwards, H.T. Edwards, M. Ferrario, M. Fouaidy, P.-D. Gall, A. Gamp, A. Gössel, J. Graber, D. Hubert, M. Hüning, M. Juillard, T. Junquera, H. Kaiser, G. Kreps, M. Kuchnir, R. Lange, M. Leenen, M. Liepe, L. Lilje, A. Matheisen, W.-D. Möller, A. Mosnier, H. Padamsee, C. Pagani, M. Pekeler, H.-B. Peters, O. Peters, D. Proch, K. Rehlich, D. Reschke, H. Safa, T. Schilcher, P. Schmüser, J. Sekutowicz, S. Simrock, W. Singer, M. Tigner, D. Trines, K. Twarowski, G. Weichert, J. Weisend, J. Wojtkiewicz, S. Wolff, and K. Zapfe. Superconducting TESLA Cavities. *Physical Review Special Topics – Accelerators and Beams*, 3:1–25, 2000. 6, 9, 81

[7] G. Ciovati. Where Next with SRF? In *Proceedings of the 4th International Particle Accelerator Conference*, pages 3124–3128, Shanghai, China, 2013. THYB201. 7

[8] L. Ferreira. Electro-Polishing for Superconducting Cavities. Presentation at the *B2FiftyTwo Seminar* (CERN internal), January 2014. 7

[9] G. Issarovitch, D. Proch, X. Singer, D. Reschke, and W. Singer. Development of Centrifugal Barrel Polishing for Treatment of Superconducting Cavities. In *Proceedings of the 11th International Workshop on RF Superconductivity*, pages 482–485, Lübeck/Travemünde, Germany, 2003. 7

[10] C. Cooper, B. Bullock, S. Joshi, and A. Palczewski. Centrifugal Barrel Polishing of Cavities Worldwide. In *Proceedings of the 15th International Conference on RF Superconductivity*, pages 571–575, Chicago, USA, 2011. 7

[11] C.A. Cooper and L.D. Cooley. Mirror-Smooth Surfaces and Repair of Defects in Superconducting RF Cavities by Mechanical Polishing. *Superconductor Science and Technology*, 26(1):015011, January 2013. doi 10.1088/0953-2048/26/1/015011. 7, 11

[12] A.D. Palczewski, C.A. Cooper, B. Bullock, S. Joshi, A.A. Rossi, and A. Navitski. R&D Progress in SRF Surface Preparation With Centrifugal Barrel Polishing (CBP) for Nb and Cu. In *Proceedings of the 16th International Workshop on RF Superconductivity*, pages 398–403, Paris, France, 2013. 9

[13] C. Benvenuti, S. Calatroni, I.E. Campisi, P. Darriulat, M.A. Peck, R. Russo, and A.-M. Valente. Study of the Surface Resistance of Superconducting Niobium Films at 1.5 GHz. *Physica C: Superconductivity*, 316(3):153–188, 1999. 9, 23, 37, 77, 89, 98

[14] G. Ciovati. Effect of Low-temperature Baking on the Radio-Frequency Properties of Niobium Superconducting Cavities for Particle Accelerators. *Journal of Applied Physics*, 96:1591, 2004. 9, 80, 104

[15] F. Barkov, A. Romanenko, Y. Trenikhina, and A. Grassellino. Precipitation of hydrides in high purity niobium after different treatments. *Journal of Applied Physics*, 114(16):164904, 2013. 9

[16] A. Grassellino, A. Romanenko, D. Sergatskov, O. Melnychuk, Y. Trenikhina, A. Crawford, A. Rowe, M. Wong, T. Khabiboulline, and F. Barkov. Nitrogen and Argon doping of Niobium for Superconducting Radio Frequency Cavities: a Pathway to Highly Efficient Accelerating Structures. *Superconductor Science and Technology*, 26(10):102001, October 2013. 9, 29

[17] A. Grassellino. N Doping: Progress in Development and Understanding. Conference Talk on the 17th International Conference on RF Superconductivity, September 2015. `http://srf2015proc.triumf.ca/prepress/talks/moba06_talk.pdf`. 9

[18] Y. Trenikhina. Nanostructure of the Penetration Depth in Nb Cavities: Debunking the Myths and New Findings. Conference Talk on the 17th International Conference on RF Superconductivity, September 2015. `http://srf2015proc.triumf.ca/prepress/talks/wea1a05_talk.pdf`. 10

[19] S. Aull, O. Kugeler, and J. Knobloch. Trapped Magnetic Flux in Superconducting Niobium Samples. *Physical Review Special Topics - Accelerators and Beams*, 15(6):062001, June 2012. 10, 37, 91, 103

[20] O. Kugeler, A. Neumann, S. Voronenko, W. Anders, J. Knobloch, M. Schuster, A. Frahm, S. Klauke, D. Pflueckhahn, and S. Rotterdam. Manipulating the Intrinsic Quality Factor by Thermal Cycling and Magnetic Fields. In *Proceedings of the SRF'09*, pages 352–354, Berlin, Germany, 2009. 10

[21] A. Romanenko, A. Grassellino, O. Melnychuk, and D.A. Sergatskov. Dependence of the Residual Surface Resistance of Superconducting Radio Frequency Cavities on the Cooling Dynamics Around T_c. *Journal of Applied Physics*, 115(18):184903, May 2014. 10, 103

[22] M. Martinello, M. Checchin, A. Grassellino, A. C. Crawford, O. Melnychuk, A. Romanenko, and D. A. Sergatskov. Magnetic Flux Studies in Horizontally Cooled Elliptical Superconducting Cavities. *Journal of Applied Physics*, 118(4):044505, July 2015. 10, 91

[23] J.-M. Vogt, O. Kugeler, and J. Knobloch. Impact of Cool-Down Conditions at T_{c} on the Superconducting RF Cavity Quality Factor. *Physical Review Special Topics - Accelerators and Beams*, 16(10), October 2013. 10, 91, 103

[24] J.-M. Vogt, O. Kugeler, and J. Knobloch. High Q Operation of Superconducting RF Cavities: Potential Impact of Thermocurrents on the RF Surface Resistance. *Physical Review Special Topics - Accelerators and Beams*, 18(4), April 2015. 10, 91, 98

[25] C.Z. Antoine. How to Achieve the Best SRF Performance: (Practical) Limitations and Possible Solutions. In R. Bailey, editor, *Proceedings of the CERN Accelerator School: Superconductivity for Accelerators*, CERN Yellow Report, pages 209–246. CERN, Erice, Italy, 24 april - 04 may 2013 edition, July 2014. 10

[26] U.S. Geological Survey. Minerals Yearbook: Niobium and Tantalum, 2012. `http://minerals.usgs.gov/minerals/pubs/commodity/niobium/myb1-2012-niobi.pdf`. 10

[27] British Geological Survey. Niobium, Tantalum, April 2011. by the Natural Environment Research Council. 10

[28] Frank Marhauser. JLab SRF Cavity Fabrication Errors, Consequences and Lessons Learned. In *Proceedings of the 2nd International Particle Accelerator Conference*, pages 346–348, San Sebastian, Spain, 2011. 11

[29] S. Aderhold. Optical Inspection of SRF Cavities at DESY. In *Proceedings of the 14th International Conference on RF Superconductivity*, pages 286–288, Berlin, Germany, 2009. 11

[30] M.S. Champion, L.D. Cooley, C.M. Ginsburg, D.A. Sergatskov, R.L. Geng, H. Hayano, Y. Iwashita, and Y. Tajima. Quench-Limited SRF Cavities: Failure at the Heat-Affected Zone. *IEEE Transactions on Applied Superconductivity*, 19(3):1384–1386, June 2009. 11

[31] S. Posen, N. Valles, and M. Liepe. Quench Studies in Large and Fine Grain Nb Cavities. In *Proceedings of the 15th Conference on RF Superconductivity*, pages 714–717, Chicago, USA, 2011. 11

[32] S. Atieh, A. Amorim Carvalho, I. Aviles Santillana, F. Bertinelli, R. Calaga, O. Capatina, G. Favre, M. Garlasche, F. Gerigk, S.A.E. Langeslag, K.M. Schirm, N. Valverde Alonso, G. Avrillaud, D. Alleman, J. Bonafe, J. Fuzeau, E. Mandel, P. Marty, A. Nottebaert, H. Peronnet, and R. Plaut. First Results of SRF Cavity Fabrication By Electro-Hydraulic Forming at CERN.

In *Proceedings of the 17th International Conference on RF Superconductivity*, Whistler, Canada, September 2015. 11

[33] P. Frigola, R. Agustsson, L. Faillace, A. Murokh, G. Ciovati, W. Clemens, P. Dhakal, F. Marhauser, R. Rimmer, J. Spradlin, S. Williams, S. Mireles, P.A. Morton, and R.B. Wicker. Advance Additive Manufacturing Method for SRF Cavities of Various Geometries. In *Proceedings of the 17th International Conference on RF Superconductivity*, Whistler, Canada, 2015. 11

[34] M. Murakami and K. Harada. Experimental Study of Thermo-Fluid Dynamic Effect in He II Cavitating Flow. *Cryogenics*, 52(11):620–628, November 2012. 12, 59

[35] H. Padamsee, J. Knobloch, and T. Hays. *RF Superconductivity for Accelerators*. Wiley-VCH, 2 edition, 2008. 13, 38, 45, 47, 74, 98

[36] G. Ciovati and B.P. Xiao. *SUPERFIT: a Computer Code to Fit Surface Resistance and Penetration Depth of a Superconductor*. Technical Note TN-03-003. Jefferson Lab, 2010. 13

[37] J. Halbritter. *FORTRAN Program for the Computation of the Surface Impedance of Superconductors*. Technical Note KFK-Extern 3/70-6. Kernforschungszentrum Karlsruhe, 1970. 13

[38] C. Benvenuti, N. Circelli, and M. Hauer. Niobium Films for Superconducting Accelerating Cavities. *Applied Physics Letters*, 45(5):583–584, 1984. 13

[39] A.M. Porcellato, S.Y. Stark, G. Bassato, G. Bisoffi, S. Canella, A. Dainelli, A. Facco, V. Palmieri, M. Poggi, V. Zviagintsev, L. Bertazzo, S. Contran, F. Stivanello, L. Boscagli, D. Carlucci, L. Badan, A. Beltramin, T. Contran, M. De Lazzari, and F. Poletto. On Line Performance and Upgrading of ALPI Resonators. In *Proceedings of the 9th International Workshop on RF Superconductivity*, pages 174–178, Santa Fe, USA, 1999. 14

[40] S. Bauer, W. Diete, B. Griep, M. Peiniger, H. Vogel, P. vom Stein, S. Calatroni, E. Chiaveri, and R. Losito. Production of Nb/Cu Sputtered Superconducting Cavities for LHC. In *Proceedings of the 9th International Workshop on RF Superconductivity*, pages 437–439, Santa Fe, USA, 1999. 14, 89

[41] W. Venturini Delsolaro, S. Calatroni, B. Delaup, A. D'Elia, N.M. Jecklin, Y. Kadi, G. Keppel, D. Lespinasse, P. Maesen, I. Mondino, V. Palmieri, S. Stark, A. Sublet, and M. Therasse. Nb Sputtered Quarter Wave Resonators for the HIE-ISOLDE. In *Proceedings of the 16th International Conference on RF Superconductivity*, Paris, France, 2013. 14

[42] W. Venturini Delsolaro, L. Alberty, L. Arnaudon, K. Artoos, J. Bauche, A.P. Bernardes, J.A. Bousquet, E. Bravin, S. Calatroni, E.D. Cantero, O. Capatina, N. Delruelle, D. Duarte Ramos, M. Elias, F. Formenti, M.A. Fraser, S. Gayde, N.M. Giron, Y. Kadi, G. Kautzmann, Y. Leclercq, P. Maesen, V. Mertens, E. Montesinos, V. Parma, G.J. Rosaz, K.M. Schirm, E. Siesling, D. Smekens, A. Sublet, M. Therasse, D. Valuch, G. Vandoni, E. Vergara Fernandez, D. Voulot,

L.R. Williams, and P. Zhang. Status of the HIE-ISOLDE Linac. In *Proceedings of the 27th Linear Accelerator Conference*, pages 795–800, Geneva, Switzerland, 2014. 14

[43] G. Cavallari, C. Arnaud, M. Barranco-Luque, C. Benvenuti, P. Bernard, D. Bloess, Boussard, D., Brown, P., Calatroni, S., Chiaveri, E., Ciapala, E., Erdt, W., Frandsen, P., Genesio, F., Geschonke, G., Guesewell, H.P., Haebel, E., Hartung, W., Hauviller, C., Hilleret, N., Kindermann, H.P., Orlandi, G., Passardi, G., Peschardt, E., Roedel, V., Tueckmantel, J., Weingarten, W., and Winkler, G. Status Report on SC RF Cavities at CERN. In *Proceedings of the 5th International Workshop on RF Superconductivity*, pages 23–36, Hamburg, Germany, 1991. 14

[44] G. Fortuna, A. Lombardi, G. Bassato, A. Battistella, G. Bezzon, G. Bisoffi, S. Canella, M. Cavenago, F. Cervellera, F. Chiurlotto, M. Comunian, R. Cortese, A. Facco, P. Favaron, M.F. Moisio, V. Palmieri, R. Pengo, A. Pisent, M. Poggi, A.M. Porcellato, L. Ziomi, I. Kulik, A. Kolomiets, and S. Yaramishev. Status of ALPI and Related Developments of Superconducting Structures. In *Proceedings of the 18th International Linear Accelerator Conference*, pages 125–127, Geneva, Switzerland, August 1996. 14

[45] H Y Zhai, H M Christen, L Zhang, M Paranthaman, P H Fleming, and D H Lowndes. Degradation of superconducting properties in MgB_2 films by exposure to water. *Superconductor Science and Technology*, 14(7):425–428, July 2001. 17

[46] M. Peiniger. *Nb_3Sn Herstellung mit Dampfphasendiffusion*. Dissertation, Bergische Universität Wuppertal, 1989. 17

[47] G. Müller, P. Kneisel, D. Mansen, H. Piel, J. Pouryamout, and R.W. Röth. Nb_3Sn Layers on High-Purity Nb Cavities With Very High Quality Factors and Accelerating Gradients. In *Proceedings of the 5th European Particle Accelerator Conference*, pages 2085–2087, Barcelona, Spain, 1996. 17, 110

[48] S. Posen and M. Liepe. RF Test Results of the First Nb_3Sn Cavities Coated at Cornell. In *Proceedings of the 16th International Conference on RF Superconductivity*, pages 660–663, Paris, France, 2013. 17

[49] A.-M. Valente-Feliciano. *Development of SRF Monolayer/Multilayer Thin Film Materials to Increase the Performance of SRF Accelerating Strucutres Beyond Bulk Nb*. PhD Thesis, Université Paris-Sud, Paris, France, September 2014. 17, 25, 26, 71

[50] R. Vaglio. Alternative Superconducting Materials for R.F. Cavity Applications. *Particle Accelerators*, 61:127–136, 1998. 17

[51] M. Juillard, B. Aune, B. Bonin, and L. Wartski. Superconducting Surface Resistance Measurements with a TE011 Cavity. In *Proceedings of the 2nd European Particle Accelerator Conference*, pages 1106–1108, Nice, France, 1990. 17

[52] P. Bosland, S. Cantacuzene, J. Gobin, M. Juillard, and J. Martignac. NbTiN Thin Films for RF Applications. In *Proceedings of the 6th European Particle Accelerator Conference*, pages 1028–1032, Newport News, USA, October 1993. 18

[53] B.H. Moeckly and W.S. Ruby. Growth of High-Quality Large-Area MgB_2 Thin Films by Reactive Evaporation. *Superconductor Science and Technology*, 19(6):L21–L24, June 2006. 18, 110

[54] X.X. Xi, A.V. Pogrebnyakov, S.Y. Xu, K. Chen, Y. Cui, E.C. Maertz, C.G. Zhuang, Q. Li, D.R. Lamborn, J.M. Redwing, Z.K. Liu, A. Soukiassian, D.G. Schlom, X.J. Weng, E.C. Dickey, Y.B. Chen, W. Tian, X.Q. Pan, S.A. Cybart, and R.C. Dynes. MgB_2 Thin Films by Hybrid Physical-Chemical Vapor Deposition. *Physica C: Superconductivity*, 456(1-2):22–37, June 2007. 18, 110

[55] T. Tajima, L. Civale, N.F. Haberkorn, R.K. Schulze, V.A. Dolgashev, J. Guo, D.W. Martin, S.G. Tantawi, C. Yoneda, H. Inoue, A. Matsumoto, E. Watanabe, B.H. Moeckly, C. Yung, M.J. Pellin, T. Proslier, X. Xi, and B.P. Xiao. MgB_2 Thin Film Studies. In *Proceedings of the 15th International Conference on RF Superconductivity*, pages 287–292, Chicago, USA, 2011. 18

[56] H. Xin, Daniel E. Oates, A.C. Anderson, R. L. Slattery, G. Dresselhaus, and M.S. Dresselhaus. Comparison of Power Dependence of Microwave Surface Resistance of Unpatterned and Patterned YBCO Thin Film. *IEEE Transactions on Microwave Theory and Techniques*, 48(7):1221–1226, 2000. 18

[57] D.E. Oates, Y.D. Agassi, and B.H. Moeckly. Microwave Measurements of MgB_2: Implications for Applications and Order-Parameter Symmetry. *Superconductor Science and Technology*, 23(3):034011, March 2010. 18

[58] B. Xiao, R. Geng, M.J. Kelley, F. Marhauser, L. Phillips, C. Reece, and H. Wang. Commissioning of the SRF Surface Impedance Characterization System at Jefferson Lab. In *Proceedings of the 23rd Particle Accelerator Conference*, pages 2144–2146, Vancouver,Canada, 2009. 18

[59] B.P. Xiao, X. Zhao, J. Spardlin, C.R. Reece, M.J. Kelley, T. Tan, and X.X. Xi. Surface Impedance Measurements of Single Crystal MgB_2 Films for Radiofrequency Superconductivity Applications. *Superconductor Science and Technology*, 25:095006, 2012. 18

[60] A. Gurevich. Enhancement of RF Breakdown Field of Superconductors by Multilayer Coating. *Applied Physics Letters*, 88(1):012511, 2006. 18, 19

[61] C.Z. Antoine, S. Berry, S. Bouat, J.-F. Jacquot, J.-C. Villegier, G. Lamura, and A Gurevich. Characterization of Superconducting Nanometric Multilayer Samples for Superconducting RF Applications: First Evidence of Magnetic Screening Effect. *Physical Review Special Topics - Accelerators and Beams*, 13(12), December 2010. 19

[62] A.-M. Valente-Feliciano, J.K. Spradlin, G. Eremeev, C. Reece, M.C. Burton, and R.A. Lukaszew. Growth and Characterization of Multilayer NbTiN Films. In *Proceedings of the 17th International Conference on RF Superconductivity*, Whistler, Canada, 2015. 19

[63] T. Tajima, G. Eremeev, G. Zou, V. Dolgashev, D. Martin, C. Nantista, S. Tantawi, C. Yoneda, B.H. Moeckly, and I. Campisi. RF Critical Field Measurement of MgB_2 Thin Films Coated on Nb. *Journal of Physics: Conference Series*, 234(1):012043, June 2010. 19

[64] A. Gurevich. Maximum Screening Fields and the Optimum Parameters of Superconducting Multilayers for Resonator Cavities. In *International Workshop on Thin Films and New Ideas for Pushing the Limits of RF Superconductivity*, Legnaro, Italy, October 2014. 19

[65] L.N. Hand. CVD SRF Cavities: Past, Present and Future. In *International Workshop on Thin Films and New Ideas for Pushing the Limits of RF Superconductivity*, Legnaro, Italy, 2006. 19

[66] P. Pizzol, A. Hannah, R. Valizadeh, O.B. Malyshev, S. Pattalwar, G.B.G. Stenning, T. Heil, and P.R. Chalker. Superconducting Coatings Synthetized by CVD/PECVD for SRF Cavities. In *Proceedings of the 17th International Conference on RF Superconductivity*, Whistler, Canada, 2015. 19

[67] F. Weiss, C. Jimenez, S. Pignard, M. Benz, E. Blanquet, R. Boichot, A. Mantoux, F. Mercier, and C. Antoine. Chemical Vapor Deposition Techniques for the Multilayer Coating of Superconducting RF Cavities. In *Proceedings of the 14th International Conference on RF Superconductivity*, pages 629–631, Paris, France, 2013. 19

[68] T. Proslier, J. Klug, N.C. Becker, J.W. Elam, and M. Pellin. Atomic Layer Deposition of Superconductors. *ECS Transactions*, 41(2):237–245, 2011. 19

[69] J.A. Thornton. Influence of Apparatus Geometry and Deposition Conditions on the Structure and Topography of Thick Sputtered Coatings. *Journal of Vacuum Science and Technology*, 11(4):666, July 1974. 20, 143

[70] E. Chiaveri. The CERN Nb/Cu Program for the LHC and Reduced Beta Superconducting Cavities. In *Proceedings of the 9th International Workshop on RF Superconductivity*, pages 352–356, Santa Fe, USA, 1999. wea003. 22, 89

[71] A. Grudiev, S. Atieh, R. Calaga, S. Calatroni, O. Capatina, F. Carra, G. Favre, L.M.A. Ferreira, J.-F. Poncet, T. Richard, A. Sublet, and C. Zanoni. Design of a Compact Superconducting Crab-Cavity for LHC Using Nb-on-Cu-Coating Technique. In *Proceedings of the 17th International Conference on RF Superconductivity*, Whistler, Canada, 2015. 22

[72] A. Anders. A Structure Zone Diagram Including Plasma-Based Deposition and Ion Etching. *Thin Solid Films*, 518(15):4087–4090, May 2010. 22

[73] A.-M. Valente-Feliciano. HiPIMS: a New Generation of Film Deposition Techniques for SRF Applications. In *Proceedings of the 16th International Conference on RF Superconductivity*, pages 748–754, Paris, France, 2013. 24, 109

[74] A. Anders. Discharge Physics of High Power Impulse Magnetron Sputtering. *Surface and Coatings Technology*, 205:S1–S9, July 2011. 24

[75] G. Rosaz, K. Ilyina, S. Calatroni, W. Vollenberg, A. Sublet, F. Leaux, and D. Richter. A15 Materials Thin Films and HiPIMS Progress at CERN for SRF Cavities. 3rd Annual Meeting of the EuCARD-2 WP12, April 2016. https://indico.cern.ch/event/494553/contributions/2005405/. 24, 89

[76] J. Spradlin, H.L. Phillips, C. Reece, A.-M. Valente-Feliciano, X. Zhao, D. Gu, and K. Seo. Structural Properties of Niobium Thin Films Deposited on Metallic Substrates by ECR Plasma Energetic Condensation. In *Proceedings of the 15th Conference on RF Superconductivity*, pages 877–882, Chicago, USA, 2011. 25

[77] A.-M. Valente-Feliciano. Nb Films: Substrates, Nucleation & Crystal Growth. In *Proceedings of the 15th International Conference on RF Superconductivity*, pages 332–342, Chicago, USA, 2011. 26

[78] M. Krishnan. Energetic Condensation Growth of Nb and Other Thin Films for SRF Accelerators. Conference Talk at the 16th International Conference on RF Superconductivity, September 2013. http://accelconf.web.cern.ch/AccelConf/SRF2013/talks/weioa02_talk.pdf. 26

[79] L. Ozyuzer, J.F. Zasadzinski, and K.E. Gray. Point Contact Tunnelling Apparatus with Temperature and Magnetic Field Control. *Cryogenics*, 38(9):911–915, September 1998. 26

[80] A.-M. Valente-Feliciano, G. Eremeev, H.L. Phillips, C. Reece, C. Cao, T. Proslier, J. Spradlin, and T. Tao. ECR Nb Films Grown on Amorphous and Crystalline Cu Substrates: Influence of Ion Energy. In *Proceedings of the 16th International Conference on RF Superconductivity*, pages 631–634, Paris, France, 2013. 26

[81] B.P. Xiao, C.E. Reece, H.L. Phillips, R.L. Geng, H. Wang, F. Marhauser, and M.J. Kelley. Note: Radio Frequency Surface Impedance Characterization System for Superconducting Samples at 7.5 GHz. *Review of Scientific Instruments*, 82(5):056104, 2011. 26, 49

[82] M. Krishnan, I. Irfan, T. Tajima, T. Proslier, R. Geng, P. Kneisel, C. Reece, and X. Zhao. Energetic Condensation Growth of Niobium Films. In *Proceedings of the 16th International Conference on RF Superconductivity*, pages 755–760, Paris, France, 2013. 26, 27

[83] S. Aull and K. Vales. Measurement Report of QPR F3.3. EDMS report 1554227, CERN, Geneva, Switzerland, October 2015. 27

[84] D. Douglass. Magnetic Field Dependence of the Superconducting Energy Gap. *Physical Review Letters*, 6(7):346–348, April 1961. 29

[85] D. Mattis and J. Bardeen. Theory of the Anomalous Skin Effect in Normal and Superconducting Metals. *Physical Review*, 111(2):412–417, July 1958. 30

[86] J.P. Turneaure, J. Halbritter, and H.A. Schwettman. The Surface Impedance of Superconductors and Normal Conductors: The Mattis-Bardeen Theory. *Journal of Superconductivity*, 4(5):341–355, July 1991. 30

[87] A.A. Abrikosov, L.P. Gor'kov, and I.M. Khalatnikov. Superconductor in a High Frequency Field. *Sov. Phys. JETP*, 8(1):182–189, 1959. 30

[88] A. Gurevich. Reduction of Dissipative Nonlinear Conductivity of Superconductors by Static and Microwave Magnetic Fields. *Physical Review Letters*, 113(8), August 2014. 30, 31

[89] T. L. Hylton, A. Kapitulnik, M. R. Beasley, John P. Carini, L. Drabeck, and George Grüner. Weakly Coupled Grain Model of High-Frequency Losses in High T_c Superconducting Thin Films. *Applied Physics Letters*, 53(14):1343, 1988. 31

[90] B Bonin and H Safa. Power Dissipation at High Fields in Granular RF Superconductivity. *Superconductor Science and Technology*, 4(6):257–261, June 1991. 31

[91] G. Ciovati, R.L. Geng, J. Mammosser, and J.W. Saunders. Residual Resistance Data From Cavity Production Projects at Jefferson Lab. *IEEE Transactions on Applied Superconductivity*, 21(3):1914–1917, June 2011. 31, 78

[92] T. Junginger. *Investigation of the Surface Resistance of Superconducting Materials*. PhD thesis, University of Heidelberg, Germany, July 2012. 31, 38, 53, 60, 69, 81, 115

[93] J. Halbritter. Transport in Superconducting Niobium Films for Radio Frequency Applications. *Journal of Applied Physics*, 97(8):083904, 2005. 31, 82, 83

[94] J. Halbritter. On Electric Surface Impedance. *Zeitschrift für Physik B Condensed Matter*, 31(1):19–37, 1978. 32, 56

[95] T. Junginger, W. Weingarten, and C.P. Welsch. Experimental Evidence for Electric Surface Resistance in Niobium. *arXiv preprint arXiv:1302.2802*, 2013. 32

[96] T. Junginger, R. Seviour, W. Weingarten, and C. Welsch. RF and Surface Properties of Bulk Niobium and Niobium Film Samples. In *Proceedings of the 3rd International Particle Accelerator Conference*, pages 2278–2280, New Orleans, USA, 2012. 32

[97] V. Palmieri and R. Vaglio. Thermal Contact Resistance at the Nb/Cu Interface as a Limiting Factor for Sputtered Thin Film RF Superconducting Cavities. *Superconductor Science and Technology*, 29(1):015004, January 2016. 32, 33, 87

[98] A.R. Strnad, C.F. Hempstead, and Y.B. Kim. Dissipative Mechanism in Type-II Superconductors. *Physical Review Letters*, 13(26):794–797, December 1964. 35

[99] J.I. Gittleman and B. Rosenblum. Radio-Frequency Resistance in the Mixed State for Subcritical Currents. *Physical Review Letters*, 16(17):734–736, April 1966. 35

[100] Y. Shapira and L.J. Neuringer. Magnetoacoustic Attenuation in High-Field Superconductors. *Physical Review*, 154(2):375–385, February 1967. 35

[101] J. I. Gittleman and B. Rosenblum. The Pinning Potential and High-Frequency Studies of Type-II Superconductors. *Journal of Applied Physics*, 39(6):2617, 1968. 35

[102] H. Suhl. Inertial Mass of a Moving Fluxoid. *Physical Review Letters*, 14(7):226–229, February 1965. 35

[103] A. Schmid and W. Hauger. On the Theory of Vortex Motion in an Inhomogeneous Superconducting Film. *Journal of Low Temperature Physics*, 11(5-6):667–685, June 1973. 35

[104] A.I. Larkin and Y.N. Ovchinnikov. Pinning in Type II Superconductors. *Journal of Low Temperature Physics*, 34(3-4):409–428, February 1979. 36

[105] C. Vallet, M. Boloré, and B. Bonin. Residual RF Surface Resistance Due to Trapped Magnetic Flux. Technical Report 93 15, DAPNIA/CE Saclay, September 1993. 37, 101, 104

[106] German Research Center for Geoscience. International Geomagnetic Reference Field Declination Calculator, 2018. `http://isdc.gfz-potsdam.de/igrf-declination-calculator/`. 37

[107] B. Bonin and R.W. Roeth. Q Degradation of Niobium Cavities Due to Hydrogen Contamination. In *Proceedings of the 5th International Workshop on RF Superconductivity*, pages 210–244, Hamburg, Germany, 1991. 38

[108] Y. Trenikhina, A. Romanenko, J. Kwon, J.-M. Zuo, and J.F. Zasadzinski. Nanostructural Features Degrading the Performance of Superconducting Radio Frequency Niobium Cavities Revealed by Transmission Electron Microscopy and Electron Energy Loss Spectroscopy. *Journal of Applied Physics*, 117(15):154507, April 2015. 38, 78

[109] M. Tinkham. *Introduction to Superconductivity*. Dover Publications, Mineola, N.Y., 2004. 38

[110] L. Cooper. Bound Electron Pairs in a Degenerate Fermi Gas. *Physical Review*, 104(4):1189–1190, November 1956. 39

[111] A.B. Pippard. An Experimental and Theoretical Study of the Relation between Magnetic Field and Current in a Superconductor. *Proceedings of the Royal Society A: Mathematical, Physical and Engineering Sciences*, 216(1127):547–568, February 1953. 40

[112] W. Weingarten. High-Frequency Cavities. In B. Seeber, editor, *Handbook of Applied Superconductivity*, volume 2, pages 1371–1406. Institute of Physics Pub., Bristol, 1998. 40

[113] C.P. Poole, H.A. Farach, R.J. Creswick, and R. Prozorov. *Superconductivity*. Academic : Elsevier, Road London, 2007. 41

[114] M. Hein. *High-Temperature-Superconductor Thin Films at Microwave Frequencies*, volume 155 of *Springer Tracts in Modern Physics*. Springer Berlin Heidelberg, Berlin, Heidelberg, 1999. 41

[115] A.A. Abrikosov. On the Magnetic Properties of Superconductors of the Second Group. *Soviet Physics JETP*, 5(6):1174–1182, 1957. 41

[116] C.-R. Hu. Numerical Constants for Isolated Vortices in Superconductors. *Physical Review B*, 6(5):1756–1760, September 1972. 41

[117] J.L. Harden and V. Arp. The Lower Critical Field in the Ginzburg-Landau Theory of Superconductivity. *Cryogenics*, 3(2):105–108, June 1963. 41, 42

[118] V.P. Galaiko. Stability Limits of the Superconducting State in a Magnetic Field for Superconductors of the Second Kind. *Soviet Physics JETP*, 23(3):475–478, March 1966. 42

[119] G. Catelani and J. Sethna. Temperature Dependence of the Superheating Field for Superconductors in the High-κ London Limit. *Physical Review B*, 78(22), December 2008. 42, 43

[120] J. Matricon and D. Saint-James. Superheating Fields in Superconductors. *Physics Letters A*, 24(5):241–242, February 1967. 42

[121] D. Brewer. Orsay Group on Superconductivity in Quantum Fluids, 1965. 42

[122] K. Saito. Theoretical Critical Field in RF Application. In *Proceedings of the 11th International Workshop on RF Superconductivity*, pages 1–16, Lübeck/Travemünde, Germany, 2003. 42, 44

[123] M.K. Transtrum, G. Catelani, and J.P. Sethna. Superheating Field of Superconductors Within Ginzburg-Landau Theory. *Physical Review B*, 83(9), March 2011. 43

[124] M.K. Transtrum. Author of Ref [123], Private Communication, 2015. 43

[125] T. Yogi, G.J. Dick, and J.E. Mercereau. Critical RF Magnetic Fields for Some Type-I and Type-II Superconductors. *Physical Review Letters*, 39(13):826, 1977. 43

[126] C.M. Lyneis. Electron Loading - Description and Cures. In *Proceedings of the 1st International Workshop on RF Superconductivity*, pages 119–144, Karlsruhe, Germany, July 1980. 45

[127] R.L. Geng. Multipacting Simulations for Superconducting Cavities and RF Coupler Waveguides. In *Proceedings of the 20th Particle Accelerator Conference*, pages 264–268, IEEE, 2003. 45

[128] P. Zhang and W. Venturini Delsolaro. The Multipacting Study of Niobium Sputtered High-Beta Quarter-Wave Resonators for HIE-ISOLDE. In *Proceedings of the 17th International Conference on RF Superconductivity*, Whistler, Canada, 2015. 45

[129] C. Schlemper, M. Vogel, and X. Jiang. Next Generation of SRF-Guns: Low Secondary Electron Yield Based on a Thin Film Apporach. In *Proceedings of the 17th International Conference on RF Superconductivity*, Whistler, Canada, September 2015. 45

[130] A. Shih, J. Yater, C. Hor, and R. Abrams. Secondary Electron Emission Studies. *Applied Surface Science*, 111:251–258, 1997. 46, 47

[131] V. Baglin, J. Bojko, C. Scheuerlein, O. Gröbner, M. Taborelli, B. Henrist, and N. Hilleret. The Secondary Electron Yield of Technical Materials and Its Variation with Surface Treatments. In *Proceedings of the 7th European Particle Accelerator Conference*, pages 217–221, Vienna, Austria, 2000. 46, 108

[132] B. Henrist, N. Hilleret, C. Scheuerlein, M. Taborelli, and G. Vorlaufer. The Variation of the Secondary Electron Yield and of the Desorption Yield of Copper Under Electron Bombardment: Origin and Impact on the Conditioning of the LHC. In *Proceedings of the 8th European Particle Accelerator Conference*, pages 2553–2555, Paris, France, 2002. 47

[133] N. Hilleret, C. Scheuerlein, and M. Taborelli. The Secondary-Electron Yield of Air-Exposed Metal Surfaces. *Applied Physics A: Materials Science & Processing*, 76(7):1085–1091, May 2003. 47, 108, 109

[134] H. Bruining. *Physics and Applications of Secondary Electron Emission*. Electronics and Waves. Pergamon Press LTD, London, UK, 1954. 47

[135] C. Yin Vallgren, G. Arduini, J. Bauche, S. Calatroni, P. Chiggiato, K. Cornelis, P.C. Pinto, B. Henrist, E. Métral, H. Neupert, G. Rumolo, E. Shaposhnikova, and M. Taborelli. Amorphous Carbon Coatings for the Mitigation of Electron Cloud in the CERN Super Proton Synchrotron. *Physical Review Special Topics - Accelerators and Beams*, 14(7), July 2011. 47

[136] M. Driss Mensi. Private Communication, 2013. 47

[137] S. Aull. Derivation of Material Parameters from Cavity Cold Tests. EDMS report 1554237, 2015. 49, 56

[138] M. Ribeaudeau, J.P. Charrier, S. Chel, M. Juillard, M. Fouaidy, and M. Caruette. RF Surface Resistance Measurement of Superconducting Samples with Vacuum Insulated Thermometers. In *Proceedings of the 6th European Particle Accelerator Conference*, pages 1873–1875, Stockholm, Sweden, 1998. 49

[139] M. Fouaidy, P. Bosland, S. Chel, M. Juillard, and M. Ribeaudeau. New Results on RF Properties of Superconducting Niobium Films Using a Thermometric System. In *Proceedings of the 8th European Particle Accelerator Conference*, pages 2229–2231, Paris, France, 2002. 49

[140] P. Welander, M. Franzi, and S. Tantawi. Cryogenic RF Characterization of Superconducting Materials at SLAC With Hemispherical Cavities. In *Proceedings of the 17th International Conference on RF Superconductivity*, pages 735–738, Whistler, Canada, 2015. JACOW, Geneva, Switzerland. 49

[141] L. Gurran, P. Goudket, S. Pattalwar, O.B. Malyshev, N. Pattalwar, T. Jones, E.S. Jordan, K. Dumbell, G. Burt, and R. Valizadeh. Superconducting Thin Film Test Cavity. In *Proceedings of the 17th International Conference on RF Superconductivity*, pages 731–734, Whistler, Canada, 2015. 49

[142] P. Goudket, S. Pattalwar, O.B. Malyshev, L. Gurran, G. Burt, E.S. Jordan, T.J. Jones, D.O. Malyshev, and R. Valizadeh. Test Cavity and Cryostat for SRF Thin Film Evaluation. In *Proceedings of the 6th International Particle Accelerator Conference*, pages 3232–3234, Richmond, USA, May 2015. JACoW. OCLC: 958149341. 49

[143] E. Mahner, S. Calatroni, E. Chiaveri, E. Haebel, and J. M. Tessier. A new instrument to measure the surface resistance of superconducting samples at 400 MHz. *Review of Scientific Instruments*, 74(7):3390, 2003. 49

[144] T. Junginger, W. Weingarten, and C.P. Welsch. Extension of the Measurement Capabilities of the Quadrupole Resonator. *Review of Scientific Instruments*, 83, 2012. 49, 50

[145] R. Kleindienst, A. Burrill, S. Keckert, J. Knobloch, and O. Kugeler. Commissioning Results of the HZB Quadrupole Resonator. In *Proceedings of the 17th International Conference on RF Superconductivity*, pages 930–936, Whistler, Canada, September 2015. 49

[146] Raphael Kleindienst. *Radio frequency characterization of superconductors for particle accelerators*. PhD thesis, Universität Siegen, 2017. 49

[147] J. Maniscalco, B. Clasby, T. Gruber, D. Hall, and M. Liepe. Recent Results from the Cornell Sample Host Cavity. In *Proceedings of the 17th International Conference on RF Superconductivity*, pages 626–628, Whistler, Canada, September 2015. JACOW, Geneva, Switzerland. 49

[148] P Goudket, T Junginger, and B P Xiao. Devices for srf material characterization. *Superconductor Science and Technology*, 30(1):013001, 2017. 49

[149] L.C. Maier and J.C. Slater. Field Strength Measurements in Resonant Cavities. *Journal of Applied Physics*, 23(1):68, 1952. 56

[150] Software COMSOL Multiphysics, 2015. 59

[151] Cryogenics Technologies Group. Material Properties: Stainless Steel 316. In *LNG Materials and Fluids*. National Institute of Standards and Technology, June 1979. 60

[152] Duthil, P. Material Properties at Low Temperatures. CERN Accelerator School, 2013. `http://indico.cern.ch/event/194284/contribution/7/material/4/0.pdf`. 60

[153] Bartington Instruments. Mag-01 & Mag-01h - Single Axis Fluxgate Magnetometers, 2014. Datasheet. 66

[154] SRF Institute JLab. Mechanical Polishing Recipe, January 2012. Internal Note. 69

[155] A.M. Valente-Feliciano, G. Eremeev, C. Reece, J. Spardlin, S. Aull, and T. Proslier. Material Quality & SRF Performance of Nb Films Grown on Cu via ECR Plasma Energetic Condensation. In *Proceedings of the 17th International Conference on RF Superconductivity*, Vancouver,Canada, 2015. 70

[156] A.T. Perez Fontenla. Surface SEM Observation on Niobium Coating on a Copper Substrate. Tech. Report EDMS 1462196, CERN, Geneva, Switzerland, January 2015. 71, 72

[157] A. Sublet. Niobium Coated HIE-ISOLDE QWR Superconducting Accelerating Cavities: coating process and film characterization. Talk at the International Workshop on Thin Films and New Ideas for Pushing the Limits of RF Superconductivity, June 2014. 73

[158] M. Bonura, J. Teyssier, and C. Senatore. Lower Critical Feld Measurements in Nb Film. Internal Measurement Report 011-01, Laboratoire de Technologie Avancée, Université de Genève, Geneva, Switzerland, September 2015. 74

[159] M. Bathe, F. Herrmann, and P. Schmuser. Magnetization and Susceptibility Measurements on Niobium Samples for Cavity Production. In *Proceedings of the 8th International Workshop on RF Superconductivity*, pages 881–889, Abano-Terme, Italy, 1997. 74

[160] A.-M. Valente-Feliciano. Towards High Performance Nb Thin Films via Energetic Condensation, June 2016. TTC Meeting at Saclay, France. 74

[161] F. Palmer. Influence of oxide layers on the microwave surface resistance of niobium. *IEEE Transactions on Magnetics*, 23(2):1617–1619, March 1987. 76

[162] B. Visentin, J. P. Charrier, B. Coadou, and D. Roudier. Cavity Baking: A Cure for the High accelerator Field Q_0 Drop. In *Proceedings of the 9th Workshop on RF Superconductivity*, pages 198–202, Santa Fe, USA, 1999. 76

[163] A. Dacca, G. Gemme, L. Mattera, and R. Parodi. XPS Analysis of the Surface Composition of Niobium for Superconducting RF Cavities. *Applied Surface Science*, 126(3-4), April 1998. 78

[164] K. Kowalski, A. Bernasik, W. Singer, X. Singer, and J. Camra. In situ XPS Investigation of the Baking Effect on the Surface Oxide Structure Formed on Niobium Sheets Used for Superconducting RF Cavity Production. In *Proc. of the 11th Workshop on RF Superconductivity, Travemünde, Germany*, 2003. 78

[165] A. Romanenko, A. Grassellino, F. Barkov, and J. Ozelis. Effect of mild baking on superconducting niobium cavities investigated by sequential nanoremoval. *Physical Review Special Topics - Accelerators and Beams*, 16(1), January 2013. 80

[166] B. Piosczyk, P. Kneisel, O. Stoltz, and J. Halbritter. Investigations of Additional Losses in Superconducting Niobium Cavities Due to Frozen-In Flux. *IEEE Transactions on Nuclear Science*, 20(3):108–112, 1973. 82

[167] L. Dufay, J.-M. Rieubland, and G. Vandoni. Summary of Thermal Impedance Measurementson Cu, Nb and Cu/Nb Samples in Superfluid Helium. CERN Cryo Note 10-00, August 2002. 84

[168] S. Bousson, M. Fouaidy, T. Junquea, N. Hammoudi, J. C. Le Scornet, and J. Lesrel. Kapitza Conductance and Thermal Conductivity of Materials Used for SRF Cavities Fabrication. In *Proc. of 9th Workshop on RF Superconductivity*, 1999. 84

[169] K. Mittag. Kapitza Conductance and Thermal conductivity of Copper, Niobium and Aluminium in the Range from 1.3 to 2.1 K. *Cryogenics*, 13(2):94–99, February 1973. 84

[170] C. Benvenuti, D. Bloess, E. Chiaveri, N. Hilleret, M. Minestrini, and W. Weingarten. Superconducting Cavities Produced by Magnetron Sputtering of Niobium on Copper. In *Proceedings of the 3rd International Workshop on RF Superconductivity*, pages 445–468, Argonne, USA, 1987. 85

[171] P. Bosland, A. Aspart, E. Jacques, and M. Ribeaudeau. Preparation and RF tests of L-band Superconducting Niobium-Coated Copper Cavities. *IEEE Transactions on Appiled Superconductivity*, 9(2):896–899, June 1999. 85

[172] C. Benvenuti, D. Boussard, S. Calatroni, E. Chiaveri, and J. Tueckmantel. Production and Test of 352 MHz Niobum-Sputtered Reduced-β Cavities. In *Proceedings of the 8th Workshop on RF Superconductivity*, pages 1038–1049, Abano-Terme, Ital, December 1997. 89

[173] P. Zhang. Private Communication, 2014. 89

[174] T. Junginger. Field Dependent Surface Resistance of Niobium on Copper Cavities. *Physical Review Special Topics - Accelerators and Beams*, 18(7), July 2015. 89, 98

[175] V. Cooley. Study of Thermocurrents in ILC cavities via measurements of the Seebeck Effect in niobium, titanium, and stainless steel thermocouples. Technical report, Fermi National Accelerator Laboratory, Batavia, USA, 2014. `http://lss.fnal.gov/archive/test-fn/0000/fermilab-fn-0980-td.pdf`. 91

[176] T. Kubo. Model of Flux Trapping in Cooling Down Process. In *Proceedings of the 17th International Conference on RF Superconductivity*, Whistler, Canada, 2015. 91

[177] S. Posen, A. Grassellino, A. Romanenko, O. Melnychuk, D.A. Sergatskov, M. Martinello, M. Checchin, and A.C. Crawford. Flux Expulsion Variation in SRF Cavities. In *Proceedings of the 17th International Conference on RF Superconductivity*, Whistler, Canada, 2015. 91, 98

[178] P. Zhang, G. Rosaz, A. Sublet, M. Therasse, and W. Venturini Delsolaro. The Influence of Cooldown Conditions at Transition Temperature on the Quality Factor of Niobium Sputtered Quarter-Wave Resonators for HIE-ISOLDE. In *Proceedings of the 17th International Conference on RF Superconductivity*, Whistler, Canada, 2015. 96, 98

[179] P. Zhang. The Influence of Cooldown Conditions at Transition Temperature on the Quality Factor of Niobium Sputtered Quarter-Wave Resonators. Talk at the International Workshop on Thin Films and New Ideas for Pushing the Limits of RF Superconductivity, August 2014. 98

[180] C. Benvenuti, P. Bernard, D. Bloess, G. Cavallari, E. Chiaveri, N. Circelli, W. Erdt, E. Haebel, J. Tuckmantel, W. Weingarten, H. Lengeler, P. Marchand, R. Stierlin, and H. Piel. RF Superconductivity at CERN. In *Proceedings of the 2nd International Workshop on RF Superconductivity*, pages 25–48, Geneva, Switzerland, 1984. 101, 104

[181] G. Arnolds-Mayer and E. Chiaveri. On a 500 MHz Single Cell Cavity with Nb_3Sn Surface. In *Proceedings of the 3rd International Workshop on RF Superconductivity*, pages 491–502, Argonne, USA, 1987. 101, 102

[182] G. Ciovati and A. Gurevich. Measurement of RF Losses due to Trapped Flux in Large-Grain Niobium Cavity. In *Proceedings of the 13th International Workshop on RF Superconductivity*, pages 132–136, Peking, China, 2007. 104

[183] D. Gonella and M. Liepe. Flux Trapping in Nitrogen-Doped and 120 °C Baked Cavities. In *Proceedings of the 5th International Particle Accelerator Conference*, page 3, Dresden, Germany, June 2014. 104

[184] P Garg, S Balachandran, I Adlakha, P J Lee, T R Bieler, and K N Solanki. Revealing the role of nitrogen on hydride nucleation and stability in pure niobium using first-principles calculations. *Superconductor Science and Technology*, 31(11):115007, oct 2018. 104

[185] C. Scheuerlein and N. Hilleret. *The Influence of an Air Exposure on the Secondary Electron Yield of Copper*. Diplomarbeit, TFH Berlin, Geneva, Switzerland, 1997. 107

[186] R. Warnecke. Emission Secondaire de Materiaux Purs. *Journal de Physique et le Radium*, 7(6):270–280, 1936. 107

[187] E.L. Garwin, E.W. Hoyt, R.E. Kirby, and T. Momose. Secondary Electron Yield and Auger Electron Spectroscopy Measurements on Oxides, Carbide, and Nitride of Niobium. *Journal of Applied Physics*, 59(9):3245, 1986. 107, 108

[188] R. Calder, G. Dominichini, and N. Hilleret. Influence of Various Vacuum Surface Treatments on the Secondary Electron Yield of Niobium. *Nuclear Instruments and Methods in Physics Research Section B: Beam Interactions with Materials and Atoms*, 13(1-3):631–636, March 1986. 108

[189] H Seiler. Secondary Electron Emission in the Scanning Electron Microscope. *Journal of Applied Physics*, 54(11):R1, 1983. 109

[190] V. Palmieri. New Materials for Superconducting Radiofrequency Cavities. In *Proceedings of the 10th International Workshop on RF Superconductivity*, pages 161–169, Tsukuba, Japan, 2001. 109

[191] P. Ylä-Oijala. Electron Multipacting in TESLA Cavities and Input Couplers. *Patricle Accelerators*, 63:105–137, 1999. 110

[192] L. Lilje, D. Reschke, P. Schmuser, D. Bloess, E. Haebel, E. Chiaveri, J.M. Tessier, H. Safa, and J.P. Charrier. Electropolishing and In-Situ Baking of 1.3 GHz Niobium Cavities. In *Proceedings of the 9th International Workshop on RF Superconductivity*, pages 74–76, Santa Fe, USA, 1999. 110

[193] Glenn F. Knoll. *Radiation Detection and Measurement*. Wiley, New York, 3rd ed edition, 2000. 113

[194] Sebastian Keckert. *Characterization of Nb_3Sn and multilayer thin films for SRF applications*. PhD thesis, Universität Siegen, 2019. 119

[195] M Arzeo, S Aull, E A Ilyina, S Fernandez, G J Rosaz, A. Myazaki, A-M Valente-Feliciano, M Bonura, C Senatore, and W Venturini Delsolaro. RF Performances of Superconducting Coatings on Copper for the FCC Study, June 2019. 5th International FCC Conference 2019. 119

List of Figures

List of Tables

Acronyms

ALD atomic layer deposition.

BCP buffered chemical polishing.

BCS Bardeen, Cooper, Schriefer.

CAD cathodic arc deposition.

CBP centrifugal barrel polishing.

CVD chemical vapour deposition.

cw continuous wave.

DC direct current.

DCMS direct current magnetron sputtering.

EBSD electron back scatter defraction.

EBW electron beam welding.

ECR electron cyclotron resonance.

EDS energy-dispersive X-ray spectroscopy.

EP electro-polishing.

fcc face centred cubic.

FG fluxgate.

FIB focussed ion beam.

HIPIMS high power impulse magnetron sputtering.

HPR high pressure rinsing.

HTS high critical temperature superconductor.

OFE oxygen-free electronic.

PID proportional–integral–derivative.

PLL phase-locked loop.

PTFE polytetrafluoroethylene.

PVD physical vapour deposition.

QPR Quadrupole Resonator.

RF radio-frequency.

SEM scanning electron microscopy.

SEY secondary electron yield.

SQUID Superconducting quantum interference device.

SRF superconducting radio-frequency.

UHV ultra-high vacuum.

VSM vibrating sample magnetometer.

Laboratories, Companies and Accelerators

ALPI Acceleratore Lineare Per Ioni at INFN Legnaro, Italy.

ASTeC Accelerator Science and Technology Centre, United Kingdom.

Bmax Supplier of magnetic pulse systems, Toulouse, France.

CERN European Organization for Nuclear Research, originally: *Conseil Européen pour la Recherche Nucléaire*, Geneva, Switzerland.

FCC Future Circular Collider; Study.

HIE-Isolde High Intensity and Energy Upgrade of the ISOLDE Facility at CERN, Geneva, Switzerland.

HZB Helmholtz-Zentrum Berlin, Germany.

JLab Thomas Jefferson National Laboratory, Newport News, Virgina, USA.

LBNL Lawrence Berkeley National Laboratory, Berkeley, California, USA.

LEP Large Electron-Positron Collider at CERN, Geneva, Switzerland.

LHC Large Hadron Collider at CERN, Geneva, Switzerland.

Symbols

Φ_0 Magnetic flux quantum.

$\varepsilon_{\mathrm{pin}}$ Depinning efficiency ranging from 0 % for complete pinning and 100 % for complete depinning.

$\lambda(0, \ell)$ Effective penetration depth at 0 K and finite mean free path ℓ.

ρ electrical resistivity.

ℓ Electron mean free path.

Δ_0 Superconducting gap at 0 K.

μ_0 Vacuum permeability, $\mu_0 = 4\pi 10^{-7}$ H/m.

λ_L London penetration depth, literature value.

ε_{TF} Flux trapping efficiency.

λ_{eff} Effective penetration depth for a finite temperature and mean free path.

ξ_{eff} Coherence lenght, characteristic length scale for the interaction distance of a Cooper pair and radius of normal conducting area of a vortex.

ρ_n Electrical resistivity in the normal conducting state.

A_{BCS} BCS factor, depends on material properties and frequency.

B_{TF} Trapped magnetic field.

B_{ext} Externally appield or ambient magnetic field.

B_{RF} RF magnetic field.

G Geometry factor, $G = \frac{\omega_0 \mu_0 \int |\bar{H}|^2 dV}{\int |\bar{H}|^2 dS}$.

P_{diss} Dissipated power.

Q Quality factor, ratio of stored energy over power loss, $Q = \frac{\omega_0 U}{P_{\mathrm{diss}}}$.

R_{K} Kapitza resistance.

R_{TF} Surface resistance due to trapped magnetic flux. Contributes to the residual surface resistance R_{res}.

R_B Thermal boundary resistance.

R_{BCS} BCS surface resistance.

$R_{Nb/Cu}$ Thermal contact resistance of the Nb-Cu interface.

R_S Total surface resistance.

R_{res} Residual surface resistance.

$S_{\mathbf{TF}}$ Trapped flux sensitivity.

T Temperature.

T_0 Helium bath temperature.

Z_S Surface impedance.

c speed of light.

$f_{\mathbf{0}}$ Resonance/operating frequency.

$f_{\mathbf{p}}$ Depinning frequency.

f_{0K} Resonance frequency at 0 K.

g Gibbs free energy density.

j_T transport current.

p Relative pinning center size.

RRR Residual resistance ratio, $RRR = \frac{\rho(300\,\mathrm{K})}{\rho(10\,\mathrm{K})}$.

SUBU Mixture of sulfamic acid, hydrogen peroxide, n-butanol and ammonium citrate.

Xs Surface reactance.